Impact of the mechanical perturbations on the performance of the LHC superconducting dipole magnets

Calvi, Marco

How to cite

CALVI, Marco. Impact of the mechanical perturbations on the performance of the LHC superconducting dipole magnets. Doctoral Thesis, 2005. doi: 10.13097/archive-ouverte/unige:37852

This publication URL: https://archive-ouverte.unige.ch/unige:37852
Publication DOI: 10.13097/archive-ouverte/unige:37852

UNIVERSITÉ DE GENÈVE
Groupe de Physique Appliquée

FACULTÉ DES SCIENCES
Professeur R. Flükiger

Impact of the Mechanical Perturbations on the Performance of the LHC Superconducting Dipole Magnets

THÈSE

présentée à la Faculté des sciences de l'Université de Genève pour
obtenir le grade de Docteur ès sciences, mention physique

par

Marco CALVI

d'Italie

Thèse No 3627

GENÈVE

2004

FACULTÉ DES SCIENCES

UNIVERSITÉ DE GENÈVE

Doctorat ès sciences
mention physique

Thèse de *Monsieur Marco CALVI*

intitulée :

" Impact of the Mechanical Perturbations on the Performance of the LHC Superconducting Dipole Magnets "

La Faculté des sciences, sur le préavis de Messieurs R. FLUKIGER, professeur ordinaire et directeur de thèse (Département de physique de la matière condensée), M. DROZ, professeur titulaire (Département de physique théorique), L. ROSSI, professeur (CERN – Accelerator Technology Division – Magnet and Superconductor Group – Geneva, Switzerland), A. SIEMKO, docteur (CERN – Magnet and Measurements – Geneva, Switzerland), et P. TIXADOR, professeur (CNRS/CRTBT-LEG – Grenoble, France), autorise l'impression de la présente thèse, sans exprimer d'opinion sur les propositions qui y sont énoncées.

Genève, le 3 janvier 2005

Thèse - 3627 -

Le Doyen, Pierre SPIERER

P. Spierer

N.B.- La thèse doit porter la déclaration précédente et remplir les conditions énumérées dans les "Informations relatives aux thèses de doctorat à l'Université de Genève".

Nombre d'exemplaires à livrer par colis séparé à la Faculté : - 7 -

« Impact des perturbations mécaniques sur la performance des dipôles supraconducteurs du *Large Hadron Collider* »

Résumé de thèse en langue française

Le travail qui est exposé ici s'inscrit dans le Projet du *Large Hadron Collider* (LHC ou Grand collisionneur de hadrons) sous-tendant la construction du futur accélérateur circulaire de l'Organisation européenne pour la recherche nucléaire (CERN). Le LHC doit être le plus grand accélérateur de particules jamais construit et devra produire des collisions frontales entre deux faisceaux de protons accélérés à une énergie de 7 TeV. Il sera installé dans le tunnel de près de 27 km de circonférence de son prédécesseur, le *Large Electron Positron* (LEP) et fonctionnera grâce à un champ magnétique de 8.33 Tesla nécessaire au confinement des particules pour un tel niveau énergétique. Cette performance technique est rendue possible grâce au principe de la supraconductivité du NbTi refroidi par de l'hélium superfluide à une température de 1.9 K.

La présente recherche est consacrée à l'étude de la performance du *quench* des aimants supraconducteurs des dipôles du LHC et en particulier au *quench training* que l'on observe dans ce type de dispositifs. Ce phénomène correspond à l'amélioration progressive de la performance du *quench* d'aimants supraconducteurs à la suite d'énergisations et de transitions successives entre un état supraconducteur et un état normal de conduction. Des *training quenches* prématurés sont généralement causés par des énergies transitoires qui sont libérées dans le bobinage magnétique alors qu'il est traversé par un courant, ces perturbations provenant en général des mouvements du conducteur sous l'action de la force de Lorentz. L'ensemble de ces évènements mécaniques produit des rapides variations de tension (de l'ordre de quelques millisecondes), appelées des *spikes*, et mesurées dans différentes parties du bobinage de l'aimant.

A ce jour, il n'existe pas de modèle solide permettant la prédiction de l'impact de l'activité mécanique sur le comportement du *quench* ; cette absence a donc impulsé cette étude. La prédiction de la performance du *quench* des aimants supraconducteurs et la compréhension du comportement de *training* sont les principales questions auxquelles ce projet tente de répondre. Le point de départ a été la mise en évidence des signaux précurseurs du *quench* se manifestant avant que l'aimant n'atteigne sa conductivité normale et l'étude de la tension résistive qui en résulte. La manifestation d'un grand nombre de ces signaux précurseurs lors de l'alimentation des aimants, a suggéré d'aborder le problème sous un angle statistique et d'en examiner les propriétés quant à leur distribution. Dans cette optique, nous avons élaboré une nouvelle sonde afin de localiser avec précision l'origine de la transition résistive dans le bobinage et nous avons installé un système d'acquisition adéquat. De plus, différents modèles théoriques ont été introduits en vue d'interpréter les données et les résultats expérimentaux obtenus.

Dans le Chapitre n°1, nous présentons un aperçu général du Projet du LHC (données générales, design) tout en faisant référence à différents grands collisionneurs circulaires existants dans le monde et en faisant une courte introduction à la physique des accélérateurs circulaires et à ses paramètres généraux. Les besoins spécifiques du LHC justifient l'utilisation d'aimants supraconducteurs de grande échelle constitués d'un alliage de NbTi et fonctionnant avec la technologique du refroidissement par de l'hélium superfluide, nous en exposons donc les principales caractéristiques.

Le Chapitre n°2 introduit le concept de la supraconductivité en se focalisant sur les supraconducteurs à basse température utilisés dans la physique à haute énergie. On présentera également les propriétés et utilisations de l'alliage NbTi (de type II) pour la fabrication des câbles employés dans les bobinages des aimants supraconducteurs du LHC. La conception des aimants supraconducteurs des dipôles du LHC est ensuite discutée selon les buts de ce travail ce qui permet d'aborder le problème de la stabilité du conducteur au sujet des transitions résistives irréversibles et de mettre l'accent sur les sources de perturbations potentielles et les mesures expérimentales.

Le Chapitre n°3 est consacré à l'étape finale du processus de contrôle qualité du principal système magnétique du LHC qui consiste en 1232 dipôles et environ 500 quadrupôles supraconducteurs. L'ensemble de ces aimants est préalablement testé dans des conditions cryogéniques à 1.9 K, et ce, avant leur installation dans le tunnel de l'accélérateur. Ces tests se déroulent au CERN dans le *Superconducting Magnet Test Plant* (SMTP), laboratoire développé à cet effet, et les principales phases de leur déroulement sont résumées dans ce chapitre y compris dans leurs modes opératoires. Le système cryogénique utilisé lors du déroulement de ces tests mobilise 12 *Cryogenic Feed Boxes* (CFB) et sera ensuite détaillé conjointement aux procédures utilisées pour refroidir les aimants à 1.9K, aux principales caractéristiques du système d'alimentation, à la topologie des circuits électriques ainsi qu'à l'équipement du test principal (utilisé pour les tests de puissance). Un accent particulier est mis sur les anti-cryostats utilisés pour garder l'ouverture des aimants à température ambiante et qui, de ce fait, rendent cet équipement accessible à des mesures à chaud. Les antennes standards utilisées pour la localisation du *quench* et la détection des *spikes* sont décrites en détail ainsi que les techniques mobilisées pour la compensation des signaux issus des bobinages de détection. En dernier lieu, nous expliciterons les systèmes d'acquisition utilisés dans le cadre de l'enregistrement des signaux de tension provenant des capteurs de l'aimant et des antennes de *quench*.

La première partie du Chapitre n°4 est consacrée au *quench* puisqu'une bonne compréhension des processus électriques et thermiques endurés durant une transition de phase résistive dans le câble supraconducteur d'un bobinage est fondamentale pour une interprétation correcte de la tension cumulée associée au processus et pour l'analyse des signaux acquis dans les antennes du *quench*. Les résultats des analyses de ce type de signaux sous l'angle des problèmes de stabilité du câble et de la protection des aimants fournissent un feedback important durant les phases de conception et de prototypage des dispositifs ; ces résultats fournissent également un puissant moyen de contrôle de la qualité durant les phases de production et de test. L'interprétation de ces résultats expérimentaux a fait appel à des outils mathématiques standards en la matière, à savoir : de l'équation générale tridimensionnelle de l'équilibre de chaleur dans un corps solide en allant vers l'estimation du *quench-load* (cette dernière étant utilisé actuellement dans le cadre des premières estimations de l'évolution du *hot spot* de température). Dans la seconde partie de ce chapitre, nous abordons le rôle des câbles Rutherford du LHC et nous présentons les simulations par ordinateur des modèles à deux fils que nous avons pu obtenir grâce à l'élaboration du code *Simulation Program for Quench Research* (SPQR) développé spécialement à cette occasion. A noter que le modèle implanté est particulièrement adapté pour la recherche et l'étude de la redistribution de courant induite par une transition résistive. Ensuite, nous discutons de la conception d'un câble mixte qui permettrait une augmentation de la vitesse de propagation du *quench* tout en simplifiant le système de protection des aimants. A la fin de ce chapitre, on proposera un modèle de câbles multi-fils dans des conditions adiabatiques ainsi que son référencement.

Le Chapitre n°5 relate l'élaboration d'une nouvelle antenne à *quench* à haute résolution (LQA ou *Local Quench Antenna*) permettant la localisation du *quench* lors de la productiona en série des aimants des dipôles du LHC. Le système a été conçu afin d'identifier avec une grande précision (de l'ordre du centimètre) la zone où le *quench* nait et doit ainsi permettre une meilleure compréhension de son origine. Les mesures effectuées ont également montré que la vitesse de propagation du *quench* pouvait être estimée avec une bonne précision. Nous exposons en détails la conception de l'antenne et la configuration d'exploitation standard sans oublier de mentionner la procédure utilisée pour l'analyse des données issues des différentes mesures que nous avons réalisées.

Le Chapitre n°6 est dévolu à la présentation du critère de distinction entre le bruit et le signal précurseur de *quench* associé aux mouvements du câble ainsi qu'à l'utilisation conjointe des compensations longitudinales et transversales. Nous discutons également du traitement statistique des paramètres des *spikes* et des expériences spécialement réalisées pour la compréhension de l'origine microscopique du comportement de *training* et dans le cadre de l'exploration de la mémoire du système.

Dans le Chapitre n°7, nous proposons une interprétation phénoménologique des perturbations mécaniques mesurées au moyen des *pick-up coils* et, après un résumé succinct des principales données expérimentales, nous introduisons un modèle à *spring block* simple en présence de frictions solides. Cette approche vise à analyser l'origine des dynamiques de « collé-glissé » (*stick-slip)* et de l'hystérèse mécanique et nous permet par la suite de définir un système à modèle couplé de *spring block* que l'on peut mettre en parallèle avec les « modèles-jouets » (*toy-models*) similaires utilisés dans la physique théorique des tremblements de terre. Dans les dernières lignes de ce travail, nous analysons la sensibilité d'un tel système à la lumière des conditions initiales et nous éclaircissons le rôle joué par la friction solide. Enfin, nous parlons des dynamiques et des propriétés statistiques de ce type de système qui ont été calculées à l'aide d'une équivalence à automate cellulaire, et ce, dans une et deux dimensions ; l'agrément qualitatif avec la phénoménologie_sont finalement mis en exergue.

Abstract

The present research is dedicated to the quench performance of the LHC superconducting dipole magnets. The remarkable phenomenon observed in these devices is the so called quench training. This term is commonly used to describe the progressive improvement of the quench performance of superconducting magnets after repeated energization and transitions from superconducting to normal state. Premature training quenches are usually caused by transient energy released within the magnet coil as it is energized. This disturbances usually originate from conductor motions under the action of the Lorentz forces. All these mechanical events produce in general rapid variations of voltages, called spikes, measured across different parts of the magnet coil. The absence of any solid theory to predict the impact of the mechanical activity on quench behavior has triggered this work. Predicting the quench performance of the superconducting magnets and understanding the training behavior are the main answers this project is trying to provide. The starting point has been to evidence the quench precursor signals occurring before the magnet gets normal conducting and a resistive voltage is developed across it. The precursor signals are not scarce in typical magnet powering history. This suggested to approach the problem from a statistical point of view and to study the precursor properties in terms of their distributions. A new probe has been designed and constructed to precisely locate the origin of the resistive transition within the magnet coil and a more powerful acquisition system has been installed. Several theoretical models have been introduced to interpret the acquired data and the experimental results obtained.

Contents

Introduction

This work has been carried out in the context of the Large Hadron Collider Project (LHC), which is at present the next circular accelerator being constructed at CERN. The LHC will accelerate two proton beams at the energy of 7 TeV and collide them head-to-head. To confine particles at that energy in the existing tunnel of 27 km circumference a magnetic field of 8.33 Tesla is required. This technical requirement has been achieved with the technology of superconducting NbTi, cooled with pressurized superfluid helium at the temperature of 1.9 K.

The present research is dedicated to the quench performance of the LHC superconducting dipole magnets. The remarkable phenomenon observed in these devices is the so called quench training. This term is commonly used to describe the progressive improvement of the quench performance of superconducting magnets after repeated energization and transitions from superconducting to normal state. Premature training quenches are usually caused by transient energy released within the magnet coil as it is energized. This disturbances usually originate from conductor motions under the action of the Lorentz forces. All these mechanical events produce in general rapid variations of voltages, called spikes, measured across different parts of the magnet coil. The absence of any solid theory to predict the impact of the mechanical activity on quench behavior has triggered this work. Predicting the quench performance of the superconducting magnets and understanding the training behavior are the main answers this project is trying to provide. The starting point has been to evidence the quench precursor signals occurring before the magnet gets normal conducting and a resistive voltage is developed across it. The precursor signals are not scarce in typical magnet powering history. This suggested to approach the problem from a statistical point of view and to study the precursor properties in terms of their distributions. A new probe has been designed and constructed to precisely locate the origin of the resistive transition within the magnet coil and a more powerful acquisition system has been installed.

In Chapter 1 a general overview of the LHC Project is given with reference to several existing large circular accelerators. The use of large scale superconducting magnets made of NbTi alloy and the technology of cooling with superfluid helium is justified with regards to the specific requirements of the LHC machine. A short introduction to the physics of a circular accelerator and of its main parameters is given while the layout of LHC is summarized.

In Chapter 2 the phenomenon of superconductivity is introduced with particular emphasis on the so called *low temperature superconductors* which are used in the high energy physics applications. The applications of NbTi alloy (type II) in cables used in coil windings of the LHC superconducting magnets is presented. The design of LHC superconducting dipole magnets is discussed in terms of the aims of this work. The problem of the conductor stability with respect to irreversible resistive transitions is introduced and possible sources of disturbances are pointed out and experimental measurements are discussed.

In Chapter 3 the final step of the LHC quality assurance is described in case of the main magnetic system of the LHC, consisting of 1232 twin aperture, high-field superconducting dipoles and about 500 twin-aperture, high-gradient superconducting quadrupoles. All these magnets, prior to their installation in the accelerator tunnel, are tested in 1.9 K cryogenic conditions. The tests are carried out at CERN in a purpose built Superconducting Magnet Test Plant (SMTP). The main features of this test facility are summarized including its operation modes. The cryogenic system of the test facility, requiring 12 so-called Cryogenic Feed Boxes (CFB), is introduced and the procedures used to cool down magnets to 1.9 K are described. The main characteristics of the powering system and the topology of the electrical circuits are presented. The main test equipment used to performed the power tests is outlined. In particular the anti-cryostats used for keeping the magnet apertures at room temperature, making them accessible for warm measuring equipment are presented. The standard antennas used for quench localization and spike detection are described in details and the techniques used for compensating the signals from the pick-up coils are explained. The acquisition systems used for recording the voltage signals coming out from the magnet sensors and from the quench antennas is presented.

In Chapter 4 the quench process is introduced. A fair understanding of the electrical and thermal processes undergoing a restive phase transition in a superconducting cable of a magnet coil is essential to interpret correctly the associated voltage build-up and to analyze the read out signals of the quench antenna. Results of the analysis of such signals with respect to cable stability and magnet protection issues, give an important feedback during the design and prototyping phase of the devices, and serve as a powerful quality control mean, during the production and testing. The standard mathematical tools for the interpretations of the experimental results are summarized starting from the general three dimensional heat balance equation in a solid body down to the estimation of the so called *quench-load*, which is currently used for a first estimation of the hot spot temperature evolution. In the second part of the chapter computer simulations of the two wire networks, obtained by means of a purpose developed code, SPQR (Simulation Program for Quench Research) are presented for the LHC Rutherford cables. The implemented model is suitable for the investigation of the current redistribution induced by a resistive transition. The design of a mixed wire cable is discussed in terms of the possible increase of the quench propagation velocity and simplification of magnet protection system. At the end of the chapter a proposed formalism for multi-wire cables in adiabatic conditions is presented and references in the subject are provided.

In Chapter 5 a new high resolution local quench antenna (LQA) for dedicated quench research on the series production of the LHC dipole magnet is presented. The system has been designed to localize with centimeter precision the starting region of a quench for a better understanding of its origin. The performed measurements demonstrated also that the quench propagation velocity can be estimated with good precision. The design of the antenna and the standard operating configuration are illustrated in detail and the procedure used for the analysis of several measurement data is discussed.

In Chapter 6 the criteria to distinguish between noise and the quench precursor signal associated to cable motions are presented. The combined use of transversal and longitudinal compensations is explained. The statistical treatment of spike parameters is discussed. Special experiments have been performed to understand the microscopic origin of the training behavior and to investigate the system memory.

In Chapter 7 a possible interpretation of the phenomenology of the mechanical disturbances measured by means of pick-up coils are discussed. Starting with a short resume of main experimental evidences a simple spring block model in presence of solid friction is introduced. This approach aims to analyzes the origin of the stick-slip dynamics and the mechanical hysteresis. Afterwards a system of coupled spring block model is defined and the parallel with similar toy-models used in theoretical earthquake physics is discussed. The sensitivity of such system with respect to the starting conditions is analyzed and the role played by solid friction model is clarified. The dynamics and the statistical properties of such system are computed using a cellular automaton equivalence both in one and in two dimension and the qualitative agrement with the phenomenology is evidenced.

Chapter 1

The Large Hadron Collider

A general overview of the LHC Project is given with reference to existing large circular accelerators. The use of large scale superconducting magnets made of NbTi alloy and the technology of cooling with superfluid helium is justify with regards to the specific requirements of the LHC machine. A short introduction to the physic of a circular accelerator and of its main parameters is given while the layout of LHC is summarized.

1.1 LHC project

The LHC [1, 2] is the circular accelerator that will substitute its predecessor, already decommissioned Large Electron Positron collider (LEP). The main scientific goal of the LHC is to provide experimental evidences for the *Higgs boson* and to investigate the first 1 TeV range of energy in which existing theories strongly indicate that new particles will begin to emerge. The LHC will reach this range of energy accelerating proton beams. A proton is a complex particle containing quarks and gluons amongst which the energy is shared, so to reach the 1 TeV range of energy per quark protons have to be accelerated to 7 TeV.

The existing 27 km LEP tunnel will be used to install the LHC components. In order to keep the proton beams on a stable orbit at that energy a dipole magnetic field of 8.33 T is required. A high current density is needed to generate such a field and for this reason a superconducting magnet system has been designed. The use of superconducting wires is in practice the only solution to achieve the required field strength and keeping the total cost reasonably low.

There are three large operating accelerators built with superconducting magnets: the Tevatron (Fermilab in Chicago, USA), HERA (Desy in Hamburg, Germany) and RHIC (BNL in New York, USA). All make use of classical NbTi superconductors cooled with normal liquid helium at a temperature slightly above 4.2 K, and their operational fields are relatively low (4 T for the Tevatron and 4.7 T for HERA, 3.45 T RHIC). The only way for obtaining fields of and above 8 T in accelerator magnets using NbTi with sufficient margin is to cool the superconductors to temperature below 2 K. This technique has been applied successfully at the French Tokamak TORESUPRA magnet, in operation at Cadarache. Below 2.17 K, helium is in the so-called superfluid state, with much lower viscosity and much higher heat transfer capacity than that of liquid helium above 2.17 K. These properties determine the

Parameter	unit	value
Injection energy	GeV	450
Energy	TeV	7
Dipole field	T	8.34
Number of dipoles magnets		1232
Luminosity	cm	10^{34}
Particles per bunch		10^{11}
r.m.s bunch length	cm	7.5
Bunch spacing	ns	25
Circulating current per beam	A	0.54
Energy loss per turn	keV	6.7

Table 1.1: The LHC main parameters

design of the cooling system, and in particular permit a drastic reduction of the helium flow through the magnets. On the other hand, between 4.2 K and 1.9 K, the enthalpy of metals and in particular of the superconducting cables is reduced by almost an order of magnitude. As a consequence higher temperature appear for a given deposit of energy. This feature calls for particular care in limiting the transient heat loads like for instance those originating in conductor motions, which have their origin in the large electromagnetic forces exerted on the coil windings by the magnetic field. It should be noted that the electromagnetic forces acting on the conductor increase with B and so does the stored electromagnetic energy, calling for stronger force-retaining structures and more elaborate quench protection systems than in previous projects.

The conceptual design of the LHC has been published in the LHC design report [2]. The overall eight fold symmetry is due to the existing LEP tunnel architecture. The LHC will be subdivided into octants and will host four large scale experiments: ALTAS, CMS, LHC-b and Alice. The LHC can also accelerate the lead ions up to 5.5 TeV/nucleon and therefore will allow the heavy-ion experiment with unprecedented energy densities. In the case of two counter-rotating beams the machine is designed to achieve a luminosity exceeding 10^{34} $cm^{-2}s^{-1}$. The luminosity L is defined as

$$L = N_1 \cdot N_2/(4\pi \cdot \sigma_x\sigma_y) \cdot n_b \cdot f_{rev} \tag{1.1}$$

where N_1 are N_2 are the number of particles per bunch for each beam, σ_x and σ_y are the beam sizes in the transverse directions cross-section, n_b the number of bunches in each beam, f_{rev} the revolution frequency (ca. 11 kHz). The high luminosity will be achieved by filling the LHC with 2808 bunches of 10^{11} particles per bunch which give a time averaged beam current of 0.56 A (see Table 1.1). In order to keep the particle trajectories stable, the field quality of the main magnets must be very high and in addition a large number of correction magnets must be implemented. As the proton bunches collide every 25 ns in the detectors, their electronics must provide a fast response and readout to avoid integrating over many bunch crossings. Both beams will be collided at collision energy for about 10 hours. During this period the amplitude of the particle oscillations around the central orbit should not increase significantly, because this would dilute the beams and degrade luminosity.

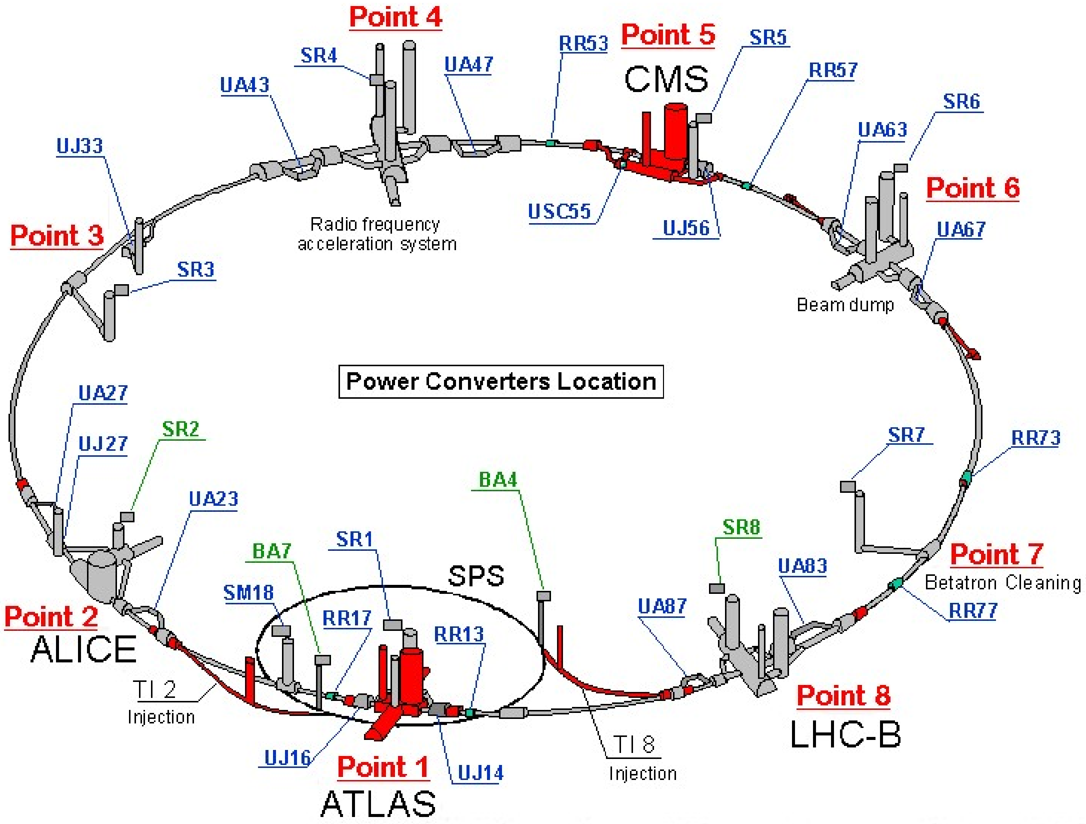

Figure 1.1: Schematic layout of the LHC. Beam 1 circulates clockwise and Beam 2 counter-clockwise.

A tiny fraction of the beam that diffuses towards the beam pipe wall and is consequently lost (this phenomenon is usually referred to as beam loss) may be sufficient to cause a resistive transition in the superconducting magnets (quench), which will interrupt the machine operation for several hours.

The feasibility of the LHC has been studied since 1984 within an R&D program for superconducting magnets and the design of the machine lattice. The CERN Council approved in 1996 the LHC project as to be built in one stage with 7 TeV nominal design beam energy.

1.2 LHC Layout

The basic layout of the LHC follows the LEP tunnel geometry and is depicted in Fig. 1.1. The LHC has eight arcs and eight straight sections [2]. Each straight section is approximately 528 m long and can serve as an experimental or utility insertion. The two high luminosity experimental insertions are located at diametrically opposite straight sections: the ATLAS experiment is located at point 1 and the CMS experiment at point 5. Two more experimental insertions are located at point 2 and point 8 which also contain the injection systems for Beam 1 and Beam 2, respectively. The injection kick occurs in the vertical plane with the two beams arriving at the LHC from below the LHC reference plane. The beams only

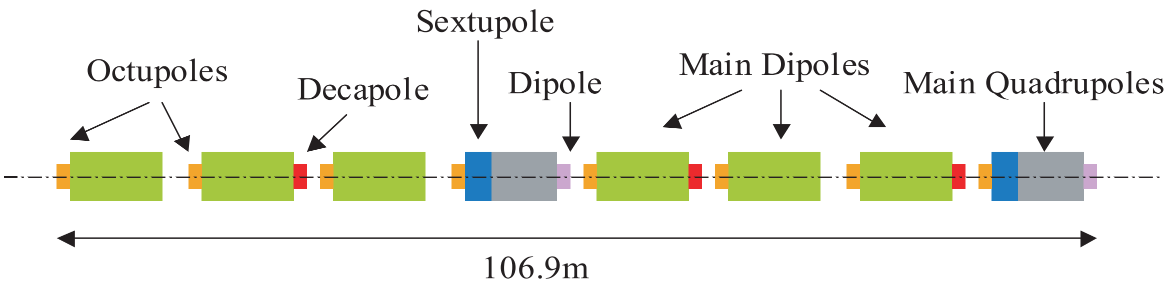

Figure 1.2: Schematic layout of the LHC arc cell. The main structure consist of main dipole and quadrupole magnets. The corrector scheme is composed of trim quadrupole (MQT), skew trim quadrupole (MQS), lattice octupole (MO), sextupole (skew sextupole) + orbit corrector (MSCB), spool piece sextupole (MCS), spool piece octupole + decapole (MCDO)

Parameter	unit	value
Magnetic length	m	14.3
Operating temperature	K	1.9
Current at injection (0.45 TeV)	A	739
Bending radius	m	2803.928
Number of beams per magnet		2
Nominal current	A	11850
Bending angle per magnet	mrad	5.1000
Peak field in coil	T	8.76
Field at injection	T	0.535
Field @7 TeV	T	8.33
Inductance per magnet	H	0.108
Mass of cold mass	t	23.8

Table 1.2: The LHC superconducting dipole main parameters

cross from one magnet bore to the other at these four locations. The remaining four straight sections do not have beam crossings. Insertion 3 and 7 each contain two collimation systems. Insertion 4 contains two RF systems: one independent system for each LHC beam. The straight section at point 6 contains the beam dump insertion where the two beams are vertically extracted from the machine using a combination of horizontally deflecting fast-pulsed ("kicker") magnets and vertically-deflecting double steel septum magnets. Each beam features an independent abort system.

1.2.1 Arc Region

As for all circular accelerators, the LHC arcs consist of a regular cell structure (Fig. 1.2) that is repeated many times around the ring. Dipole magnets are used to deflect the beam whereas quadrupole magnets act as lenses to focus the beam. Different from an optical lens, a magnetic lens focuses in one transverse direction and defocuses in the other transverse direction. In order to obtain a net focusing effect, two quadrupole magnets are needed. These

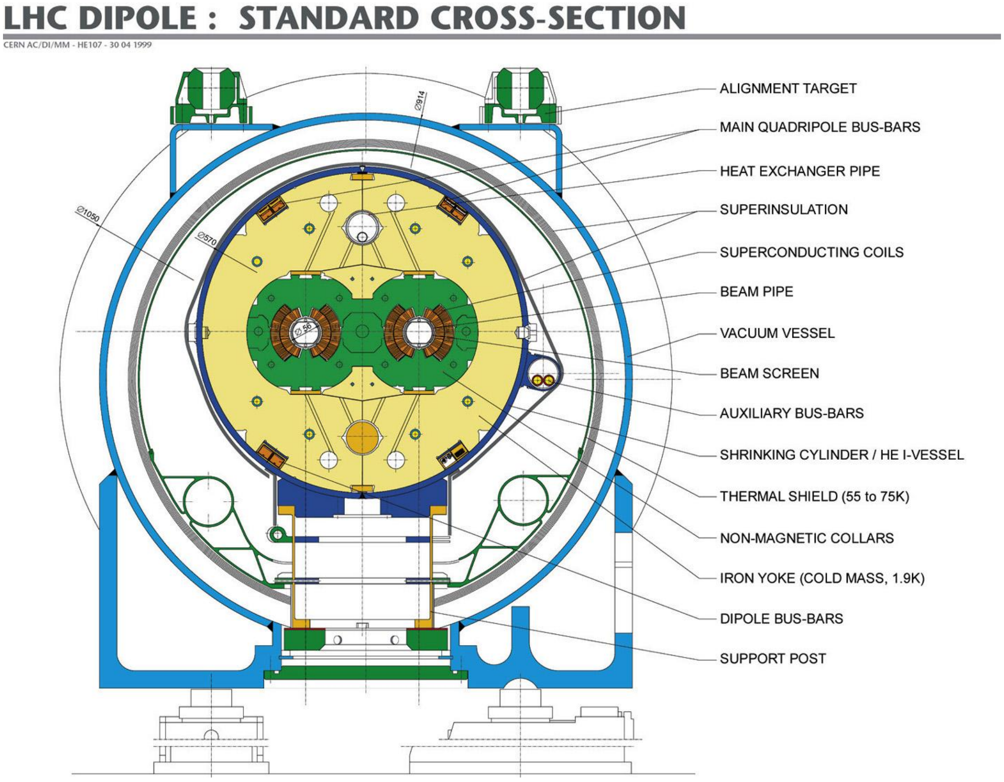

Figure 1.3: The standard LHC arc dipole cross section

form the so called *FODO lattice*, in which F and D stand for the focusing and defocusing quadrupole and in a circular accelerator the O stands for dipole magnets. Each LHC arc consists of 23 regular cells each with six main dipole magnets and two main quadrupole magnets. Small sextupole, octupole and decapole corrector magnets, the so-called spool piece, are located at the ends of the main dipole magnets to correct their field errors. Other sets of correcting magnets, namely the dipole, quadrupole, sextupole and octupole correctors are installed close to the main quadrupole magnets (short straight section) in order to control the beam parameters.

1.2.2 Insertion region

The insertion regions (IR) have no the same regularity as discussed for the arc region [2]. Each of them has a particular purpose which determines its design. The scheme used in the high luminosity experiments like for instance ATLAS and CMS is very similar in terms of hardware and optics (except for the crossing-angle scheme: the crossing angle in ATLAS is in the vertical plane and in CMS in the horizontal plane). The small β-function values at the IP are generated with the help of a triplet quadrupole assembly. A detailed description of the matching constraints for IR1 and IR5 can be found in [3]. At the interaction point (IP), the two rings share the same vacuum chamber, the same low-beta triplet magnets and the separation dipole magnets. The remaining matching section (MS) and the dispersion suppressor (DS) consist of double-bore magnets with separate beam pipes for each ring.

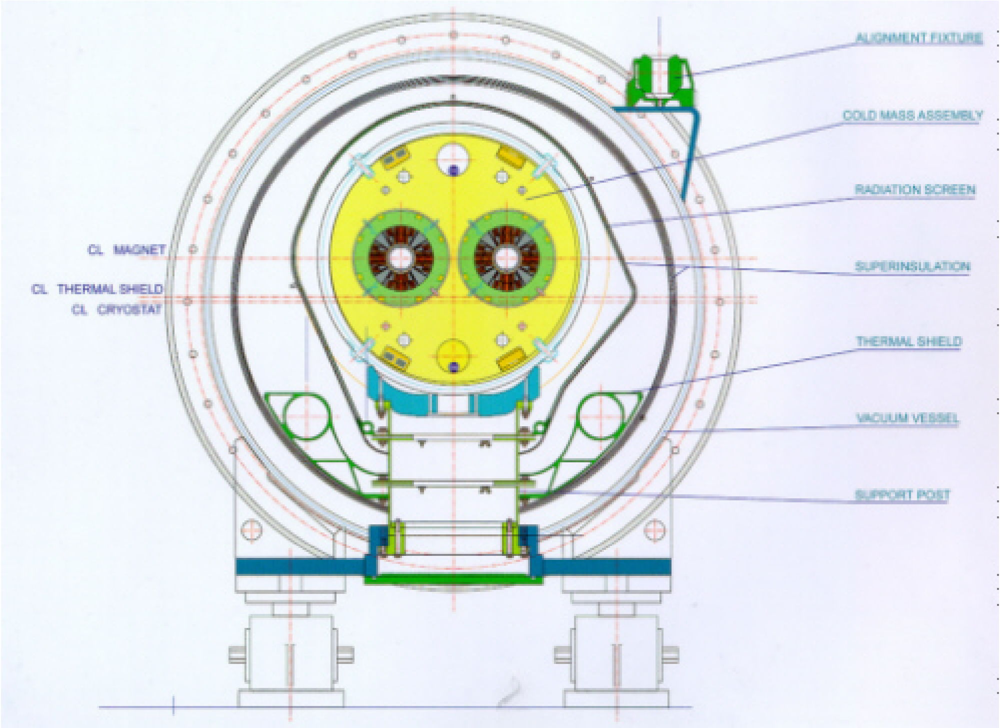

Figure 1.4: The standard LHC arc quadrupole cross section

Apart from the dispersion suppressor the insertions are comprised of the following sections, given in order from the interaction point. A 31 m long superconducting low-β triplet assembly operated at a temperature of 1.9 K and providing a nominal gradient of 205 T/m. A pair of separation/recombination dipoles separated by approximately 88 m. The dipole (D1) located next to the triplet magnets has a single bore and consists of six 3.4 m long conventional warm magnet modules yielding a nominal field of 1.38 T. The following dipole (D2) is a 9.45 m long, double bore, superconducting dipole magnet operating at a cryogenic temperature of 4.5 K with a nominal field of 3.8 T. The bore separation in the D2 magnet is 188 mm and is thus slightly smaller than the arc bore separation, four matching quadrupole magnets. The first quadrupole following the separation dipole magnets, Q4, is a wide-aperture magnet operating at a cryogenic temperature of 4.5 K and yielding a nominal gradient of 160 T/m. The remaining three quadrupole magnets are normal-aperture quadrupole magnets operating at a cryogenic temperature of 1.9 K with a nominal gradient of 200 T/m.

1.2.3 Main circuits

The main dipole magnets are powered in series in each octant. The subdivision of the LHC into octants reduces the stored magnetic energy per dipole circuit. The parameters of the LHC main dipole magnet (MB) and its superconducting cables are summarized in Table 1.2, in Table 1.3 and in Table 1.4. The energy stored at nominal field in one dipole magnet is equal about $7 \cdot 10^6$ J whereas in the one dipole circuit equals to $1.1 \cdot 10^9$ J. The main

Parameter	unit	value
Number of strands		28
Cable width	mm	15.1
Cable mid thickness at 50MPa	mm	1.9
Keystone angle		1.25
Transposition pitch	mm	115
Critical current, @1.9 K, @10 T		>13750 A
1^{st} insulating Polyimide Layer thickness	mm	0.05
2^{nd} insulation LCI Layer thickness	mm	0.068
Copper Cross section	mm^2	15.33
Strand diameter	mm	1.065
Copper to superconductor ratio		1.6
Filament diameter	μm	7
Number of filaments in strand		8900
Twist pitch of filament after cabling	mm	15

Table 1.3: Dipole cable inner layer main parameters

Parameter	unit	value
Number of strands		36
Cable width	mm	15.1
Cable mid thickness at 50MPa	mm	1.48
Keystone angle		0.9
Transposition pitch	mm	105
Critical current, @1.9 K, @9 T		>12960 A
1^{st} insulating Polyimide Layer thickness	mm	0.05
2^{nd} insulation LCI Layer thickness	mm	0.068
Copper Cross section	mm^2	12.56
Strand diameter	mm	0.825
Copper to superconductor ratio		1.9
Filament diameter	μm	6
Number of filaments in strand		6520
Twist pitch of filament after cabling	mm	18

Table 1.4: Dipole cable outer layer and Quadrupole cable main parameters

quadrupole magnets for the LHC are the twin aperture arc quadrupoles (MQ), dispersion suppressor quadrupoles (MQM) and the matching section quadrupoles (MQY). The arc quadrupole magnets are powered in series of 47 or 51 magnets. The quadrupole magnets in the matching section and in the insertion triplet are powered individually or in series of two.

1.2.4 Corrector circuits

The tuning of LHC beam parameters and the correction of the field errors in the main magnets require about 6000 small superconducting magnets operating at currents ranging from 50 A up to 600 A. Because the big power converters can only be located in the caverns at both ends of the eight octants, about 1200 km of wire are required to connect the magnets to the converters. To minimize resistive losses, superconducting NbTi multifilamentary wires are used, which are routed within the cryostat system of the main dipoles and the main quadrupoles. All orbit dipole corrector magnets installed next to the quadrupoles are powered independently via dedicated currents leads. The second group of corrector magnets installed close to the main quadrupole magnets will be connected by 53 m long segments of cable with 42 superconducting wires. The cable will be installed in a tube which is welded to the helium vessel of the main magnets and filled with 1.9 K helium. Corrector magnets which are powered in series in one circuit are members of one family. Families of the so called spool pieces are located next to the main dipoles. The busbars for the spool piece magnets are routed inside the cold mass of the dipoles and the short straight sections. Consequently a splice is required at every magnet interconnect (about every 15 m). The total number of splices in the circuits for spool piece magnets is thus about 32000. The magnets of all other families, like the quadrupole corrector magnets for the correction of the betatron tunes, the sextupole magnets for the correction of the chromaticity and the octupole magnets providing Landau damping are located in the short straight sections, close to the main quadrupole magnets.

Chapter 2

Superconducting magnets for accelerators

The fascinating phenomenon of superconductivity is introduced with emphasis on the so-called *low temperature superconductors* which are used in the high energy physics applications. The difference between the so-called *type I* and *type II* superconductors is explained and the applications of NbTi alloy (type II) in the cables used in windings of the LHC superconducting magnets is presented. The design of LHC superconducting dipole magnets is discussed in terms of the aims of this work. The problem of the stability with respect to irreversible resistive transition is introduced and possible sources of disturbances are pointed out.

2.1 Superconductivity

Superconductivity is a remarkable phenomenon whereby certain metals, when cooled to very low temperatures, become excellent conductors of electricity. Unlike the gradual change of the electrical resistance with temperature in common metals, the superconducting state appears quite abruptly at the critical temperature T_c which is a characteristic parameter of the specific metal. Below this temperature the resistance is not just very small; as far as can be seen from the results of some very sensitive experiments, it is absolutely equal to zero. In addition to the critical temperature, superconductors also have a critical magnetic field, above which they revert from the superconducting state to the normal resistive state. To describe fully the electromagnetic behavior of this matter, it is necessary to introduce also a critical current density J_c to those of T_c and B_c. All this properties are related to each other by the critical surface in BJT space, which is characteristic of the material in question. Superconductivity prevails everywhere below this surface with normal resistivity everywhere above it.

2.1.1 Historical overview

Superconductivity was discovered [4] in 1911 by the Dutch physicist H. Kamerlingh Onnes, only three years later he was successful in liquefying helium. During his investigations on the conductivity of metals at low temperatures he found that the resistance of mercury sample dropped to an unmeasurable small value just at the boiling temperature of liquid helium. Karmelingh Onnes called this totally unexpected phenomenon *superconductivity* and this name has been retained since. The temperature at which the transition took place was called the *critical temperature* T_c.

In the 1933 W. Meissner and R. Ochsenfeld [5] discovered that a superconducting element like for instance lead, completely expelled a weak magnetic field from its interior when cooled below T_c, while in strong magnetic fields superconductivity broke down and the material went to the normal state. This was the first evidence of the intimate relation between superconductivity and magnetic field. Controversially it is not possible to explain the spontaneous expulsion of the magnetic field below T_c in terms of Maxwell equations and indeed turned out to be a non classical phenomenon.

After two years of the discovery, H. and F. London [6] proposed a phenomenological explanation of the Meissner effects but a justification was missing till the advent of the Bardeen, Cooper and Schrieffer theory - the so-called the BCS theory - [7] in 1957. The BCS theory revolutionized the understanding of the superconductivity by the assumption that the carries of the current are not the electrons themselves but couples of electrons with opposite momenta and spins, the so called *Cooper's pairs*. All pairs occupy a single quantum state, the so called *BCS quantum state*, whose energy is separated from the single electron states via an *energy gap*, which turned out to be related to the critical temperature. The BCS theory have predicted several phenomena, like for instance the temperature dependency of the energy gap, the quantization of the magnetic flux and the existence of a quantum interference phenomena, which all have been confirmed by experiments.

A discovery of enormous importance for practical applications was the existence of two types of superconductors with rather different response to the magnetic fields. The element like mercury, lead, aluminium and others belong to so-called *type I* superconductors. They do not admit magnetic field in bulk material and they are in superconducting state when the external applied magnetic field is lower than a critical value B_c. All superconductor alloys like lead-indium, niobium-titanium, niobium-tin and also the pure niobium belong to the large class of *Type II* superconductors. Those materials are characterized by two critical fields B_{c1} and B_{c2}. When the external applied magnetic field is lower than B_{c1} it does not penetrate in the bulk and the material is in the so called Meissner state. When the field is higher than B_{c1} and lower than B_{c2} the magnetic field may penetrate inside of the material in form of flux tubes. The superconductivity breaks down when the external applied magnetic field reaches the upper critical value B_{c2}. In the following sections the importance of Type II superconductors for application is adressed.

2.1.2 Meissner-Ochsenfeld Effect

When an external magnetic field is raised in a perfect conducting cylinder from zero to a finite value B, a surface current is induced according to Lenz's law in order to cancel out the applied field in the interior. Since the resistance in a superconductor is zero, the current will flow with constant strength as long as the external field is kept constant, keeping the bulk of the cylinder field-free. The superconductor acts as a perfect diamagnetic material below the critical temperature Tc. When the external field rises while the temperature is higher than

Tc, eddy currents are induced, which decay quickly because of the resistance, and the applied magnetic field penetrates the interior of the cylinder. If the cylinder is cooled down, at the very instant the temperature drops below Tc, a surface current is spontaneously created and the magnetic field is expelled from the interior of the cylinder. This phenomena is called the Meissner-Ochsenfeld effect and law of induction cannot explain it because the magnetic field is kept constant. But superconductivity is more than just vanishing resistance. The transition between normal conducting and superconducting phases is comparable to different thermodynamic phases. London equations demonstrate that magnetic field does not stop abruptly at the superconductor surface but penetrates into the material with exponential attenuation. The bulk of the superconductor is then field free, but a magnetic field can be tolerated in a thin surface layer. The current flow will therefore be restricted to the same thin layer. The dimension of this conducting surface is determined by a very important parameter resulting from London equations [14], the London penetration depth

$$\lambda_L = \sqrt{\frac{m}{4\mu_0 n_s e^2}}, \tag{2.1}$$

where m and n_s are the mass and density of the Cooper pairs, respectively. For type I superconductors the penetration depth is quite small, 20 to 50 nm. This is a first indication that type I superconductors are not suitable for winding superconducting magnet coils.

2.1.3 Type II superconductors

Type I superconductors do not allow the construction of superconducting magnets since the critical magnetic field is very small. The magnetization curves of transition metals like niobium and some alloys show two critical fields B_{c1} and B_{c2} which are both temperature dependent. These materials are called type II superconductors. Below the critical field B_{c1} the material is in the Meissner phase with complete exclusion of the field from the interior like a type I superconductor. Between B_{c1} and B_{c2} the Meissner-Ochsenfeld effect is said to be incomplete (mixed phase) and the material keeps superconducting electrical properties up to this last value.

The upper critical field B_{c2} can reach high values, which make these superconductors very interesting for magnet coils. The magnetic flux does not penetrate the type II superconductor with uniform density. It is concentrated in flux tubes surrounded by a super-vortex current. The Cooper pair density drops to zero at the center of the vortex, meaning that the core of a flux tube is normal-conducting.

2.1.4 Hard Superconductors

The large upper critical field of type II superconductors permits to flow high currents in the bulk material that, in principle, would allow the construction of accelerator magnets with them. However, there is a problem with the so-called flux flow resistance. The current density exerts a Lorentz force on the flux lines, which begin to move in a direction perpendicular to the current and to the field. This is a viscous motion that leads to heat generation. So, although the current itself flows without dissipation, the material acts as if it had an ohmic resistance. In order to make wires suitable for magnet coils this motion has to be inhibited. This can be done by capturing the flux lines at pinning centers. A type II superconductor is called a hard superconductors when it presents a strong pinning. Hard superconductors are very well suited for high field magnets as they allow current to flow in high magnetic fields without heat generation. The drawback of using hard superconductors is the strong magnetic hysteresis that generates persistent current multipoles. Moreover, some small flux creep effects remain. At finite temperatures a few of the flux quanta may be released from their pinning locations by thermal energy and move out of the material, reducing the magnetization. This effect can be explained assuming a logarithmic decay of the critical current density J_c with time. It implies that for a given temperature and magnetic field the critical current density depends on time. The value J_c can be set after the decay rate has become unmeasurably small. Hard superconductors can, therefore, be characterized by a critical current density as a function of the applied magnetic field and temperature. Early attempts to use hard superconductors for shielding or trapping of magnetic fields faced the difficulty that under certain conditions the super-currents suddenly broke down. In hard superconductors exposed to a high external magnetic field, a small heat dissipation makes the temperature rise, thus reducing the critical current density. This increases the core field resulting in a voltage perpendicular to the current flow and the applied magnetic field. The slightest disturbance will cause the superconductor to reduce its critical current and expel part of the captured magnetic flux. This process is called flux jumping [18]. The stability increases as the conductor dimension along the voltage direction decreases. In order to prevent flux jumping, superconductors that are used to wind magnets are made of multifilament wires.

2.2 Superconducting Cables

The superconducting cable for the LHC are made of NbTi hard superconductor multi-wires embedded in a copper stabilizer. Such wires are wrapped together to form a Rutherford cable type [18].

2.2.1 Multi-filamentary Wires

In order to avoid flux jumping, multi-filament wires (also called strands) are used for magnets. The strands used for the LHC main magnets operate at nominal condition at 423 A for the inner layer main dipole cable and 329 A for the outer layer dipole cable and the main quadrupole cable. A schematic view of a multi-filament wire is shown in Fig 2.1. The filaments are twisted to ensure equal current distribution and to minimize the strength of induced eddy currents due to a changing magnetic field. Eddy currents can have an impact on the achievable field quality and on the quench process. As the filament diameter must be in the range of some μm to avoid flux jumping, a large number of filaments are embedded in a copper matrix that provides mechanical stability and at the same time serves as an electrical bypass of high conductivity and as a heat sink. The main parameters of the multi-filament wire are the ratio of copper to superconductor $r_{cu/sc}$, the cross-section A, the number of

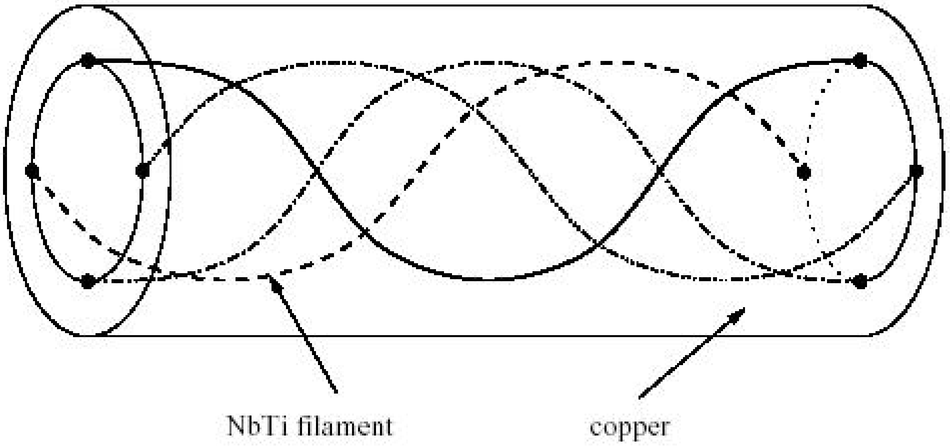

Figure 2.1: Schematic cross-section of a multi-filament wire (strand). Only four filaments are shown for a better understanding. The shown length is the filament twist pitch L_p^f . For the LHC wires this length is typically about 15-20 mm.

filaments N_{fil}, the filament diameter d_{fil}, the filament twist pitch length L_p^f , and the RRR value of the copper stabilizer. For illustration the cross-section of the strand used for the outer layer cable of the LHC dipole magnet is shown in Fig 2.3.

2.2.2 The Wire Fabrication

Multi-filamentary superconducting wires made of NbTi are fabricated in a multi-step process [16]. A cylindrical billet of NbTi is prepared by arc vacuum melting. The alloy NbTi must be produced with high purity and with a variation in titanium contents of less than 1%. From this high homogeneity material, round bars are manufactured with a diameter of about 150 mm and a length of 500 to 750 mm. They are wrapped with a niobium foil of controlled tensile properties and grain size and inserted in a thick-walled can of pure copper (usually RRR>100) with an outer diameter of about 200 mm. The can is closed at the ends by caps that are electron-beam welded. After evacuation the can is compressed and extruded at 600 to 700 ^oC to a composite of about 40 mm. A multiple process of drawing and compaction is performed leading to a long bar of hexagonal cross-section with a width of about 3.5 mm. This bar is cut into pieces of 0.5-0.75 m length. Several thousand of the carefully cleaned short bars are stacked into another 300 mm diameter thick-walled copper tube around a copper rod center. The copper leads are electron-beam welded. Compaction, hot extrusion, and a number of drawing steps with heat treatments are repeated to optimize the critical parameters. The last step can be a coating process (like for the LHC wires) with final shaping or an anodization if required. The niobium foil is a diffusion barrier that prevents the formation of CuTi during the heat treatment, which is brittle and does not reduce in size during the drawing procedure and might damage the filaments. Aiming at very thin filaments, a second or even a third multi-filamentary billet has to be produced from the hexagonal rods of an intermediate stage. The final wire may contain up to 100 thousand filaments of some μm in diameter (6-7 thousand for the case of the LHC dipole wires).

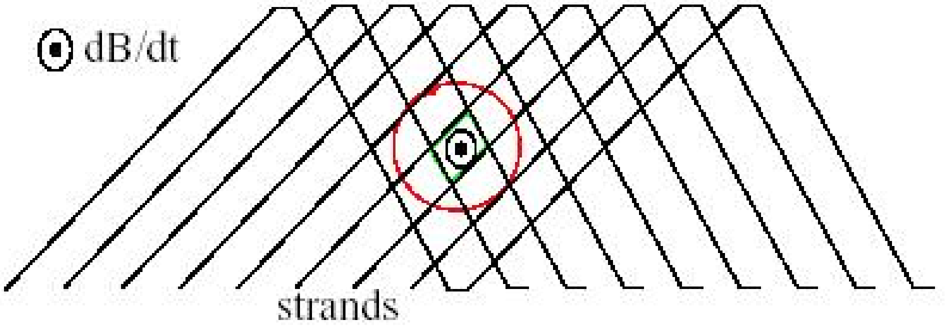

Figure 2.2: Sketch of a Rutherford cable: strands cross each other and form a two layer structure. Eddy currents are induced that flow through the contact resistances when the applied magnetic field changes

The production aims at a continuous length of several tens of kilometers with reliable reproducibility of the critical current characteristics [17].

2.2.3 Rutherford Cables

The superconducting cable for the LHC main dipole magnets with nominal field of 8.33 T at an operating current of 11.85 kA are made of several strands (28 for the inner-layer and 36 for outer layer, this last cable is also used for the quadrupole coils and busbars). As for the filaments, the strands are twisted. The strand twist pitch L_p^s is 11.5 cm for the inner dipole cable and 10.5 cm for the outer. The strands are compressed into a flat two layer structure with a trapezoidal shape, the so-called Rutherford cable (see Fig. 2.2 and Fig. 2.3). The cable is permeable to liquid helium so that the surface of all strands is wetted with the coolant. The insulation of the cable must have a high breakdown voltage, be elastic at room and liquid helium temperature, and radiation hard. The LHC Rutherford cables are insulated by wrapping polyimide films around the cables.

2.2.4 Cabling Procedure

The Rutherford cables are produced with machines equipped with the necessary number of wire spools. The wires are guided around a conical mandrel and then rolled to the required trapezoidal cross-section shape by an assembly of rollers, named *Turk's Heads*. Care must be taken to avoid strand breaks as well as burrs and sharp edges on the cable surface which may puncture the cable insulation and lead to electrical shorts in the coil. In some cases a final shaping process may turn out to be necessary. Within any magnet coil all strands should be of a continuous length without internal welds. In order to control the cable geometry online devices have been invented that periodically clamp the cable with a preset compression up to 70 MPa, and measure the width, the average thickness and the trapezoid angle. A satisfactory cable fabrication is achieved if the degradation of the critical current is less than 2%. The cabling also reduces the RRR of the copper [17, 18].

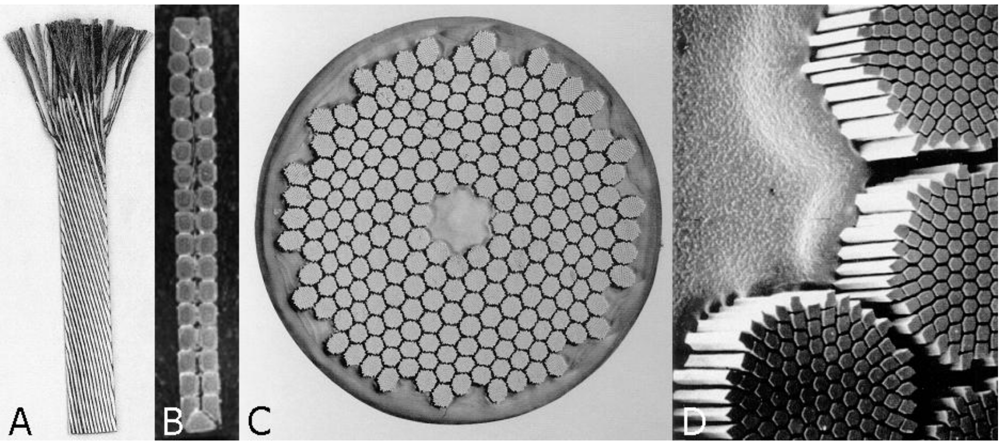

Figure 2.3: A) A superconducting Rutherford cable; B) A cross-section of the cable; C) A cross-section of an individual strand of the cable, with the NbTi filaments in a copper matrix; D) A close-up of the NbTi filaments

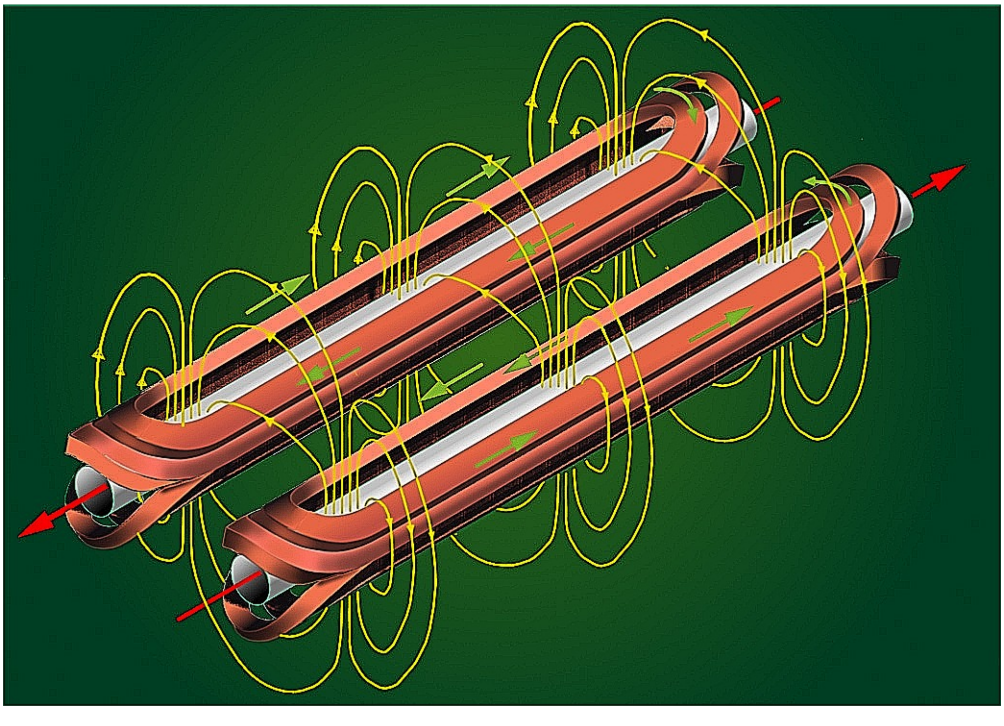

Figure 2.4: The superconducting cables loop around the beam pipes inside the dipole. For each beampipe the upper half of the inner layers of cables is drawn blocked together, as is the upper half of the outer layers and the lower halves of the inner and outer layers. The left beampipe is on the external side of the dipole and the right beampipe is on the internal side.

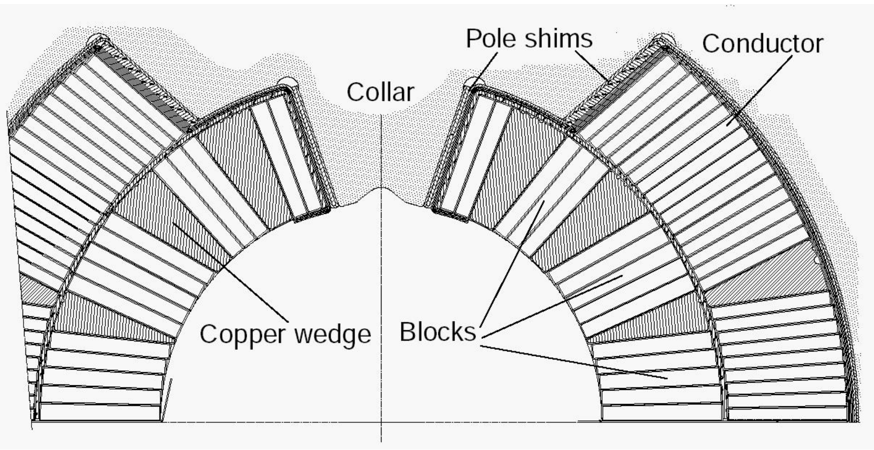

Figure 2.5: The LHC dipole cross section. The two layers and the six-blocks structures have been optimized to produce an homogeneous dipole field

2.3 LHC superconducting dipoles

A dipole magnet is like a split pair of circular coils stretched along the particle trajectory in such a way that the dipole field is generated only along the beam pipe, as shown in Fig. 2.4. It can be shown that current layer having an azimuthal profile of the surface current density J_s varying like $cos\theta$, generate a perfect dipole field. The same result is obtained with uniform volume current density J in a coil cross-section with an azimuthal profile varying like $\cos\theta$. this configuration is the one obtained by the intersection of two cylinders carrying uniform but oppositely directed current densities. In practice this configuration is approximated by shells of currents with suitable azimuthal angle. The final design of the LHC dipole magnets is sketched in Fig. 2.5. It is based on two layer design where each of them is subdivided in blocks. The final geometric structure is made of six blocks, four in the inner layer and two in the outer. Since the field in the outer layer is considerably lower than in inner one, it is natural to take advantage of the steep increase of J_c at lower field region by reducing the superconductor cross section in the cable of the outer layer. For example, at 4.2 K NbTi more than doubles its critical current in passing from 8 T, Jc 1100 A/mm^2, down to 6 T, J_c 2300 A/mm^2. The cable cross section cannot be reduced accordingly because a minimum amount of stabilizer must be retained, in order to avoid a too strong dissipation during a quench. In practice, by proper grading of the current density, the ampere-turns in the outer layer can be increased by 50-70%, with great advantage for the field strength generation. For such reason the two layers of the LHC dipole magnet are made of different cables.

2.3.1 Coil Winding

The Rutherford cable is wound on a mandrel with a variable tension of up to 200 N. The baking moulds are stacked from punched steel laminations providing a geometrical accuracy of about 20 μm at any cross-section. After the winding, the coil is cured with a mould placed on the top of the coil package that covers the entire length and the assembly is moved into a hydraulic press. It is worth mentioning that the heat treatment during the curing process increases the RRR value of copper.

2.3.2 Splices

The joints between cables of different windings (top and bottom poles and dipole of the two apertures) are accommodated outside the coils. On the contrary the splice between inner and outer cable of the same pole must be done in situ, during winding, and is fitted inside the winding. Splices must have a low resistance, typically below $1\,n\Omega$ at high field, and they are critical elements from the point of view of the reliability of the magnet. To avoid splices inside windings, placed by definition in a high field region, a two layer magnets can be wound from a single cable length using the double pancake technique. This of course implies that the advantage of the current density grading is relinquished. The LHC arc quadrupoles (collaboration CEA-CERN) are wound in this way, using identical cable to that used in the outer layer of the dipoles.

2.3.3 Collaring Procedure

The resultant of electromagnetic forces per unit length of an LHC dipole in a coil quadrant at nominal operation condition is about 1.7 MN per meter length. A strong structure is needed to take over this force. It is formed by collars clamped and pressed around the coils to obtain a pre-compression in the coil winding. The pressure is maintained along the whole magnet by means of pinning rods that lock the upper half collars to the lower half ones. The collars restrain the coils in the radial direction, like a tube, but also squeeze the coils in the azimuthal direction by means of the wedge in the pole region, at 90 degrees from the midplane. The azimuthal pre-compression has to be at least as high as the e.m. forces: when the magnet is excited the action of the e.m. forces is, in first approximation, to release the pressure at the interface between collars and coils with no coil movement. The collar-coil interface near the pole is shown in Fig. 2.6. Collaring is a very critical operation and is done by means of large presses capable of exerting about 20 MN/m. A typical compression on the coils of 100-150 MPa is applied, with a residual stress of 60-90 MPa when the external pressure is released. The collars are made of 5 mm thick laminations, produced by fine blanking using special stainless steel with very low magnetic permeability ($\mu_r < 1.005$ while at cold and under stress). Usually collars are not sufficient to take over the whole magnetic force and that is why also the yoke has to be compressed against the coils by means of an external shrinking cylinder made of stainless steel. The shrinking cylinder serves also as helium vessel. It is fitted onto the yoke assembly by welding two half shells along the whole length of the magnet. By means of a "calibrated" welding of the two shells the shrinkage can be more or less controlled. This is a very difficult operation to carry out with reliability and good repeatability and could be avoided if the collars are self-sustained, as it is in the design of the LHC arc quadrupoles and the American LHC IR quadrupoles. The LHC dipoles, also in consideration of the twin design have been designed with 40 mm wide radial extension stainless steel collar, a choice that is safe for field beyond 9 T. In an alternative design one can use very narrow 'skin' collars, just few millimeters wide, intended for locking the coils

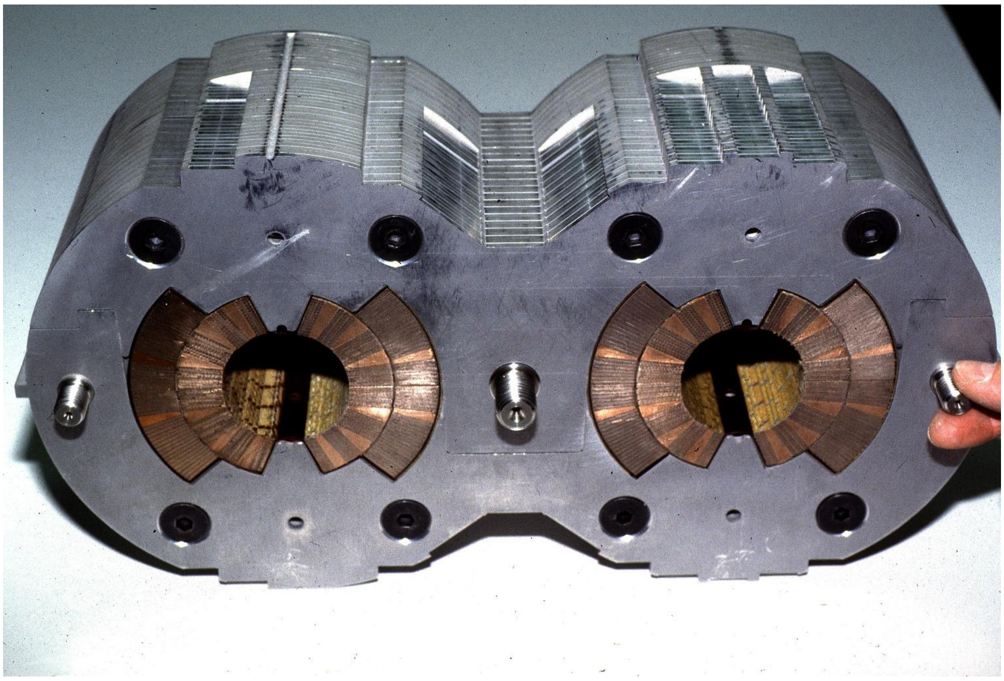

Figure 2.6: The cross section of collared LHC dipole coil

in the proper position and for coil handling. In this case almost all forces are kept by the yoke-outer cylinder structure, with the advantage of a 3-5% enhancement of the field, due to the closer vicinity of the yoke to the center (dipole D19 of LBNL, CERN first LHC IR quad, Japanese LHC IR quad). Of course the design should take into account the non uniform spring back of the materials when the press is released, the eventual plasticity of critical points, like the locking rod holes, the effect of the differential thermal contraction of the various materials and, what is most difficult, the role of friction at various locations. Care and attention during assembly and the quality control of the components leads to the desired prestress in operating conditions. For example, the dimension tolerance of cables is $6\,\mu m$, collars have profiles with an accuracy of $20\,\mu m$ and the total assembly must be controlled to the level of $50\,\mu m$.

2.3.4 Coil Ends

Coil ends are usually difficult to design, since each turn has to climb up around the beam tube, as shown in Fig. 2.4. The saddle-type bend has a complicated 3-D shape and has been the object of various studies both for mechanical stability and for magnetic design. The cable turns are bent and then kept in position by inserting *end spacers*. The end spacers are designed according to the principle of minimum strain energy or the equal perimeter [1] and are precisely machined in fiberglass-epoxy composite. The ends also require special attention during collaring: here the roman arch is far from perfect, so the collaring must be more gentle. Coil ends are usually surfaced with a partial resin impregnation in order to finish the outer surface and to fill eventual gaps in between conductors and end spacers.

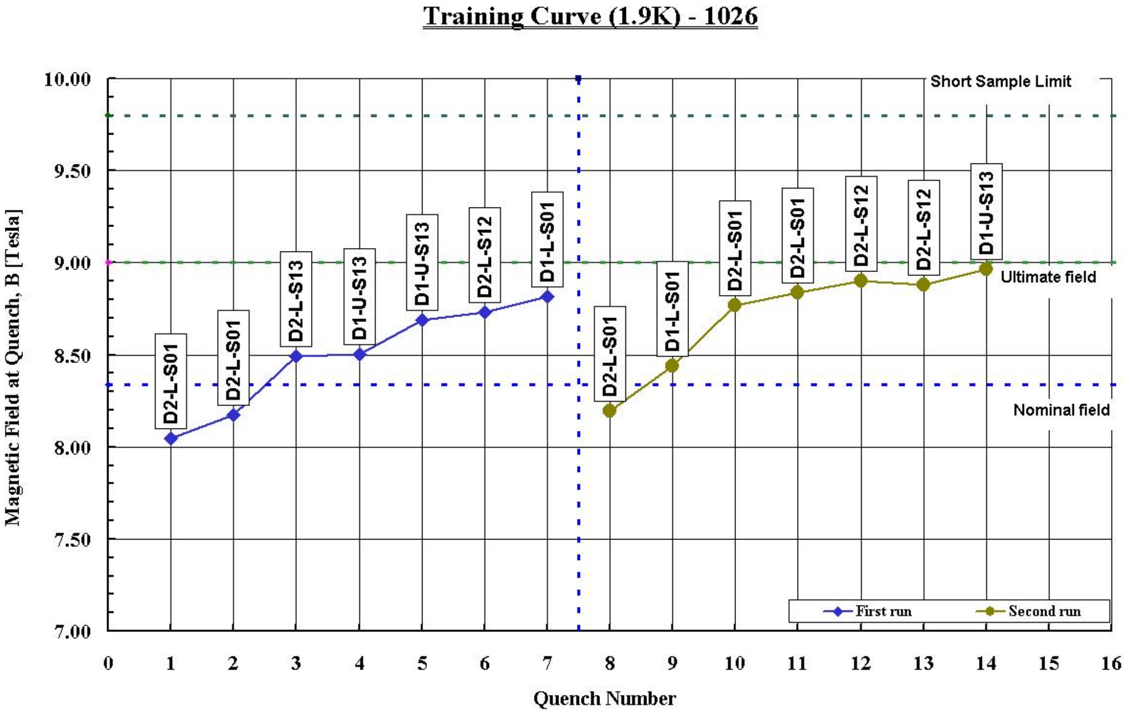

Figure 2.7: The so called training curves. The low performance exhibited by this particular magnet caused its rejection. The slow training, 7 quenches without reaching 9 Tesla, the low memory after the thermal cycle and the small detraining are the signature of a problematic magnets which cannot be considered enough reliable to be installed in the LHC.

2.4 Quench performance

The power performance of a superconducting magnet can be lower than the one expected from the measured performance on a cable short sample. A permanent degradation of the cable caused by the winding and collaring procedure is expected to be in the order of few percents below the critical current measured in the cable short sample and its value is expected to be fixed. On the contrary the tests performed on the LHC dipole magnets confirmed that the performance is a function of the powering history, as already experienced in previous projects. While at a first trial the maximal current reached before quenching is usually much lower than the expected value, at the second trial the quench current can be significantly higher. This phenomenon is usually referred to as *quench training*. It has been observed that several powering tests can enhance the current very close to the expected conductor limit. This is not true for all magnets and depends on the quality of the winding, the collaring procedure and the possible accidental damage that can happen during the production. Few magnets which have been finally rejected has not shown a fair training behavior, on the contrary several of them has behaved as meta-stable object which sometimes during the powering history lose the "memory" and shift back to the previous low-performance state. This is usually referred to as *detraining* effect.

2.4.1 Training and Detraining

The capacity of a magnet to improve the performance after repeating powering tests is usually refereed as the training behavior. For the LHC dipole magnet the target is to reach the ultimate field in a maximum of 7 quenches. A "fair" magnet, with respect to the statistics accumulated so far, is expected to exhibit a maximum of 3 quenches before reaching the ultimate field of 9 Tesla. If the magnet does not reach the target, a thermal cycle is performed and a second test run is done. If the magnet does not reach the expected performance during the second run it is refused. In Fig. 2.7 example of a magnet with long training is reported. During the first run the magnet started with a quench slightly above 8 Tesla and during the next powering the field has always improved even if the gain in quench field form a quench to the next one has never been very large. During the first run the magnet never reached 9 Tesla and exhibited a positive but very slow training behavior. During the second run it never reached 9 Tesla and moreover the 12^{th} and the 13^{th} quench the magnet shift back to a lower field value, a clear detraining. A very slow training and one point of detraining are the signature of a problematic magnet which does not have enough memory to be considered reliable for the LHC machine.

2.4.2 Mechanical Activity versus Training

The degradation of the quench training performance with respect to the cable short sample performance and the underlaying memory in the training behavior are the emergency properties which cannot be referred to the behavior of the magnet components. The evidence of quench precursors (usually referred to as *spikes* for its shape) observed on voltage taps and simultaneously on quench antenna suggested to analyze in details the powering history. During the first energisation several thousands of such signals are present and the current research investigate the possible correlation between the spikes statistical properties and the quench performance. As it is discussed in details in chapters 6-7 the spikes has a mechanical origin which is related to cable motion within the magnet coil induced by the Lorentz forces. Moreover the quenches are manly located in the magnet extremities which indicates them as the weak points in which a different mechanical behavior is expected with respect to straight part.

Chapter 3

Test facility

The main magnetic system of the LHC consists of 1232 twin aperture, high-field superconducting dipoles and about 500 twin-aperture, high-gradient superconducting quadrupoles. All these magnets, prior to their installation in the accelerator tunnel, are tested in 1.9 K cryogenic conditions. The tests are carried out at CERN at a purpose build Superconducting Magnet Test Plant (SMTP). The main features of this test facility are summarized including its operation modes. The cryogenic system of the test facility, requiring 12 so-called Cryogenic Feed Boxes (CFB), is introduced and the procedures used to cool down magnets to 1.9 K are described. The main characteristics of the powering system and the topology of the electrical circuits are presented. The main test equipment used to performed the power tests is outlined. In particular the anti-cryostats used for keeping the magnet apertures at room temperature and making them accessible for warm measuring equipment are presented. The standard antennas used for quench localization and spikes detection are described in details and the techniques used for compensating the signals from the pick-up coils are explained. The acquisition systems used for recording the voltage signals coming out from the magnets sensors and from the quench antennas is described.

3.1 The standard test sequences for the LHC main ring magnets

The dipole and quadrupole cold masses are delivered to CERN where they are equipped with cryostat. When this procedure is finished the magnets are transported in a big hall called sm18 in which all the necessary infrastructures needed to cold test them is available.

3.1.1 Cold test benches

Cryogenic and electric feeding is done through the CFBs connected to one end of the magnet. A magnet return box (MRB) closes the opposite end of the cryo-magnet under test. The functions of the CFB are to control the cool down and warm up of a cryo-magnet, to maintain a magnet cold mass in saturated liquid helium at 4.5 K or in pressurized superfluid helium at 1.9 K for magnetic measurements, power tests and quench training. The CFBs were optimized to recover as much liquid helium as possible after a quench and to automatically

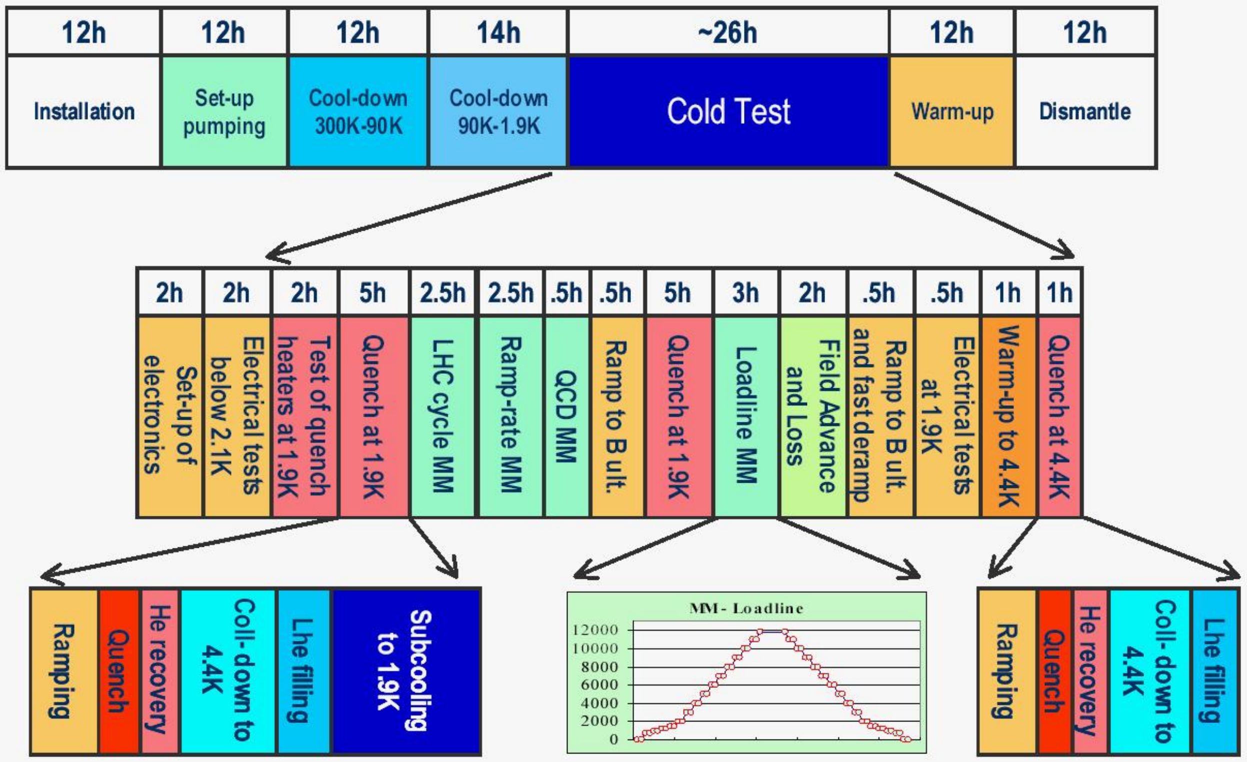

Figure 3.1: Main phases of the standard test cycle for the LHC main dipole

cool down the magnet again. They also contain all the current leads for the main coil and for the auxiliary corrector magnets. As the magnetic measurement equipment only operates at ambient temperature, the beam screens [] required during the accelerator operation are not mounted in the magnet apertures to permit insertion of the so-called *anticryostats* [8], which allow the use of measuring shafts at room temperature for quench location and magnetic field measurements. As from summer 2004 the SMTP consists of twelve test benches grouped in six clusters. Every cluster is supplied with one set of main and auxiliary power converters shared between the two test benches belonging to a cluster. Standard test sequence for the LHC main cryo-dipoles is shown in Fig. 3.1 Individual phases of the cold tests are briefly described in the following paragraphs.

3.1.2 Installation Phase

The cryo-magnets after their final preparation for the cold tests in the assembly hall (SMA18) are transported by means of the *ROCLA* (Fig. 3.2) transport vehicles to one of the test benches in SMTP. There the magnet under test is first placed onto three support posts anchored to the test bench base structures. After a set of electrical reception tests the magnet is aligned vertically and horizontally and all electrical, hydraulic and anti-cryostats connections to the CFB unit are formed and are followed by the tests simulating magnet contraction during the cool down phase. The MRB, which closes the opposite end of the cryo-magnet is anchored to the force retaining supports of the base structures. The test bench base structures are design to retain all mechanical forces appearing during the tests

Figure 3.2: The ROCLA, the special vehicle design for the trasportation of the LHC superconducting dipole magnet.

and to guarantee alignment and stability of a cryo-magnet throughout the test campaign. The installation of the thermal shield in the connection zone and closing of the vacuum vessel by means of a dedicated bellow accomplish the installation phase.

3.1.3 Setting-up and Pumping Phase

When all electric, hydraulic and vacuum connections are completed and tested, three pumping purges between P1 (1000 mbar) and P2 (20 mbar) are executed followed by an internal leak test performed by means of the integrated leak detector in the CFB. The signal is typically below 10^{-6} mbar l/s at a pressure of gas He in the magnet of 1.5 bar. In the next stage the insulation vacuum of the CFB and magnet is pumped down to 10^{-3} mbar and globally leak tested.

3.1.4 Cool down to 90 K

The cool down from 300 to 90 K is done by helium gas pre-cooled with liquid nitrogen in a dedicated heat exchanger, which is not part of the CFB. The cold helium gas enters the system and passes through the magnet and the magnet thermal shields. Both flows are controlled such as to pass the maximum possible flow through the cold mass and at the same time to maintain the thermal shield at nominal temperature.

3.1.5 Cool down to 1.9 K

Once a cold mass is filled with saturated liquid helium it can be cooled further down to its working temperature of 1.9 K. For this purpose the CFBs are equipped with a low-pressure circuit connected to a liquid/liquid heat exchanger built in the magnet. The liquid helium is pre-cooled in a liquid/gas heat exchanger with cold low-pressure gas, which is pumped via a valve controlling the pressure. The maximum flow rate capacity of the pumping circuit is 18 g/s at 15 mbar.

3.1.6 Cold Tests - Powering the Magnets

The tests and measurements performed on the LHC main ring magnets require not only the nominal operating cryogenic conditions but also the nominal operating powering. In order to power the magnet coils, the CFBs are equipped with one pair of main 13 kA current leads and two pairs of 1 kA auxiliary current leads, see Fig. 3.3. The magnet coils are operating in pressurized superfluid helium at 1.9 K and 1 bar and all current leads are operating at saturated liquid helium at 4.5 K. For this reason the so-called lambda plates physically separate the two helium circuits. The two dipole coils, being part of the LHC two-in-one dipoles are powered in series making use of the main 13 kA current leads. Auxiliary magnets are also power tested, in particular 100% of the pre-series cryo-dipoles and 10% of the series. In the case of the MBA dipole type, two auxiliary circuits are formed. The first circuit consists of two sextupole correctors (MCS) and two decapole correctors (MCD) all connected in series and powered through the first pair of 1 kA auxiliary current leads. Second auxiliary circuit consists of two octupole correctors (MCO) connected in series and powered through the second pair of auxiliary current leads. In the case of the MBB dipole type the first circuit consists of two sextupole correctors (MCS) connected in series. The second auxiliary circuit contains the remaining auxiliary busbars connected in series. Similar powering schemes are also used for the main ring quadrupole magnets. On the test benches, powering of magnets is performed up to an ultimate current level. For the LHC main dipole and quadrupole magnets, so-called quench tests are carried out. During the quench the liquid helium around the coil vaporizes and the pressure increases rapidly up to about 16 bars. A mixture of gas and liquid helium passes through a "quench" discharge valve into a decanter of about 400 liters volume. The gas can partially leave hydraulic circuit of the CFB-magnet assembly through the recovery line and/or partially through the low-pressure line. The liquid helium remaining in the decanter is used for re-cooling the cold mass after a quench if required by the test program.

3.1.7 Electrical Tests

The electrical measurements are an essential part of the tests performed in SMTP on the LHC cryo-magnets. These test verify magnet electrical integrity and qualify electrical circuits for the power tests on the test benches and for the future use in the machine. Electrical tests are executed several times during each test campaign. It is obligatory to perform relevant tests after each operation that can affect electrical integrity of a magnet, both at ambient and cryogenic temperatures. Main operations that are considered important for the electrical integrity are: cool-down due to resulting thermal contraction of the magnet coils, quenching and finally warm up of a magnet. A typical sequence of electrical tests for the pre-series magnets is shown in Fig. 3.1. The results of the electrical tests are of "go"/"no go" type and are decisive for the future of every magnet.

3.1.8 Power Test

The importance of the cold tests is not only related to the magnet quench training, but first of all they allow qualifying of the magnets' cryogenic, vacuum and electrical integrity. Magnet acceptance is given only if all these aspects are conform to specifications. The power tests carried on the LHC pre-series dipoles seek to qualify the magnets in terms of the number of training quenches necessary to reach nominal (8.33 T) and ultimate (9 T) field levels. The provisional acceptance criteria require the nominal field to be exceeded after no more than the 2^{nd} quench and the ultimate field after no more than 7^{th} quench. The first 30 dipoles (3 times 10 from the three production companies) were undergoing an extended test program, also validating the magnet property of keeping the "memory" of quench training after a thermal cycle. For this purpose the tests were typically carried out in two to three runs separated by thermal cycles from 1.8 K to room temperature and back to 1.8 K. The results of this extended program of tests permitted the establishment of final acceptance criteria and verification of test procedures.

3.1.9 Warm-up Phase

At the end of the measurement campaign at cryogenic temperature the magnet is quenched, also in order to vaporize most of the liquid helium. The heaters installed inside the decanter and in the phase separator boil off the reminder of the liquid helium. Once the liquid helium is evaporated, the magnet is warmed up to room temperature with a flow of warm helium gas using the same hydraulic circuit as during the cooling phase.

3.1.10 Dismantling Phase

During this last phase of the test cycle, the cryo-magnets are disconnected from the cold test stands in inverse order with respect to that of the installation phase. The tested magnets are transported by means of the ROCLA transport vehicles back to the assembly hall SMA18 for further warm magnetic measurements and preparation for the storage.

3.2 Anti-cryostat

The necessary measurement conditions for quench location and magnetic field measurements shaft that operate at room temperature are provided by a warm bore anti-cryostats, which are well insulated, single-walled tube, kept at room temperature by low-voltage coaxial heating wires. Each magnet aperture is equipped with an anti-cryostat so that it can be measured individually with measuring shaft and other various types of instruments. The anti-cryostat [8] is built as a coaxial tube system, consisting of a seamless, cold drawn pipe of stainless steel 316L with an inner diameter of 40 mm and a wall thickness of 0.7 mm. The tube is equipped with four mineral-insulated coaxial heater cables with an outside stainless-steel jacket of 0.5 mm diameter and an inside conductor of 0.09 mm diameter. Each of them forms over its total length a loop which is soft soldered in the form of a helix around the outside surface of the warm bore. The incoming and the outgoing cable part of each loop must be soldered together as close as possible to avoid formation of parasitic magnetic fields by the heater loops. Supplied with a maximum current of 1 A and a maximum voltage of 30 V, each heater can either warm up the anti-cryostat from cryogenic temperatures up to room temperature or - the common case during measurement operation - maintain the warm bore

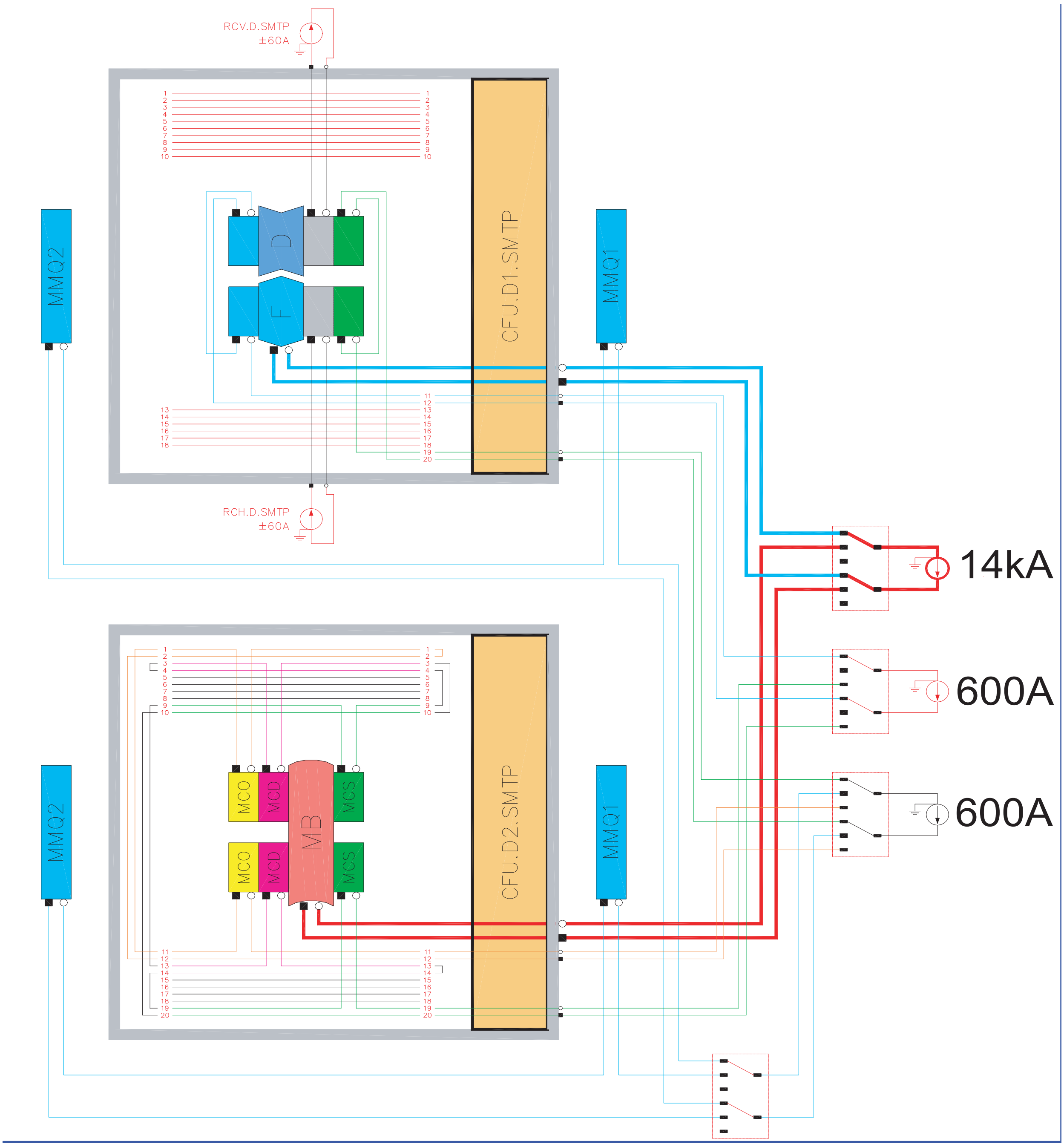

Figure 3.3: The power supply and the electrical circuit per cluster in SMTP.

at room temperature. Each heater can dissipate a maximum of about 2 W/m heater length while the average dissipation during normal operation is around 0.8 W/m for all four heaters in one aperture. An aluminum ribbon is wrapped around the warm bore and the heaters in order to reduce the emissivity of this surface. Small gaps are left between the turns which help out-gassing during vacuum pumping of the magnet cryostat. On top of the aluminum ribbon two blankets of multi-layer super-insulation (MLI - each has 4 layers separated with net-type sheets) are installed in a way that any gap of the inner layer is covered by the outer one. This guarantees a minimum of heat losses by thermal radiation. Mainly for reasons of mechanical protection the MLI is then covered by a thin-walled stainless steel tube, the external screen. In order to facilitate the assembly, this tube is cut in 700 mm long segments and mounted step by step together with the MLI. The segments are connected end to end in a way that they form a continuous tube over the whole length of the anti-cryostat. A pin with a diameter of 6 mm is fixed on every eighth tube segment and is kept in place by a U-shaped stopper which is soft soldered previously on the warm bore. This is to avoid a movement of the screen tubes relative to the warm bore due to differential thermal expansion and during the installation in a magnet. A 10 μm silver layer on the inside and outside surface of the tubes reduces their emissivity and improves further the thermal behavior of the anti-cryostat.

3.3 Quench antenna

As discussed above the LHC dipoles are equipped during tests with an anti-cryostat (a warm bore) with a 40 mm inner diameter. This imposes a maximum outer diameter of 36 mm to the shaft of the quench antenna, to leave enough clearance for installation and operation. Mechanical tolerances, bending stiffness requirements, equipment handling and, last, cost issues have driven the design of the shaft towards a modular solution. A 16 m shaft is obtained by assembling 13 modules of approximately 1.25 m length each. This covers the 15 m length of the LHC Dipole and the adjacent corrector magnets. All modules are identical and designed to allow interchange of position and easy management of spares, Fig 3.4. Ceramic (Al_2O_3) has been chosen as support material because of the high rigidity and geometric stability, both mandatory for proper calibration of the coil sensitivity. In addition ceramic is non-magnetic and nonconducting, thus can turn freely in a magnetic field without perturbing it. Because of their hardness, ceramic materials are difficult to machine. This has driven the design of the support towards a simple geometry, i.e. a hollow cylinder equipped with tangential coils. It has been developed at CERN a technique to wind coils on glass-reinforced epoxy supports using a dedicated winding machine. Each coil is calibrated individually and matched to other coils with the same cross section to achieve the highest possible dipole compensation ratio. Coils are mounted onto reference surfaces machined along the outside of the ceramic pipes

Figure 3.4: The longitudinal view of the assembly of the quench antenna sectors

and fixed to it with precise dowel pins (see Fig. 3.5). Flatness and parallelism of this fitting is better than 20 Pm. For the purpose of magnetic measurements a single coil would be sufficient to perform the measurement. Three symmetric coils, however, offer the possibility of quench localization and several advantages such as flexibility in magnetic measurements, including the possibility to verify the measurement accuracy using symmetry properties, and better rotational inertia properties. A number of different, standardized longitudinal positions have been defined and optimized for the exigencies of magnetic measurement of the dipole and associated correctors, quench localization and calibration. Moreover, as the coil includes an additional module, in situ cross checks can be made by shifting the axial position of the coil by the length of one unit. As shown in Fig. 3.5, each coil module is completed at one end with a ceramic (SiN) flange that houses an integrated ceramic ball bearing in a brass cage equipped with beryllium-copper rollers. At the other end a small Ti-bellows is glued on the module. The titanium bellows has a flange mating with the opposite ceramic support, so that the modules can be mechanically assembled. The function of the bellows is to accommodate the curvature of the dipole cold bore (0.4 mrad at each junction) as well as the anti-cryostat centering errors in vertical and horizontal direction. It guarantees however high torsional rigidity, as required for the measurement of the dipole field direction. In addition, its small size and high electrical resistivity are such that eddy current effects are negligible.

Once assembled the modules are supported at each junction by the ceramic ball bearings, either directly through the flange or indirectly through the bellows. The outer races of the ball bearings sit in bronze cages, fitted with fixed and spring-loaded rollers that allow longitudinal movements along the anti-cryostat as necessary during installation and removal of the complete shaft. During the rotation of the shaft the outer race of the ball bearings and the bronze cage remain stationary. Hence no perturbation due to induced eddy currents can occur. The frictional torque for the whole shaft is 0.03 Nm, extremely small thanks to the high quality of the ball bearings. This torque results in a maximum twist of 0.0026 mrad along the shaft. In order to pass the signals from all coils in a modular manner we have fitted each module with 39 twisted pairs guided inside the ceramic pipe aside the central coil and equipped with micro-connectors at both ends of each module. This system allows interchanging of modules without need for re-cabling the complete shaft. The main disadvantage is that the signals from modules at the far end of the shaft are connected to the acquisition system through all other intermediate modules. This leads to an increased number of interconnections. The link from the rear of the coil to the outside rotating unit located at a distance of 1.4 m, is made by an interconnection ceramic pipe fitted with the necessary cables and plugs. In addition the end of this interconnection pipe is equipped with

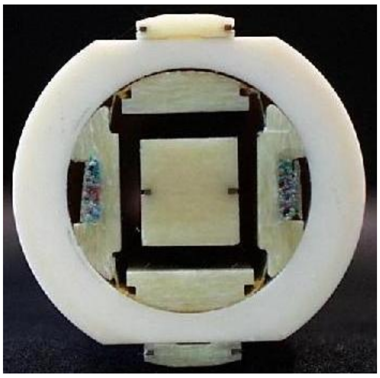

Figure 3.5: The cross section of the quench antenna. The three pick-up coils are visible, one in the top, one in the middle and the the last on the bottom. All pick-ups have the same polarization.

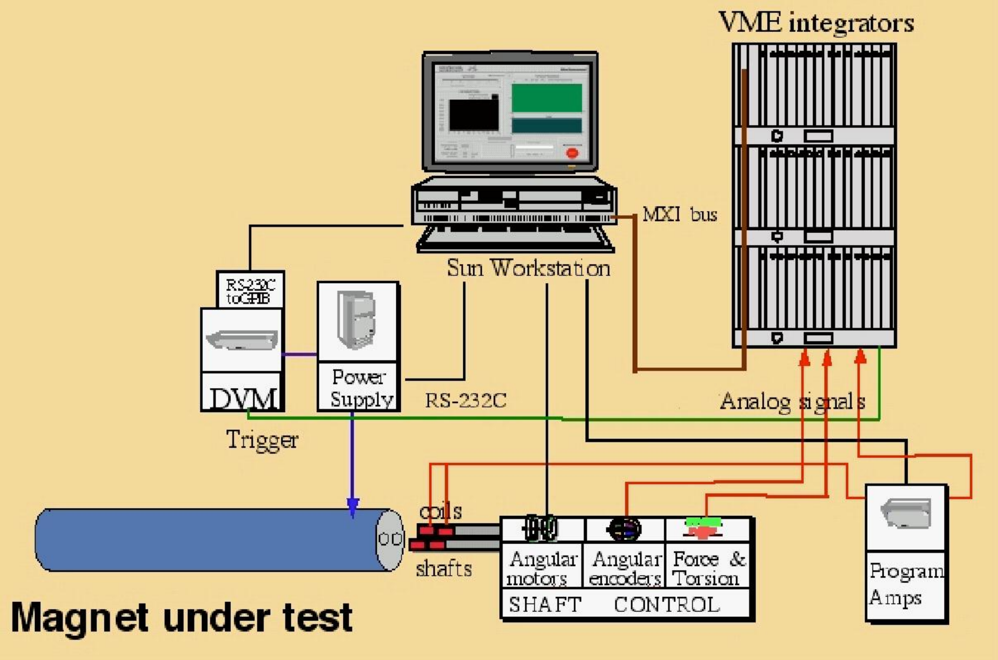

Figure 3.6: Scheme of the measuring system used for the cold tests of the LHC superconducting dipole magnets

a reference surface that provides the angular fiducial for all coils.

3.4 Compensation Scheme and Acquisition System

All signals coming out the QA enter into a connection box to be properly ordered before entering in the electronic charts in which the difference is done. There are two main compensation scheme adopted, the transversal (TC) and the longitudinal one (LC). In the TC the three signals in one longitudinal section are differentiated two by two. This operation gives as results other three signals but no more independent. In the LC two signal belonging to different longitudinal sections are differentiated. The choice of the sections is done taking into account the natural mode of vibration of the antenna. During this filtering procedure some information is lost but the signals left has a noise to signal ratio much lower. Actually the not compensated signal is not easily distinguishable from pure noise. This compensation reject the noise from mechanical vibration [15] but it is affected by a pulsing noise of electrical origin which may be related to the power converter. The LC is less effective in rejecting mechanical noise but it has demonstrated to be robust with respect to the previous electrical noise. In chapter 6 the rigorous treatment of those signals and the cross check between different compensation scheme for spikes detection is addressed in very details.

Finally 120 compensated signals enter a A/D converter with a maximal frequency of 50 kHz per channel. The maximal time recorded is 300 ms. There is the possibility to transfer the samples into a bigger memory before being ejected but the buses are limited in frequency and cannot be pushed more than 8.33 kHz. The typical frequency used for this second step is 5 kHz and 150 s may be recorded.

Chapter 4

The Quench Process

A fair understanding of the electrical and thermal processes undergoing a restive phase transition in a superconducting cable of a magnet coil is essential to interpret correctly the associated voltage build-up and to analyze the read out signals of the quench antenna (see section 5.6). Results of the analysis of such signals with respect to cable stability and magnet protection issues, gives an important feedback during the design and prototyping phase of the devices, and serve as a powerful quality control means, during the production and testing.

The standard mathematical tools for the interpretation of the experimental results are summarized starting from the general three dimensional heat balance equation in a solid body down to the estimation of the so called *quench-load*, which is currently used for a first estimation of the hot spot temperature evolution. In the second part of the chapter computer simulations of the two wire networks obtained by means of purpose developed code, SPQR (Simulation Program for Quench Research) are presented for the LHC Rutherford cables. The implemented model is suitable for the investigation of the current redistribution induced by a resistive transition. The design of mixed wire cable is discussed in terms of the possible increase of the quench propagation velocity and simplification of magnet protection system. At the end of the chapter a proposed formalism for multi-wire cables in adiabatic conditions is presented and references in the subject are provided.

4.1 Heat balance equation

In a superconducting wire which quenches, the thermal and electrical behavior are closely coupled because the current in the quenched wire generates heat and the resistivity of copper strongly depends on the temperature. The design of a superconducting system carrying high current requires a good comprehension of the wire temperature as a function of the current during the whole magnet quench process. The equation that describes the temperature evolution of a system is the heat balance equation. The solution for this equation can only be found with numerical methods, because of the strong nonlinear temperature dependence of the material parameters [18, 17]. With a given initial temperature profile and appropriate boundary conditions, this equation describes the time evolution of the temperature in each point of the system.

The three-dimensional heat balance equation is the most general model to describe how the heat is flowing inside a solid body and consequently how its temperature changes with time. This equation belongs to the family of the balance equations which are common to all the transport problems (electric, hydraulic, etc.) and are the standard tools used in the characterization of the out of equilibrium systems. The basic assumption is the conservation of the energy. Fig. 4.1 shows an infinitesimal volume in which the heat passing through is graphically illustrated with arrows which respectively enter and get out of it. During the quench process an important role is played also by the heat generated inside. The net amount of heat variations in the cube at a certain instant of time gives the infinitesimal variation of its internal energy. If the net heat passing through is positive the temperature increases while it is negative decreases. This can be expressed in the following this differential form:

$$\frac{du}{dt} = \sigma(\vec{r}, t) - \vec{\nabla} \cdot \vec{j}(\vec{r}), \tag{4.1}$$

which states that the local variation of energy is equal to the internal heat generation, σ, minus the divergence of the heat flux density. The divergence is a differential operator that estimates locally the net flux that is going out of an infinitesimal element. A good estimation of the heat flux density in a solid body is given by the Fourier's law,

$$\vec{j}(\vec{r}) = -k(T) \cdot \vec{\nabla} T, \tag{4.2}$$

which states that the heat flux is proportional to the temperature gradient via the heat conductivity which is a characteristic of the material. For a good thermal conductor like copper the heat conductivity is of the order of hundreds of W/(K·m) and it is strong temperature dependent. Without heat flow there would be no correlation between neighboring points of the solid. It is an essential ingredient for the quench phenomenon and without it there would be no expansion of the quenching zone. Each part of the wire would warm up just because there is an internal source of heat and not because of an exchange of energy with neighboring parts. The internal heat generation term causes a coupling of the thermal and the electrical properties. In the superconducting parts of wire this term is equal to zero while the normal conducting ones it can be expressed as:

$$\sigma(\vec{r}, J) = \rho(T) J^2(\vec{r}, t) \tag{4.3}$$

where ρ and J are the resistivity and the electrical current density. In the following ρ always represents the resistance averaged over the cross section of the wire, where the NbTi filaments and the copper matrix are electrically in parallel. The thermal energy density u in the (4.1) is defined in the following way:

$$u = \frac{\Delta U}{\Delta V}. \tag{4.4}$$

The energy density is connected with the temperature as follows

$$\frac{du}{dt} = \frac{du}{dT}\frac{dT}{dt} = c(T) \cdot \frac{dT}{dt} \tag{4.5}$$

where c is the characteristic of the material heat capacity. This parameter correlates at each temperature the infinitesimal energy variation with the infinitesimal temperature variation. Solving Eq.(4.1) means finding the function $T(\vec{r}, t)$ for given initial temperature distribution and specific boundary conditions.

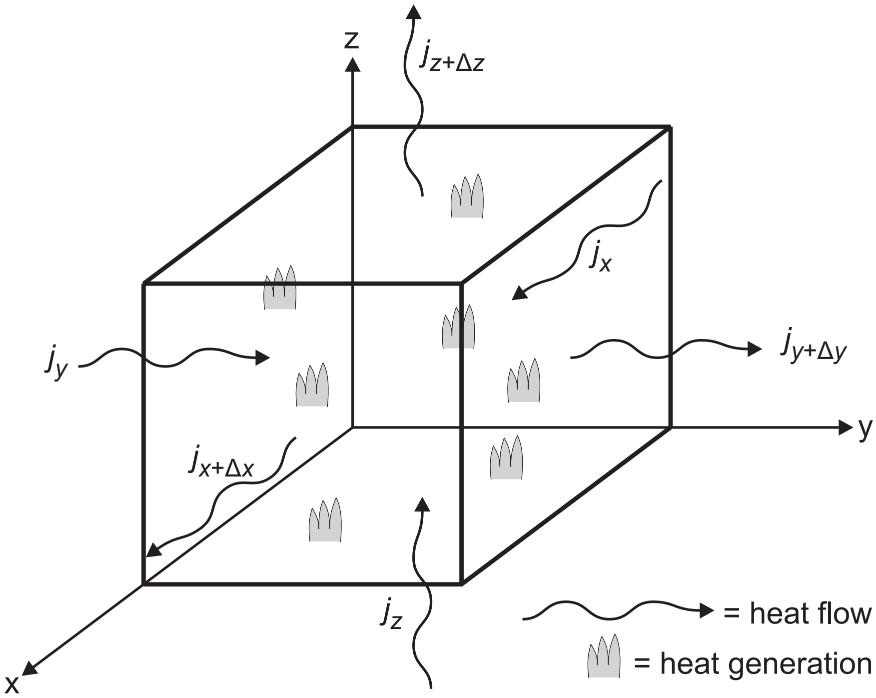

Figure 4.1: The components of the three-dimensional balance equation, Eq.(4.1)

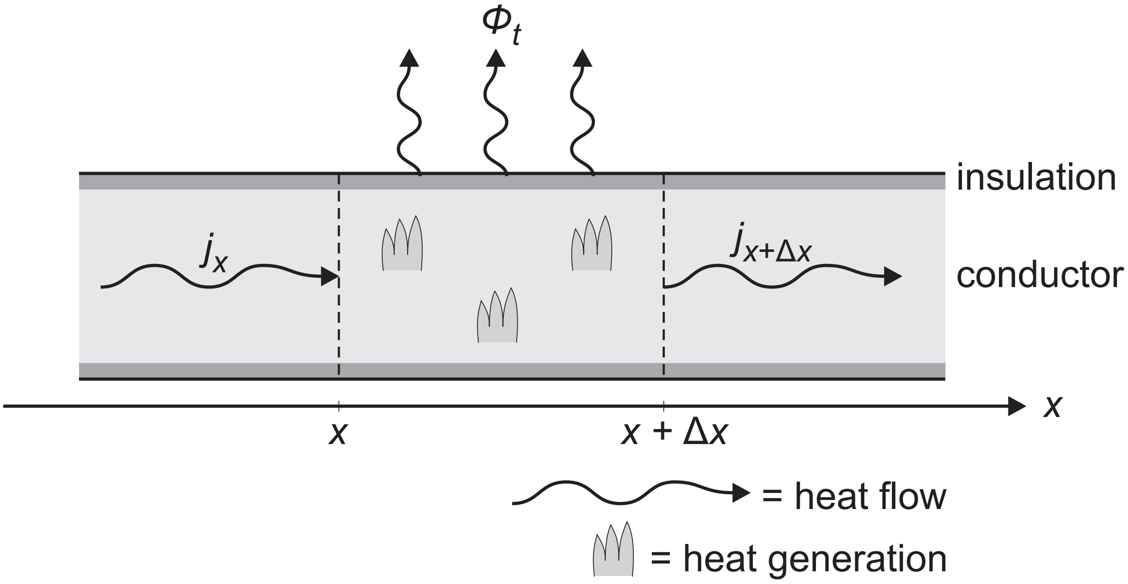

Figure 4.2: The contributions to the one-dimensional balance equation, Eq.(4.6)

4.2 One-dimensional heat balance equation

The elongated shape of a wire suggests that the quench propagation may be studied with a one-dimensional model. The whole system is divided into two subsystems: the conductor and the environment. A wire can be regarded as 'thin', when the temperature is the same (or very close to the average) for all points of a cross section. In this case the only space variable remaining is the length along the wire (in the following the z co-ordinate). Each cross section is just characterized with one temperature and one value for the material parameters. In Fig. 4.2 the evaluation of the net heat flux for this element is shown. There is heat generated in this element, heat flowing along the conductor, entering in a cross section and going out of it and also heat exchanged with the environment, through the side surface. The one dimensional heat balance equation takes the form:

$$A \cdot c(T) \cdot \frac{dT}{dt} = A\frac{dj_z}{dz} + \sigma(T, I) - \Phi_t, \tag{4.6}$$

where A is the cross section of the conductor, j_z the heat flux density along the conductor,

$$j_z = -k(T) \cdot \frac{dT}{dz}, \tag{4.7}$$

σ is the ohmic heat generation

$$\sigma = \frac{\rho(T)I^2}{A}, \tag{4.8}$$

with the current I:

$$I = \int_A \vec{J}(\vec{r}) \cdot d\vec{A}. \tag{4.9}$$

The term Φ_t in the (4.6) stands for the heat leaving the conductor transversally and it must be evaluated for the specific environment in which the wire is working. In general it is a complex function of the history of the conductor temperature, but a good approximation for the purpose of this thesis is a function of the conductor temperature and it's time derivative. The LHC wire are wrapped with two layers of polyimide tape serving as electrical insulation. They operate in a bath of superfluid helium at 1.9 K. In the literature this term is usually called *cooling* because the heat exchange limitations due to the electrical insulation are often not taken into account and Φ_t is only the evaluation of the heat that liquid helium can absorb at different temperatures. In the following *cooling* signifies the heat flow out of the (bare) copper wire into the insulation, which is surrounded by liquid helium.

4.3 Adiabatic calculation - the quench load

At first sight it appears that the assumption of no cooling (Φ_t=0) leads to the most conservative design and therefore the most safe operation of devices. However, this is only true if the time to detect a quench is negligible compared to the energy extraction time of the circuit, which is not the case for many circuit, like for example the busbars. However, adiabatic calculations are useful for a first, coarse estimate of the maximum temperature reached during a quench. The calculation is particularly simple if no heat flow along the wire is allowed, which is equivalent to assuming that the temperature is the same all along the wire. The following calculation is usually called the *quench load* or *MIITS* calculation. With these assumptions the heat balance equation becomes

$$\frac{\rho \cdot I^2}{A} = A \cdot C(T) \cdot \frac{dT}{dt}, \tag{4.10}$$

in which there is just the internal heat generation that in each instance of time has to be equal to the energy variation of the same region. If a quench starts in any part of the conductor at the time t_0, this means that its temperature is equal to the temperature of current sharing[1] one ($T(t_0)=T_{cs}$). The temperature evolution under the above condition can be evaluated with the integral:

$$\int_{t_0}^{t} I^2(t)dt = A^2 \cdot \int_{T_{cs}}^{T} \frac{C(T')}{\rho(T')} dT'. \tag{4.11}$$

The integral at the right side of this equation may be calculated for given material parameters and with this function the maximum temperature for a given *I(t)* can be easily calculated. In an engineering application of superconducting wires it is often necessary to assess if a chosen wire will survive the I(t) required after a quench (magnet de-energisation). Eq. (4.11) can be used to get a first estimate for T_{max} reached for a given I(t). This is daily used in the tests of the LHC superconducting magnets as a first check of the correct operation of the magnet and of its protection system.

4.4 Cryogenic stability

For the understanding of a real system, cooling into the helium bath has to be considered [18]. With a wire in an adiabatic condition a quench may be triggered at any current regime. It is rather intuitive that the helium is able to absorb from the quench region at least a part of heat loads, generated by small currents, letting the conductor return to the superconducting state. For a first investigation on this subject the heat flux along the wire may be neglected. This is a conservative assumption because, as already discussed, this term spreads the heat along the wire, taking heat from the region at high temperature and transferring it to the neighborhood at low temperature. The heat balance equation becomes

$$\sigma(T) - \Phi_t(T, \frac{dT}{dt}) = A \cdot C(T) \cdot \frac{dT}{dt}. \tag{4.12}$$

Comparing the curves of the cooling and the heating in terms of the temperature there are different possible situations. The regions of the wire that are in a range of temperatures in which the heating is stronger than the cooling will warm up and the other regions will cool down. If both these regions are present there are intersection points and they belong to two different families:

---

[1] In the literature of applied superconductivity the critical temperature at a give current and magnetic field is usually called the temperature of current sharing T_{cs}, while T_c is defined as the critical temperature at a certain external applied magnetic field and zero transport current.

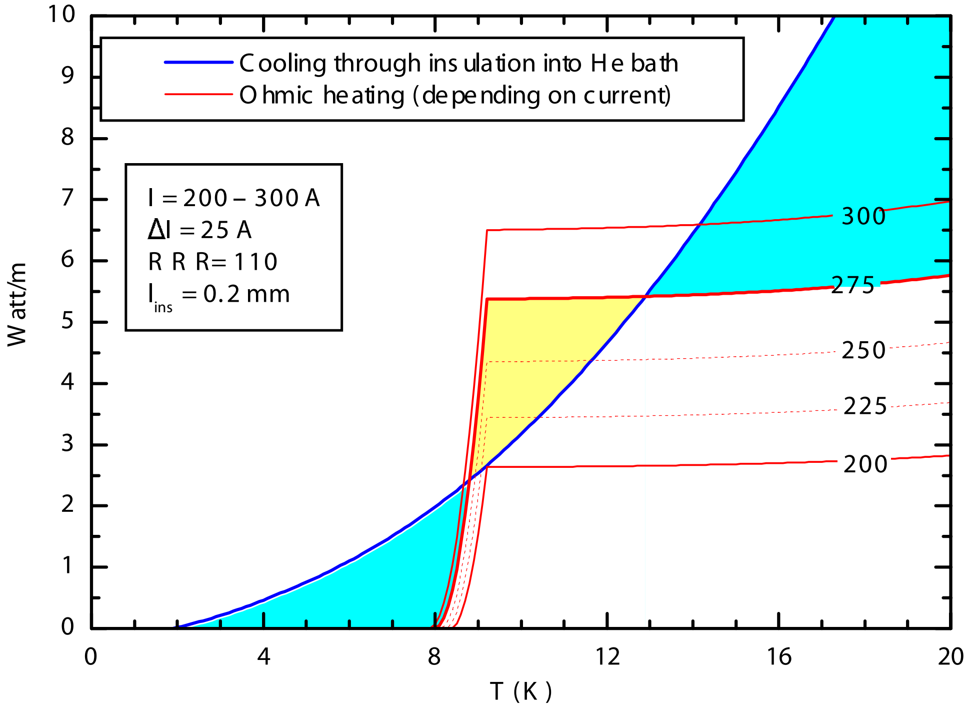

Figure 4.3: Equal area criterion applied to the wire of the 600 A busbars powering the LHC corrector magnets. The temperature dependence of the heat conductivity has been neglected.

- stable: T_i^{stable};
- unstable: $T_i^{unstable}$.

In the first group there are the intersections in which the cooling is weaker than the heating for T$<$T$_i^{stable}$ and the cooling is bigger than the heating for T$>$T$_i^{stable}$. These points are called stable because the regions that have a lower temperature warm up and the ones at higher temperature cool down until T$>$T^{stable} is reached. The unstable points are intersections with opposite order. The regions at higher temperature than T$_i^{unstable}$ will warm up and the region at lower temperature will cool down, such that the temperatures develop away from T$_i^{unstable}$. Between two stable points there is always an unstable one and vice versa.

If the cooling is stronger than the heating for every temperature up to the nominal current, then the cable is called *cryostable* and when a quench occurs it always disappears. The heat generation is a function of the current and for a real system there is always a current below which the system is cryostable. The limit current for cryostability , which is called I$_0$ in the following, is rather important and in the following section a criterion to calculate its value is presented.

4.5 Heat transfer and equal-area theorem

For given cooling and heating conditions a criterion to understand if a quench, with given initial conditions and current regime, starts expanding or retreating is presented in this section. In the treatment of cryogenic stability in the previous section the heat conduction was neglected but its effect can be very helpful, provided the zone is finite in extent and is enclosed by a cold superconducting region. At the boundary between hot and cold regions, heat conduction will add significantly to the cooling and may cause the normal zone to retreat. It will thus shrink and eventually disappear, even though the simple conditions for cryogenic stability are not fulfilled and the heating may exceed the cooling in the center of the zone.

In a current regime where stable temperatures exist, and thus sections of the wire may remain at these temperatures for a long time, the question arises what happens at a point where a quenched zone at T^{stable} and a superconducting one meet. As already mentioned, the normal zone can expand or retreat, depending on the current and thus the heating in the wire. Intuitively it is clear that at one particular current the border line does not move - it remains stationary. To find this current (or heating function), we therefore have to solve the equation:

$$\frac{d}{dz}\left(A \cdot k(T) \cdot \frac{dT}{dz}\right) = \Phi_t(T) - \sigma(T, I), \tag{4.13}$$

where no time dependant factors appear. The equation shows that only the difference between Φ_t and σ is significant. With the variable

$$S = k(T)\frac{dT}{dz}, \tag{4.14}$$

$$\frac{dS}{dz} = \frac{dS}{dT}\frac{dT}{dz} = \frac{dS}{dT}\frac{S}{k(T)} \tag{4.15}$$

z can be substituted from the (4.13) leading to:

$$A \cdot S\frac{dS}{dT} = k(T)(\Phi_t(T) - \sigma(T, I)), \tag{4.16}$$

which may be integrated directly between the temperature of the coolant,T_b, and the hot spot, temperature T_{max}:

$$\int SdS = \left(\frac{S^2}{2}\right)_{S(T_b)}^{S(T_{max})} = \int_{T_b}^{T_{max}} k(T)(\Phi_t(T) - \sigma(T, I))dT. \tag{4.17}$$

The cold part far from the interface is at homogeneous temperature T_{bath} where the gradient is zero and the hot spot is at a stationary temperature where dT/dz is also zero. Thus $S(T_{bath})=S(T_{max})=0$:

$$\int_{T_0}^{T_1} (\Phi_t(T) - \sigma(T, I))\, k(T)dT = 0 \tag{4.18}$$

or, if k does not depend on temperature,

$$\int_{T_0}^{T_1} (\Phi_t(T) - \sigma(T, I))\, dT = 0 \tag{4.19}$$

This is the mathematical criterion for a stationary front line between superconducting and quenched regions.

It is useful to visualize the cooling and heating functions. An example concerning the LHC 600 A busbars is shown in Fig. 4.3, [26][24]. The cooling curve does not change, but the heating curves are obviously current dependent. At currents above 200 A (the values were taken from a simulation of a busbar wire) the cooling and heating curves intersect at two temperatures, where the smaller one is unstable and the larger one stable. Assuming that the quenched region is at the stable temperature, the (4.19) states that for the stationary case the blue triangle at the right and the yellow triangle have to have the same area, which is the case for 275 A in the example shown. This is thus the current I_0 where the quench propagation velocity is zero. The condition expressed in the (4.19) is usually called the equal area theorem:

$$A_1(I_0) = A_2(I_0). \tag{4.20}$$

If k does depend on T the heat generation and cooling should be plotted multiplied by k(T) to enable a direct comparison of the two areas (see the Eq. (4.18)).

4.5.1 Minimum Quench Energy

The problem of the minimum quench energy (MQE) refers to the calculation of the transient response of an initially superconducting cable to an arbitrary energy input [18], abstracting from the origin and nature of the disturbance spectrum. The main result of the analysis is the stability margin, the maximum energy that can be deposited in the cable over a given extension in space and time and with a given waveform for which the transient response ends with the cable back to the superconducting state. This is a conceptually simple problem statement. However, depending on the level of detail and the type of application, it involves modelling of a transient, coupled, thermal, fluid-dynamics and electro-dynamics problem with, often, 3-D space dimension. The additional difficulties intrinsic to the knowledge of non-linear material properties and transport coefficients at cryogenic temperature can result in large margins of uncertainty and considerable computational complexity.

4.6 Quench Propagation Velocity

If a superconducting wire gets locally normal conducting because a sufficient amount of heat (>MQE) has been absorbed from an external source, the dissipating region starts expanding at constant velocity. Defining z_q as the border between the normal conducting zone and the resistive one, the velocity is defined as (see Fig. 4.4):

$$v_q = \frac{dz_q}{dt}. \tag{4.21}$$

References to the measuring techniques as well as calculations can be found in [18, 58, 56, 54].

4.7 Simulation Program for Quench Research (SPQR)

The physical model used in the SPQR code is the two wire approximation. The quench propagation velocity calculation are not very different with respect to the one already performed

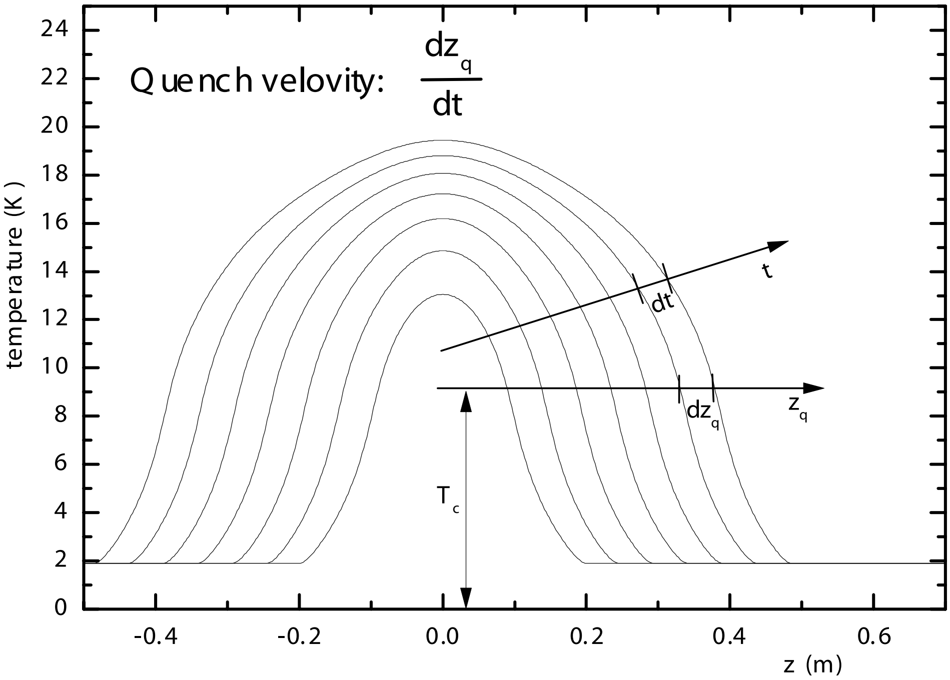

Figure 4.4: Schematic representation of the expansion of a normal conducting zone in a superconducting wire.

at an earlier stage [25] with the single wire approximation, but the two wire model gives the opportunity to understand the phenomena of current redistribution inside the cable. Even if it is a simple model it has already the ingredients to estimate the transversal current induced by the magneto resistivity [63, 64] induced by non negligible magnetic field gradient in the cable cross section, which is actually the case of the LHC superconducting, and to interpret the voltage signals which at the very beginning of a quench are strongly non linear because of a non negligible inductive component induced by current redistribution. The simulation performed helped the interpretation of the data recorded on the LQA, giving solid explanation of the complex signal wave form observed at the very beginning of the transition. In the following sections the equations used are described in detail. The relevant numerical methods are presented in the appendix B.

4.7.1 The Two Superconducting Wire Model

The two wire model has been used to model the quench propagation in the Rutherford cable for the LHC dipole magnets. In this case the magnetic field cross section in the conductors region is very inhomogeneous and this causes great difference the magneto resistivity in the cable cross section. The cable is subdivided in two wire, one which describes the half at high field region and the other the half at low field region, each of them is characterized with the temperature, the current and the average magnetic field. The thermal equations are the

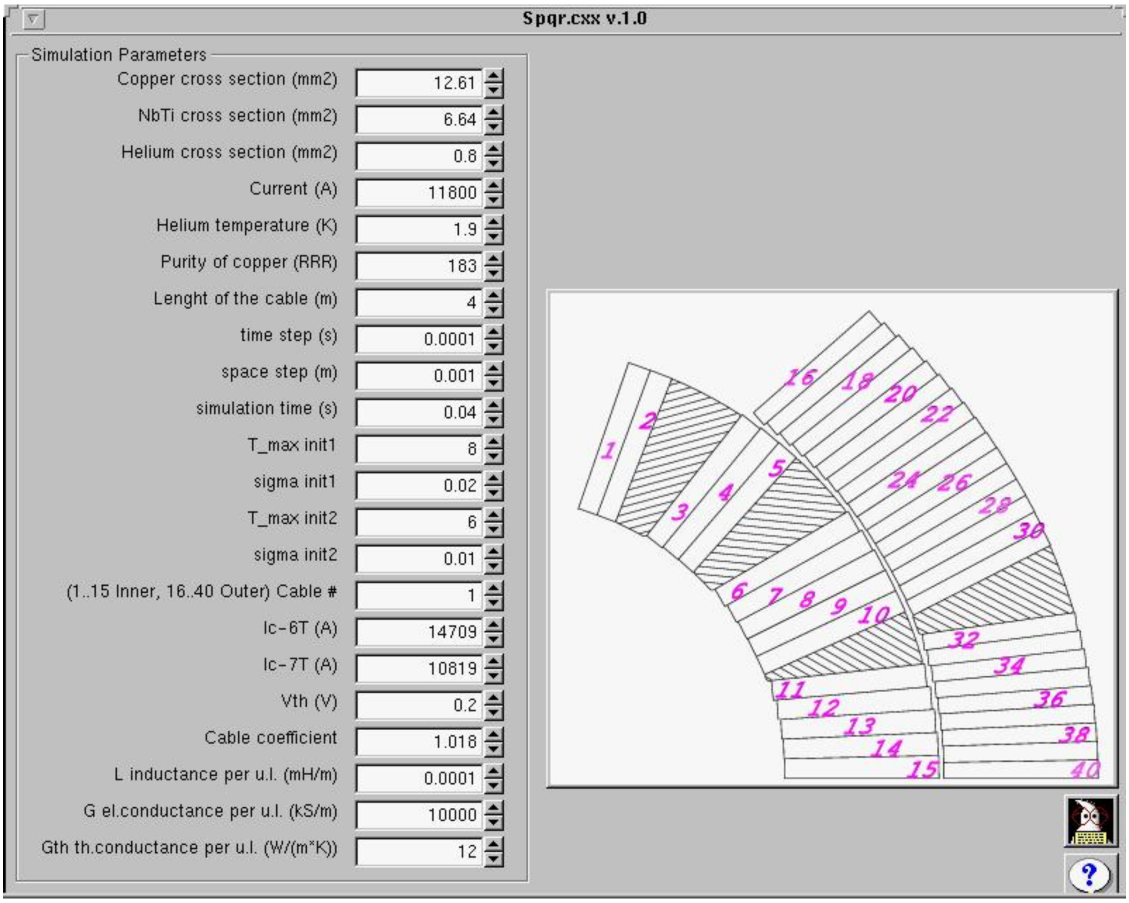

Spqr.cxx v.1.0

Simulation Parameters

Copper cross section (mm2) 12.61
NbTi cross section (mm2) 6.64
Helium cross section (mm2) 0.8
Current (A) 11800
Helium temperature (K) 1.9
Purity of copper (RRR) 183
Lenght of the cable (m) 4
time step (s) 0.0001
space step (m) 0.001
simulation time (s) 0.04
T_max init1 8
sigma init1 0.02
T_max init2 6
sigma init2 0.01
(1..15 Inner, 16..40 Outer) Cable # 1
Ic-6T (A) 14709
Ic-7T (A) 10819
Vth (V) 0.2
Cable coefficient 1.018
L inductance per u.l. (mH/m) 0.0001
G el.conductance per u.l. (kS/m) 10000
Gth th.conductance per u.l. (W/(m*K)) 12

Figure 4.5: The graphical user interphase developed for SPQR. All the parameter need for the simulation may be introduced directly in this panel. After running the simulation the results are automatically plotted.

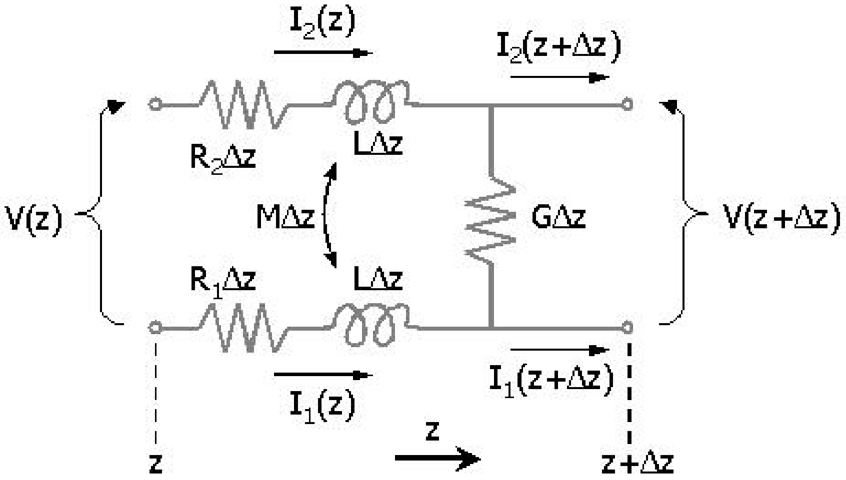

Figure 4.6: A schematic of an infinitesimal length Δz of the two wires.

following

$$A_1 \cdot c(T_1) \cdot \frac{dT_1}{dt} = A_1 \frac{d}{dz}\left(k(T_1)\frac{dT_1}{dz}\right) + \sigma_1 + \beta(T_1 - T_2), \tag{4.22}$$

$$A_2 \cdot c(T_2) \cdot \frac{dT_2}{dt} = A_2 \frac{d}{dz}\left(k(T_2)\frac{dT_2}{dz}\right) + \sigma_2 + \beta(T_2 - T_1), \tag{4.23}$$

where T_1 and T_2 are the average temperature in the high and in the low field region. The electrical behavior is well described in the circuit described of Fig. 4.6 where the current can flow from one side to the other of the cable throw distributed resistance. In the continuous limit ($\Delta z \rightarrow 0$) the equation is

$$L_{eq}\dot{I}_1 = \frac{1}{G}\frac{d^2 I_1}{dz^2} - (R_1 + R_2)I_1 + R_2 I_0, \tag{4.24}$$

where $I_1 + I_2 = I_0$ are respectively the current in the high field and the one at low field region and the total current in the cable. Similarly the $R_1 > R_2$ are the linear resistance of the high and of low field region and their expression is

$$R_1 = \frac{\rho(T_1, B_1)}{A_1}. \tag{4.25}$$

It is important to notice that G is now the transversal electrical conductance per unit length and it is related to the copper resistivity and to the contacts among the strands, a good estimation of such parameter is the given by the following formula

$$G = \gamma\rho(\langle T\rangle, \langle B\rangle)\frac{w_c}{2h_c}, \tag{4.26}$$

where $\langle T\rangle$ and $\langle B\rangle$ are the average temperate and magnetic field between the two wires, w_c and h_c are the width and the height of the cable and γ is a coefficient which take into account the contribution of the contact resistance among the strands. The heat generation has the following form

$$\sigma = R_1 I_1^2 + \frac{1}{2G}\left(\frac{dI}{dz}\right)^2. \tag{4.27}$$

To fully specify the problem the initial conditions and the boundary conditions have to be defined for both the thermal and electrical equations. As initial temperature profile, the gaussian distribution is used which describes reasonably an external spot like perturbation inducing the deviation from the uniform helium bath temperature (T_b). The initial condition must be imposed on both wires and the following parametrization is used:

$$T_1(z, t = 0) = T_1^{max} \exp\left(-\frac{z^2}{2\sigma_{z1}^2}\right) + T_b, \tag{4.28}$$

$$T_1(z, t = 0) = T_2^{max} \exp\left(-\frac{z^2}{2\sigma_{z2}^2}\right) + T_b. \tag{4.29}$$

Adiabatic conditions, like the following, have been adopted for the cable's boundaries

$$\frac{dT}{dz}(z = 0, l) = 0, \tag{4.30}$$

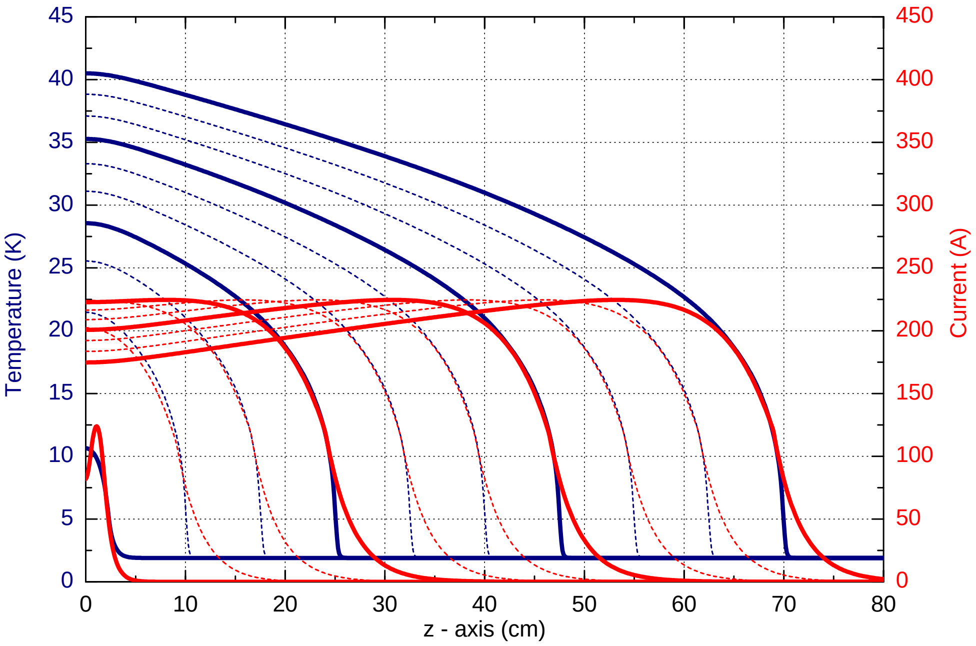

Figure 4.7: The simulation results of SPQR. On the right axis the temperature profile and on the left axis the current difference between the low field and high filed region of the cable. Different curves represent the profiles in different instant of time. The time interval between the solid curves is 20 ms

where l is the end of the cable length. The boundary conditions (4.30) are an important ingredient for the mathematical and the numerical solution of the equations but they do not play an active role in the evolution of the system: until the normal expanding zone does not approach the boundary region the system does not "feel" the influence their presence.

As starting conditions for the electrical equations a uniform current profile has been adopted,

$$I_1(z) = I_2(z) = I_0/2, \tag{4.31}$$

which are in agreement with the evidence that it is the thermal part which drives the system. In the boundaries the transversal voltage is considered equal to zero

$$\frac{dI}{dz}(z = 0, L) = 0. \tag{4.32}$$

4.7.2 LHC Rutherford Cable - Simulation Results

An example of simulation results of SPQR is presented in Fig. 4.7. The main results are the temperature profile as a function of time and the current redistribution between the two side of the wire. When locally the temperature is above the critical one it might happen that the heat generation is sufficient to drive the system into an irreversible resistive transition and, if this is the case, the normal conducting zone starts expanding with constant velocity and the current starts redistributing in the half of the wire where the resistivity in lower.

With the output provided by SPQR, the other properties of the quench can be easily estimated (they are normally provided directly by the program) like for instance the voltage across the quenching wire

$$v(t) = \int_0^L R_1(z,t)I_1(z) + (L-M)\dot{I}_1(z,t)dz \tag{4.33}$$

and the voltage induced on a pick-up coil, see section 5.6.

4.7.3 Analytical Approximation for the Current Redistribution

Beyond certain approximations it is possible to get an analytical expression of the current redistribution around the quench front [23]. The simulation results confirmed that after a short transitory regime, which depends on starting conditions, the quench begins to propagate at constat velocity. This allows to define the current distribution of the front as a travelling wave,

$$I(z,t) = I(z - v_q t). \tag{4.34}$$

Moreover, around the quench front the temperature is below 20 K, a regime in which the resistance of copper is in practice constat with respect to temperature. The electrical equation of the two wire model under these approximations becomes

$$\frac{1}{G}\frac{d^2}{dz^2} + L_{eq}v_q\frac{dI}{dz} - (R_1 + R_2)I + R_2 I_0 = 0. \tag{4.35}$$

In any instant the cable can be divided in two parts (see Fig. 4.8), the superconducting and the normal conducting one. Defining z_0 as the border between these regimes, the (4.35) must be solved separately for the two domains and afterwards the continuity of the current and of the transversal voltage must be assured. The solution is plotted in Fig. 4.9. In both regions the current gets into its stationary flat distribution with an exponential transition but with different characteristic length of redistribution. The value of the characteristic length in the normal conducting part is

$$\frac{1}{\lambda_n} = \frac{1}{2}\left(\sqrt{\frac{1}{\lambda_s^2} + 4G(R_1 + R_2)} - \frac{1}{\lambda_s}\right), \tag{4.36}$$

while in the superconducting is

$$\frac{1}{\lambda_s} = LGv_q. \tag{4.37}$$

Defining the total current which has to be redistributed as

$$\Delta I_0 = \frac{|R_2 - R_1|}{R_1 + R_2} I_0 = \Delta I_n + \Delta I_s, \tag{4.38}$$

the remaining current which has to be redistributed in the superconducting part is

$$\Delta I_s = \frac{\lambda_s}{\lambda_s + \lambda_n}\Delta I_0. \tag{4.39}$$

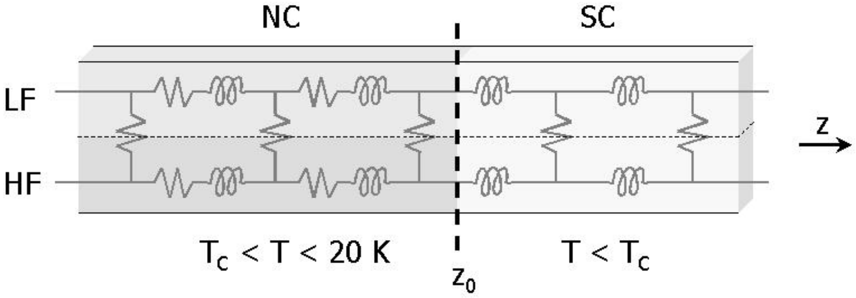

Figure 4.8: The model, with the normal-conducting (NC) zone on the left and the superconducting (SC) zone on the right. For this particular cable, the non-homogeneous magnetic field results in a high-field (HF) region below a low-field (LF) region. The quench front is located at the position z_0 along the z-axis, which runs parallel with the cables, and $z_0(t) = v_q t$.

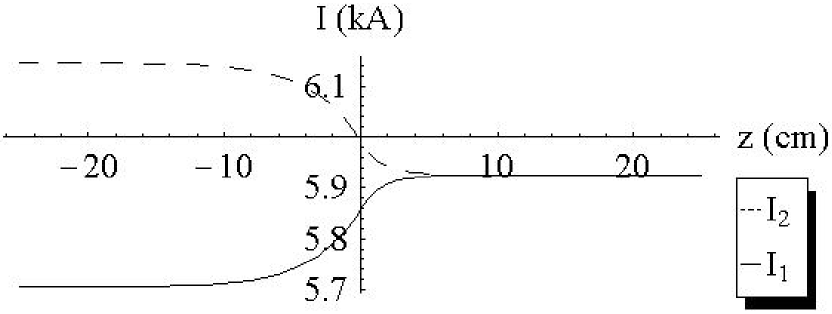

Figure 4.9: The current distribution induced by the quench calculated by means of the analytical approximation.

When v_q increases the redistribution length λ_s decreases while λ_n increases. At the limit of high speed the current redistributes mostly in the normal conducting part with a very long length of redistribution while the current in the superconducting one remains at the initial state. This is consistent with the simple evidence that it is the normal conducting side which drives the process while the superconducting one just follows: if the expansion of the normal zone is much faster than the diffusion time of the current, the superconducting part has no time to react and change its state. On the contrary, at the limit of very low speed there is no current redistribution in the normal conducting part while there is a long tail of redistribution in the superconducting one. If current has "time" it prefers to redistribute in the superconducting part rather than in the normal conducting one and to reduce the resistive path (which in this region is only the transversal one) increasing as much as possible the length of the redistribution.

The analytical formulas which estimate the quench propagation velocity present in the literature [54] do not take into account the transversal field gradient but it is never the less evident that there is a non negligible power dissipation during current redistribution. The only analytical work which has been found concerns the current redistribution effects in super-stabilized conductor [55, 56, 57, 58]. Moreover this process involves also the superconducting region where no power dissipation is expected.

The total amount of power dissipated because of the induced transversal current is easily estimated. The total power dissipated in the normal conducting part is

$$P_n = \frac{1}{G}\int_{-\infty}^{z_0}\left(\frac{dI}{dz}\right)^2 dz = \frac{\lambda_n \Delta I_0^2}{2G(\lambda_s+\lambda_n)^2}, \tag{4.40}$$

while total power dissipated in the superconducting part is

$$P_s = \frac{1}{G}\int_{z_0}^{+\infty}\left(\frac{dI}{dz}\right)^2 dz = \frac{\lambda_s \Delta I_0^2}{2G(\lambda_s+\lambda_n)^2}. \tag{4.41}$$

Defining

$$\lambda = \lambda_n + \lambda_s, \tag{4.42}$$

the total amount of power dissipated because of current redistribution becomes

$$P_{tot} = \frac{\Delta I_0^2}{2G\lambda}. \tag{4.43}$$

4.7.4 The Two Mixed Wire Model

A version of SPQR has been developed to study the quench propagation in mixed strand cables. There exist several designs of such type of cables, for instance there are cables in which some strands are superconducting and others are normal conducting. Another variant design exist in which all the strands are superconducting and are wound around a normal conducting core. This last design triggered this investigation because the very first results suggest that this type of cables can improve the efficiency of the magnet protection system.

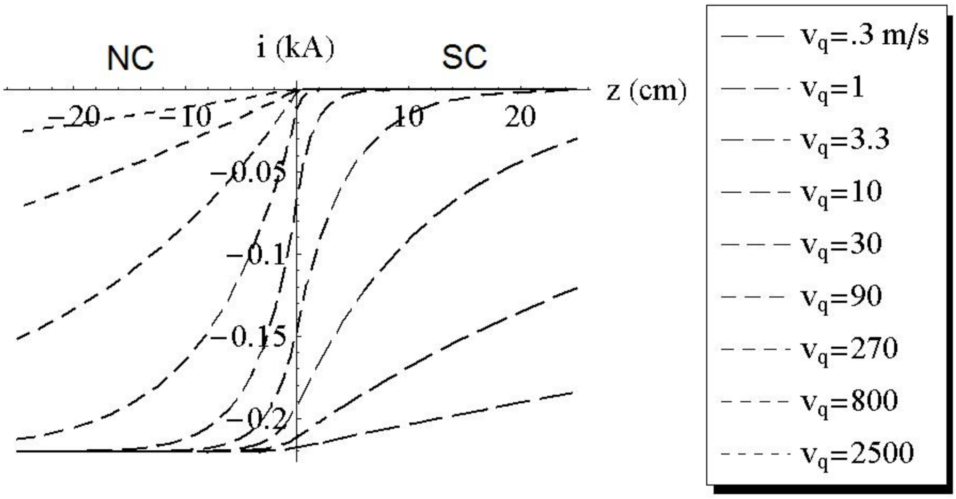

Figure 4.10: The profile of the total amount of current redistributed due to a non negligible transversal magnetic field is plotted. Different profiles are plotted for different velocity.

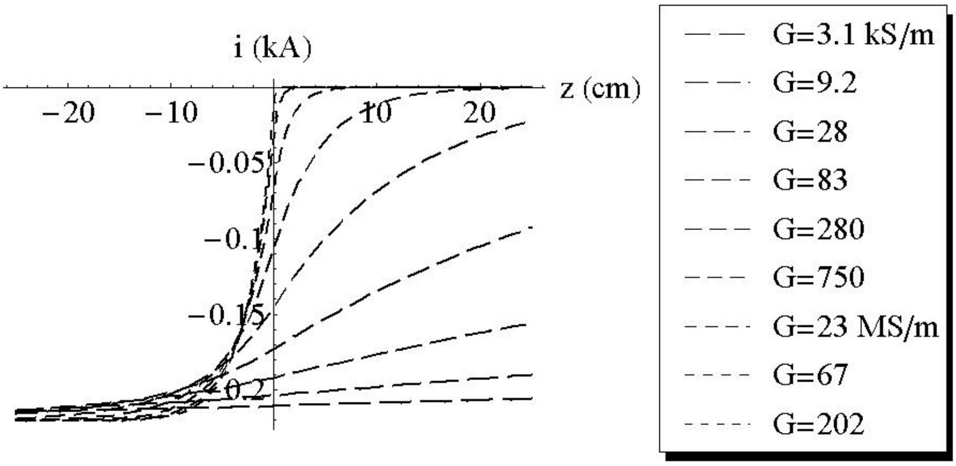

Figure 4.11: The profile of the total amount of current redistributed because of a non negligible transversal magnetic field is plotted. Different profiles are plotted for different value of the transversal conductance.

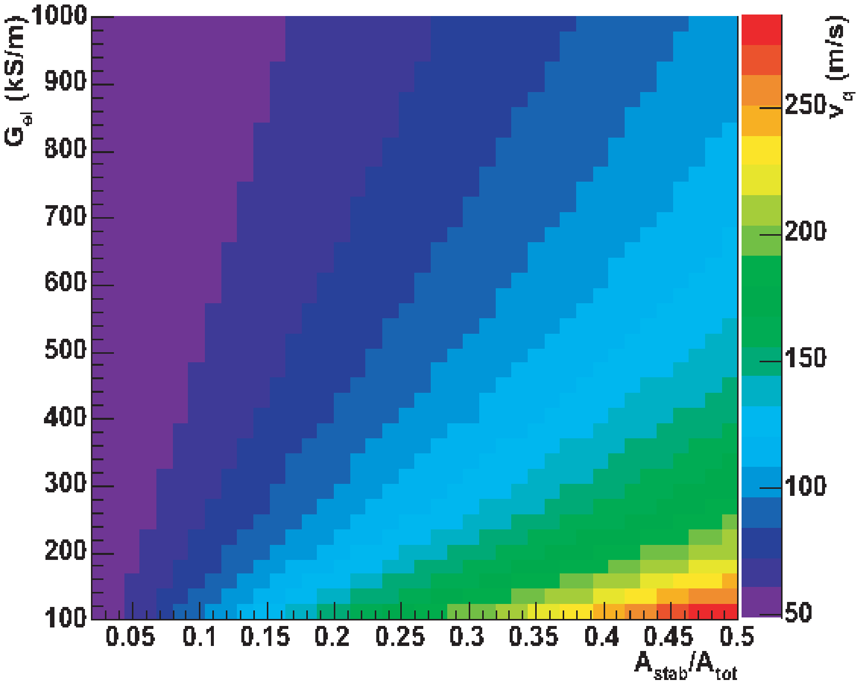

Figure 4.12: The sensitivity analysis study performed with SPQR of the quench propagation velocity in mixed cables with respect to the electrical conductance between the superconducting part and the stabilizer and the amount of stabilizer segregated as a separate component.

The numerical model adopted is essentially the same as the one discussed above, except certain changes in the interpretation of the parameters and the starting conditions of the electrical equations. Defining I_1 as the current in the superconducting component and I_2 as the current in the normal conducting components the starting conditions gets, $I_1 = I_{tot}$ and $I_2 = 0$, because, for such design, the current at the very beginning is confined only in the superconducting parts.

4.7.5 Mixed Cable - Simulation Results

A simulation campaign has been carried out to investigate the quench propagation velocity in mixed cables. The sensitivity analysis with respect to several parameters has been studied. Starting from the definition of the overall copper needed to protect the cable during a resistive transition, one important parameter was discovered to be the percent of the copper segregated as a separate component. In first approximation the amount of current redistribution is proportional to the percent of copper segregated outside the superconducting strands. Higher is the current moving in transversal direction and higher is the dissipation. Another key parameter is the resistance between the superconducting part and the normal conducting one. Higher is the resistance, higher is the length of the redistribution around the quench front and higher is the dissipation. The results of the simulated quench propagation velocity as a function of the two discussed parameters are summarized is Fig. 4.12.

4.7.6 Current Redistribution in the Quench Front

It is useful to compare the current redistribution in the quench front for superconducting cable and mixed cable. The calculation for the mixed cable has no significant difference with respect to the previous one, the characteristic length of redistributions for the normal conducting part is the same and for the superconducting part, which here is called mixed, is rather different

$$\frac{1}{\lambda_m} = \frac{1}{2}\left(\frac{1}{\lambda_s} + \sqrt{\frac{1}{\lambda_s^2} + 4GR_2}\right), \tag{4.44}$$

$$\Delta I_0 = \frac{R_2}{R_1 + R_2} I_0 = \Delta I_n + \Delta I_s, \tag{4.45}$$

and the total current dissipated in the mixed one is:

$$P_m = \int_{z_0}^{+\infty} \left[\frac{1}{G}\left(\frac{dI}{dz}\right)^2 + R_2 I_2^2\right] dz = \frac{\lambda_m \Delta I_0^2}{2G(\lambda_m + \lambda_n)^2}\left(1 + R_2 G \lambda_m^2\right) \tag{4.46}$$

$$P_{tot} = \frac{\Delta I_0^2}{2G\lambda} + \frac{R_2 \lambda_m^3 \Delta I_0^2}{2\lambda^2}. \tag{4.47}$$

4.8 A general adiabatic model for a multi-strands cable

A superconducting cable for accelerator magnets is composed with several strands to have the mechanical flexibility required during winding of a magnet coil (see section 2.2). To correctly take into account this feature the one-dimensional model previously discussed must be used to describe not only a single strand but also a thermal and electrical coupling with the other strand which constitute the cable. The generalization of the thermal equation into a coupled system of thermal equation and the definition of a generical electrical network with distributed parameters is done in the following subsections.

4.8.1 Thermal Equations

A cable composed of N superconducting strands thermally coupled may be described as a system of one-dimensional heat balance equations with a coupling term. At first order approximation a linear term may be used to describe the coupling among the strands. The system of equations is easily described using the generalized scalar field $T_i(z,t)$ which indicate the temperature profile in the i-strand. Finally the system reads

$$A_i c(T_i)\dot{T}_i = A_i \frac{d}{dz}\left(k(T_i)\frac{dT_i}{dz}\right) + \sigma_i(T_i, I_1, I_2, ..., I_N) - \beta_{ij}(T_i - T_j), \tag{4.48}$$

in which the matrix σ_{ij} estimate the amount of heat which may flow from a strand to the others. The term σ is modified and the new term of dissipation term related to the mechanisms of current sharing among the strands are added. It is explained in details in the following sections.

4.8.2 Electrical Equations

The electrical properties of a single wire may be well described as a distributed inductance plus a distributed resistance. The resistance is related to the dissipation and the inductance to the energy which is store in form of current and magnetic field, mainly it states that current is a continuous function of time and space. Because all the strands which constitute the cable are in contact one with the others the current may flow from one to another through contacts resistances. The mathematical equation may be written using the formalism of the distributed circuits. Defining the V_i as the voltage difference between the wire i and a reference point and I_i as the current flowing in the wire i, the equation at the loop i reads like

$$-\frac{dV_i}{dz} = R_i(z)I + \sum_j L_{ij}\dot{I}, \tag{4.49}$$

where R_i is the resistance per unit length of the i-strand and L_{ij} are the self (i=j) and mutual inductance (L_{ij}=L_{ji}) between stands i and j. The strands are one close to the others and that means a strong magnetic coupling. This link is less strong further the strands are one from the others. The second equation is the current balance in the node of i-strand

$$-\frac{dI_i}{dz} = \sum_j g_{ij}(V_j - V_i) = \sum_j g_{ij}V_j - V_i\sum_j g_{ij}, \tag{4.50}$$

where the g_{ij} are the conductances per unit length between strand i and strand j ($g_{ii} = 0$ and g_{ij}=g_{ji}). The current in the cable has the value which is imposed by the power supply and this can be summarized as

$$I_{tot} = \sum_{i=1}^{N} I_i(z). \tag{4.51}$$

All this equation has a natural vectorial formulation if the correct matrixes are chosen. The Eq. 4.49 becomes

$$-\frac{d\mathbf{V}}{dz} = \mathbf{RI} + \mathbf{L}\dot{\mathbf{I}}, \tag{4.52}$$

where $\mathbf{R}$ is the matrix of linear resistances, it is diagonal and $R_{ii} = R_i$; $\mathbf{L}$ is the inductance matrix and it correspond to L_{ij}. The Eq. 4.50 becomes

$$-\frac{d\mathbf{I}}{dz} = \mathbf{GV}, \tag{4.53}$$

where **G** is defined like following

$$\mathbf{G} = \begin{bmatrix} -\sum\limits_{\substack{k=2\\k\neq 1}}^{N} g_{1,k} & g_{1,2} & \cdots & g_{1,N} \\ g_{2,1} & -\sum\limits_{\substack{k=1\\k\neq 2}}^{N} g_{2,k} & \cdots & g_{2,N} \\ \vdots & & & \\ g_{N,1} & g_{N,2} & \cdots & -\sum\limits_{\substack{k=1\\k\neq N}}^{N} g_{N,k} \end{bmatrix}. \tag{4.54}$$

This is a much more compact an simpler form and the final equation of the currents is

$$\mathbf{GL\dot{I}} = \frac{d^2\mathbf{I}}{dz^2} - \mathbf{GRI}. \tag{4.55}$$

4.8.3 Link between thermal and electrical parts

Considering only the simpler but effective case for our purposes in which I_{tot} is constant in time and all previous transitory are already well extinguished the dynamic of the system is driven at the beginning by the thermal equations. This statement means that is the local inhomogeneity in the temperature profile which gives the begin to the dynamic. It is nevertheless evident that the electrical equation has internal time constant and this imply that for a given temperate profile there is no a unique solution for the current but it is needed to know the initial state. This is a consequence of the not negligible electromagnetic energy store in the cable.

Considering the case in which locally a strand is above the critical temperature. Immediately there is heat produce by joule effect and the current locally starts to diffuse to the other strands. It is important to notice that the current diffusion among the strands is also a source of heat because of the contact resistances and the therm σ should be modified is the following way

$$\sigma_i = R_i \cdot I_i^2 + \frac{1}{2}\sum_j g_{ij} \cdot V_{ij}^2 = R_i \cdot I_i + \frac{1}{2}\sum_{j\neq i} \frac{1}{g_{ij}} \left(\frac{dI_i}{dz}\right)^2. \tag{4.56}$$

Chapter 5

The Local Quench Antenna

A new antenna for quench research on the series production of the LHC dipole magnet is presented. The system has been designed to localize within centimeters precision the starting region of a quench for better understanding of its origin. The measurements performed demonstrated also that the quench propagation velocity can be estimated with good precision. The design of the antenna and the standard operating configuration are illustrated in details and the procedure used for the analysis of measurement data recorded on several problematic magnets is discussed. Future developments to adapt the instrumentation to be used as a standard tool for the series tests on the LHC dipole magnets are discussed.

5.1 Motivations

The cold tests performed on the pre-series LHC dipoles confirmed that the coil extremities are the weak regions where most of the quenches begin. The measurements performed up to now by means of voltage tap technique and the standard low resolution quench antenna [9] give information about the pole of the dipole which is quenching and about the longitudinal location within a precision of about half a meter. A careful analysis of the voltage tap signals indicates which pole layer (inner or outer) is quenching [65]. The efforts paid to identify the quenching block of cables did not give unique solutions and moreover it was not possible to measure the quench propagation velocity but in few rare cases.

These limitations called for an improvement of the localization resolution to identify the weak elements of the magnet ends. To optimize the resources and to profit from the existing acquisition system the local quench antenna (LQA) has been designed to cover only the problematic regions of the magnet. This configuration has the disadvantage that in the rare case in which the quench does not start in the magnet extremities there is no information about its location except that the quench started not far from the antenna region.

5.1.1 Measurement Principles

The principles of this measurement technique are explained in details in [10, 11, 12]. While a superconducting cable is quenching the current carried in the filaments is shared with the normal conducting stabilizer. In the case of the LHC Rutherford cable it is a copper stabilizer. Because the magnetic field in the cable cross-section is not homogenous and the resistivity of copper increases with the applied magnetic field (magneto resistance [63]) the current redistributes to minimize the dissipated power. This phenomenon is at the origin of a transversal current, which generates a temporary local magnetic field distortion. This field distortion induces a voltage across a pick-up coil. Using several pick-up coils next to each other enables to visualize the propagation of the quench fronts.

Figure 5.1: The final assembly of the Local Quench Antenna is shown. The pick-up coils are finally covered with a semi-transparent plastic tube to prevent damages during manipulation.

5.2 LQA Design

The LQA has been designed to cover the last half meter of the LHC dipole coil (see Fig. 5.1). This configuration guarantees to detect quenches which start in the bending region of the coil up to the end of the layer jump region for the connection side. The measuring system is working at room temperature inside an anti-cryostat [8] but it is possible to adapt it for operating in cold conditions too.

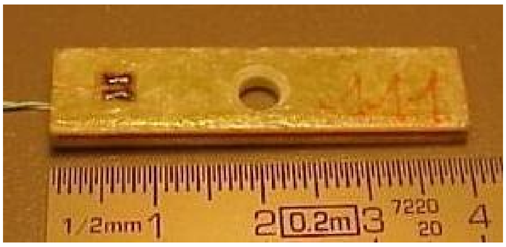

Figure 5.2: A pick-up coil used for the assembly of the LQA. A very thin tungstenic wire of 32 μm diameter is wound 400 times on a glass fiber support. The average magnetic surface measured over the all production is of about 0.1642 m^2

The pick-up coils assembled in the LQA are wound on a glass-reinforced epoxy which is 4 cm long, 1 cm wide and 1 mm thick, Fig. 5.2. From each pick-up coil the signal is carried out via a twisted wire pair soldered on the upper face of the coil, inside of a small connector. The shaft (Fig. 5.3) on which the pick-up coils are assembled is composed of eleven longitudinal sections. Each of them holds four pick-up coils in tangential configuration. Four grooves, aside each longitudinal array of pick-up coils, are used to place the twisted wires. At the end of each groove the wires enter in a hole and arrive at two rectangular connectors fixed in a titanium support, Fig. 5.4. This unit has in its extremity a mechanical connection to join with extension modules about 1.5 m long equipped with two multifilament cables that are plugged on the antenna connectors to carry the signals to the acquisition system. Thanks to the modular system adopted, the antenna can be placed all along the magnet by a single person. A mechanical support has been designed to help the installation and to give a precise longitudinal and azimuthal position to the antennas.

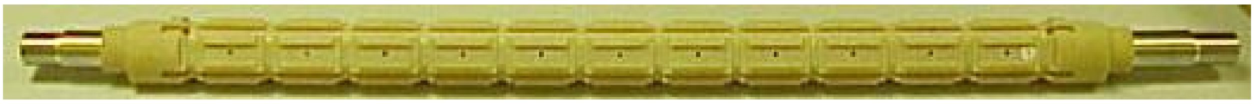

Figure 5.3: The shaft on which the pick-up coils are assembled. There are eleven sections and each of them is equipped to hold four coils in a tangential configuration.

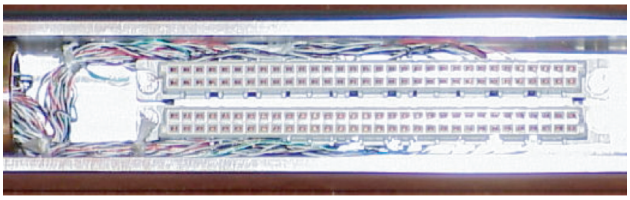

Figure 5.4: The two female connectors where the twisted wires of the pick-up coils are connected to. The wires come from the hole in the left side and are soldered to the bottom pins of the rectangular connectors.

5.2.1 Experimental set-up

The standard operating configuration foresees that four antennas are installed, one in each magnet extremity. The longitudinal position of two LQAs with respect to the LHC dipole magnet coil longitudinal section is illustrated in Fig. 5.6. The winding structure in the extremities is more complex than in the straight part of the magnet. The 2^{nd} block split in two in the non connection side and in three sub-blocks in the connection side. In the following the sub-parts of the second block are called a,b,c, starting from the outside (Fig. 5.6).

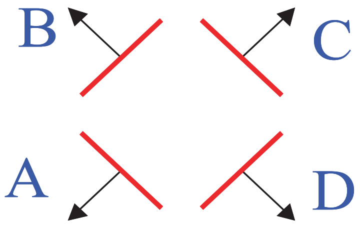

Figure 5.5: The LQA schematic cross section

Each antenna is fixed with the coils at 45^o degree with respect to the gravity. The pick-up coil signal is affected by the main field variation. To eliminate this signal component the difference between two pick-up coils with the same polarization with respect to the main field is taken before entering the acquisition system. This is also a fair method to reduce the number of signals. If the pairs of pick-up coils used for the compensation are far enough one from the other, the signal induced by the quench has always an amplitude very different on both. The compensation schema adopted is the following

$$\begin{cases} V_{AC} = V_A + V_C, \\ V_{BD} = V_B + V_D, \end{cases} \tag{5.1}$$

where V_A,V_C,V_B,V_D are the read out voltage of the coils with their own polarization. The convention chosen for the polarization is the one which preserves the rotation invariance of the coils with the positive versor going out of the shaft, Fig. 5.5.

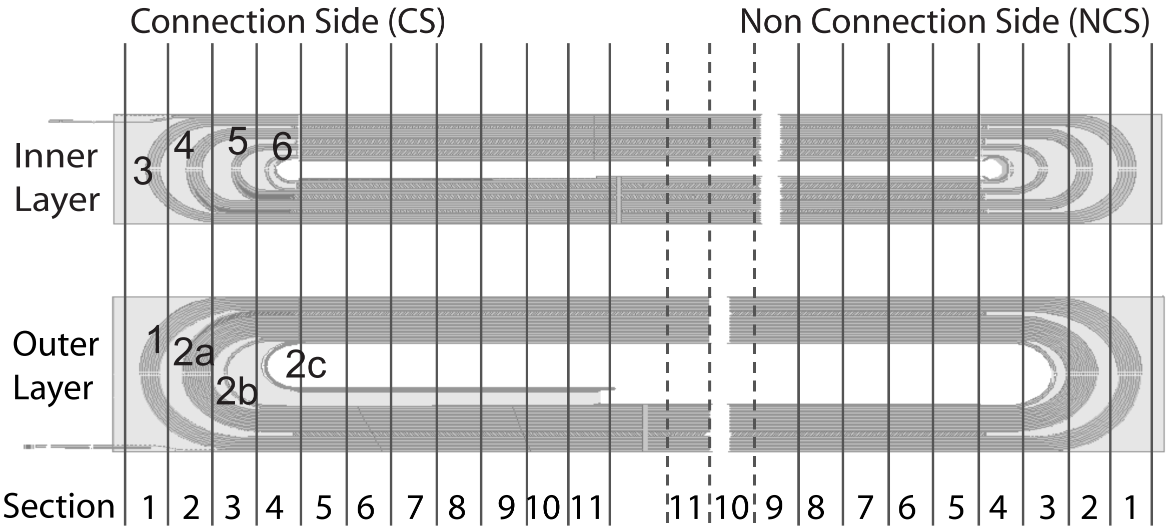

Figure 5.6: The standard longitudinal position of the LQA with respect to the LHC dipole superconducting coils. The sections 1, 2, 3 and 4 are dedicated to the monitoring of the bending region of the magnet. The label on each cable blocks is used as a reference to identify the quenching region.

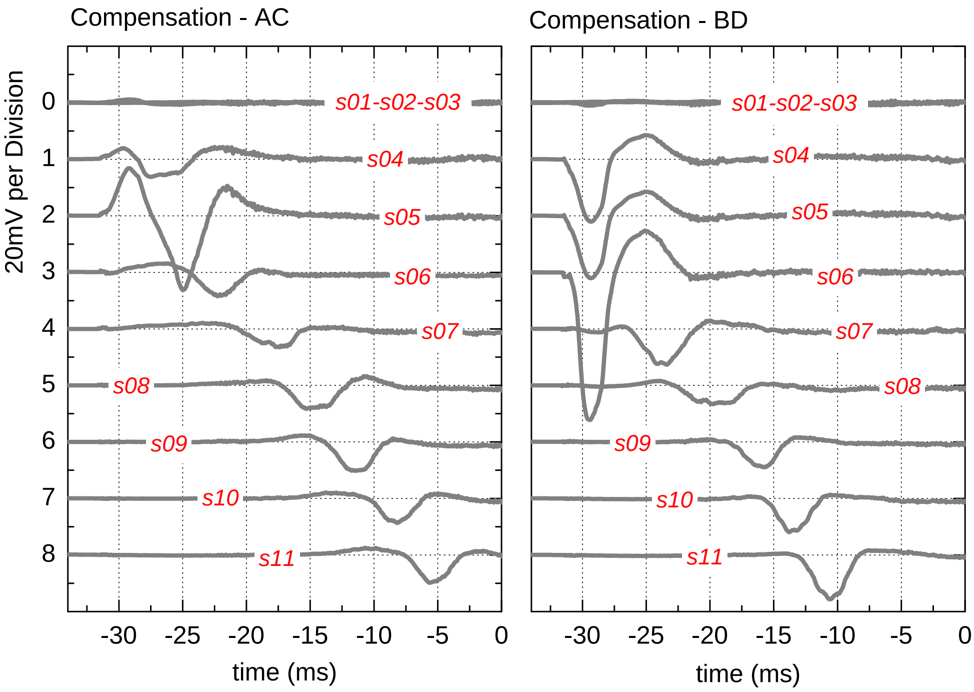

Figure 5.7: The signals recorded on the antenna located in the quenching extremity. Different sections are spaced in amplitude of 20 mV to easy inspection. The sections 1, 2 and 3 are not activated and they are plotted on the same raw. The signals are filtered to reject the high frequency noise.

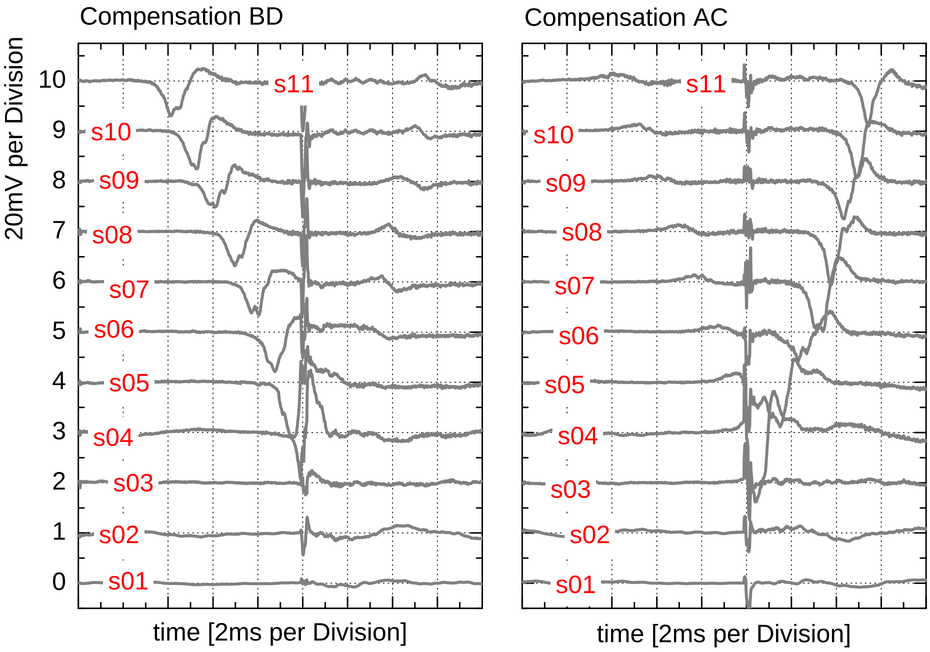

Figure 5.8: The second example of signals recorded on the antenna located in the quenching extremity. In this particular case the quench started in the magnet straight part but close to the extremity and the propagation of a single front is visible. Different sections are spaced in amplitude of 20 mV to easy inspection. The signals are filtered to reject the high frequency noise.

5.3 Raw Data Examples

An example of raw data acquisition is presented in Fig. 5.7. Before the beginning of the quench the signal across the pick-up coils is at zero average, which indicates that the compensation technique efficiently eliminates the induced voltage due to the current ramping (10 A/s). When the quench starts the sections s04,s05,s06 are activated at the same time, the signals is present on both AC and BD compensation (with opposite sign) but it is higher on the BD one. The highest signal is on s06-BD. After a transitory regime of about 5 ms in which the signal oscillate, the coil s07-BD is activated and it displays a major single bump shape. With an almost constant delay the signals are activated also in s08-09-10-11 which is the signature of normal front propagating. On the AC compensation the same phenomenon is visible but each signal is delayed of about 5 ms with respect to the same section in the BD compensation. The AC signals show the propagation of the second front. It is never the less evident that the two fonts signals are not fully decoupled. Taking for instance the signal s11-BD, it has a negative minimum at -10 ms which corresponds to a positive maximum 8 times attenuated in the s11-AC.

In Fig. 5.8 a second example of data recorded with the LQA is presented. This quench starts in the straight part of the magnet and at the very beginning of the transition there is no signal on the LQA but after few milliseconds the quench propagates towards the extremity and activates the pick-up in section 11. This is the only example of such a quench that has been observed during the test campaign and it is very instructive because, thanks to the very particular location, the antenna is excited only by one quench front. The two compensations are very much differently affected by the quench propagation and this confirmed the sensitivity to left and right side of the magnet. After reaching section 4 the quench goes back to section 5. During the coming back the highest signal is in the opposite compensation.

5.4 Quench Localization

Localizing the starting region of the quench is very important to understand the performance of a superconducting magnet. The first pick-up coil activated in the antenna gives the longitudinal location of the transition region. If more than one coil is activated at the same time the whole region covered by the activated coils is considered quenching. If the readout signal of one coil is significantly higher than the others, the hot spot region of the starting quench is considered to be closer to that coil. If two coils are activated at the same time with about the same intensity the quench hot spot is considered located in the middle. The magnet cross section is divided in blocks and this structure is also preserved in the extremities. This geometry helps to identify the quenching block because each of them bends at different longitudinal position and each of them is spaced of about one pick-up coil length, like it is shown in Fig. 5.6. Wherever the quench starts in the extremity it propagates and reaches the bending part. The last coil activated during the propagation towards the very extremity gives the information about the quenching block. For instance in the raw data of Fig. 5.7 and 5.8 the last activated pick-up coils are in s04 which, knowing that the quench was in the inner layer pole let conclude that the quenching block was the 6^{th}.

5.4.1 Inner and Outer Layer Criterion

In many cases it is mandatory to know which layer of cables is quenching to conclude with the LQA data which block is quenching. A criterion based on the voltage taps signals has been developed [65]. It uses the *trt* (time to reach the threshold) parameter to discriminate between the inner and outer layer. The distinction is based on the difference in quench propagation velocity and linear resistance in the conductors of both layers. The criterion has been validated with measurements performed on prototype magnets in which the information about the quenching layer were available[1], see Fig. 5.9.

5.5 Measuring the Quench Propagation Velocity

The quench propagation velocity is one of the most important parameters for quench protection studies because it gives the major contribution to the voltage development across the magnet. Unfortunately it is not easy to estimate with good precision the quench propagation

---

[1] During the prototyping phase additional voltage tabs where assembled within the magnet coils by means was possible to identify the quenching layer of the magnet. When the R&D period finished it was decided to reduce the number of voltage tabs to the minimum needed for the protection system.

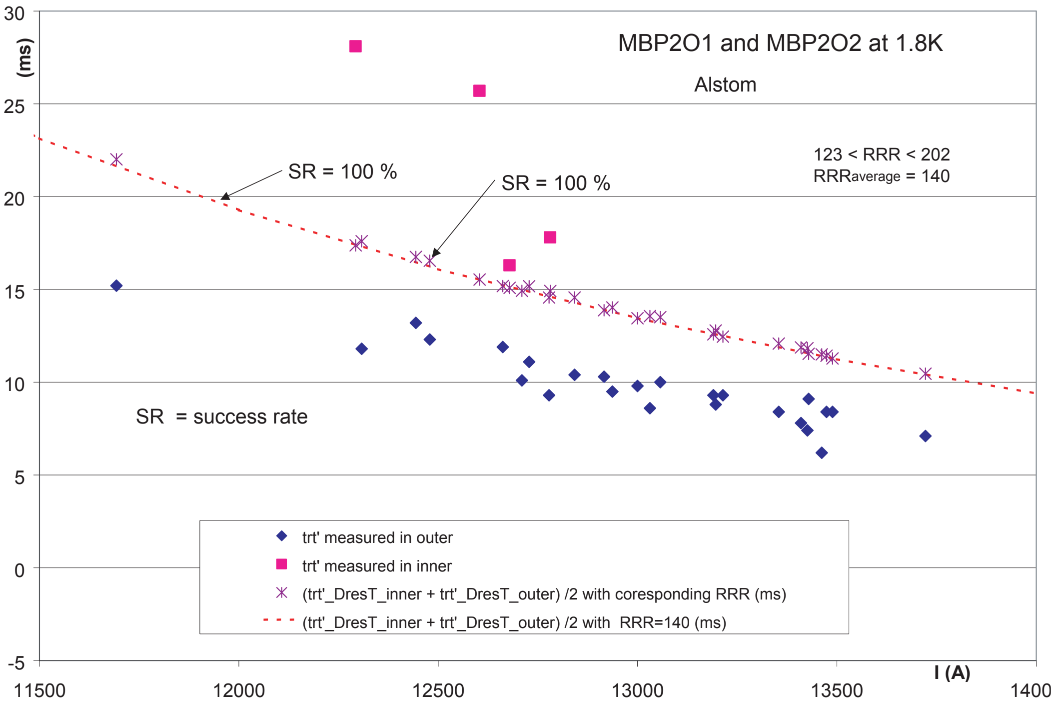

Figure 5.9: Application of the trt criteria to two prototype dipoles (courtesy Eric Floch)

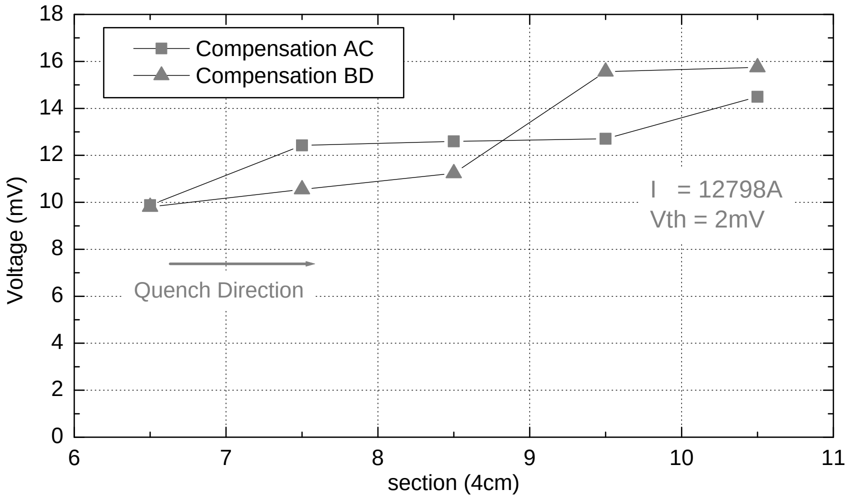

Figure 5.10: Example of the measurements of the quench propagation velocity as a function of the active section. The arrow indicates the direction of the quench propagation.

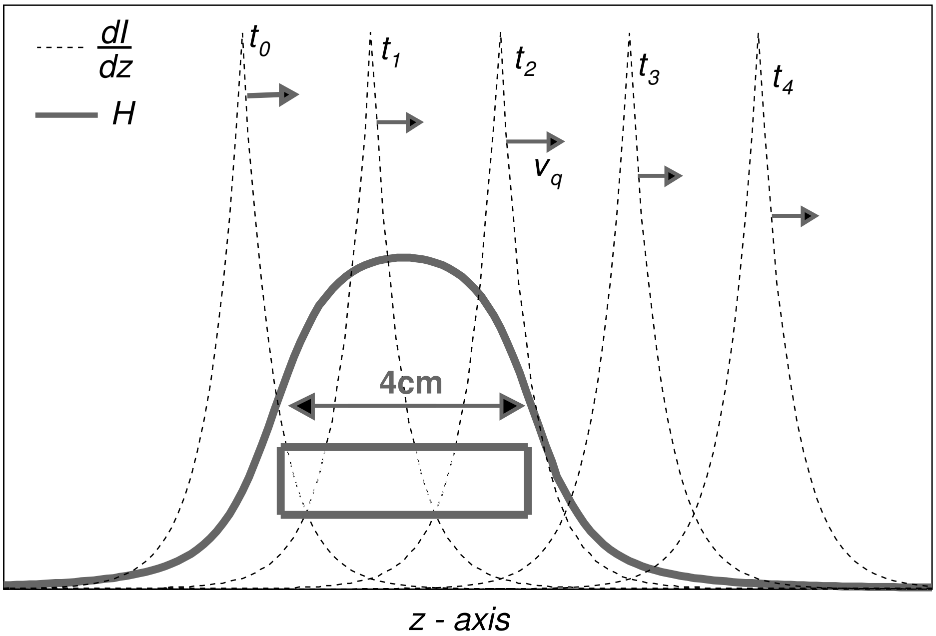

Figure 5.11: The schematic view of the coupling mechanism between the quench front and a pick-up coil. The current distribution moves with the quench front at constant velocity v_q while the pick-up coil is fixed. The voltage across the pick-up coil is proportional to the value of the space integral between dI/dz and H.

velocity of a cable even with sophisticated numerical simulation. On the contrary the quench antenna turns out to be a fair and simple instrument to measure it. The easiest criterion to extract the information about velocity is to define a threshold above which the quench is considered to be at the beginning of a coil. The time taken to observe the signal in the next coil at the same voltage level is considered equivalent to the time the quench takes to go from a coil to the next (δt). Knowing the distance between the beginning of two pick-up coils (l) the velocity is simply $v_q = l/\delta t$. Because the antenna is equipped with many sections of pick-up coils the velocity can be measured as a function of time or space, Fig. 5.10. During 5 to 10 ms after the quench start, it is difficult to measure the quench propagation velocity because the front is not yet established. This transition period is related to the conditions in which the quench is initiated. In some cases the transition period gives higher velocity than the stationary state. In other cases transition velocities are lower. The signal associated to the stationary quench propagation velocity does not depend on the starting conditions, which change from quench to quench and it has a simpler interpretation.

5.6 The Quench Propagation Signals

After few milliseconds from the beginning of the quench the signals recorded in the pick-up coils become very similar one to the other. This is the experimental evidence that the quench propagation front, responsible of the current redistribution, becomes translational invariance. In the following the two wires model is adopted to discussed the details of the calculation but the formulas can be easily extended for the general case. The value of the voltage across the pick-up coil, as a function of the current redistribution, can be formulated as (see also Appendix A and Fig. 5.11)

$$v(t) = \frac{d}{dt}\int_{-\infty}^{+\infty} I_1(z,t)h_1(z) + I_2(z,t)h_2(z)dz \tag{5.2}$$

where I_1 and I_2 are respectively the current distribution along the wires located the high field region and in the low field region, h_1 and h_2 are the transfer functions of the pick-up coil, they are different because the two wires are located in different positions. If the quench front is translation invariant at the velocity of the quench (v_q) than the 5.2 becomes simpler

$$v(t) = -v_q\int_{-\infty}^{+\infty} \frac{dI}{dz}(z - v_q t)h(z)dz, \tag{5.3}$$

where

$$h(z) = h_1(z) - h_2(z) \tag{5.4}$$

which is, apart from some cosmetic differences, a convolution.

5.6.1 The transfer function of the pick-up coil

In the evaluation of the pick-up coil transfer function two approximation have been used, the point like antenna and the segment like antenna. The first and the simplest one has this expression

$$h_p(z) = \frac{\mu_0}{4\pi}(\hat{t}\cdot\hat{n}_A)\frac{Sd}{(z^2+d^2)^{-3/2}}, \tag{5.5}$$

$$\hat{t} = \frac{\hat{z}\times\hat{r}}{|\hat{z}\times\hat{r}|}, \tag{5.6}$$

where S is the magnetic surface, which is in principle equal to the product of the number of turns (N_t), the length (L) and the width (w) of the pick-up coil but all pick-up coils assembled has been tested and the magnetic surface measured. d is the distance between the center of the antenna and wire, $\hat{n}_A$ is the versor normal to the pick-up coil surface and $\hat{t}$ is the one orthogonal to the plane which contain the wire and the center of the pick-up coil. In the segment-like approximation the transfer function gets this expression

$$h_s(z) = \frac{\mu_0}{4\pi}(\hat{t}\cdot\hat{n}_A)(N_t\cdot w)\left(\frac{z+L}{d^2\sqrt{(z+L)^2+d^2}} - \frac{z}{d^2\sqrt{z^2+d^2}}\right) \tag{5.7}$$

The two numerical estimation are very close, the segment-like is lower but larger than the point-like. This is in agreement with the selectivity expected, larger is the pick-up coil larger is its interaction with the environment. If two pick-up coil has the same magnetic surface than the smaller is more sensitive (i.e. has a higher maximum).

The segment like antenna has been choose to discussed the numerical results because even if it has a more complicated expression it has an analytical formula and it is closer to the real transfer function (see Fig. 5.12).

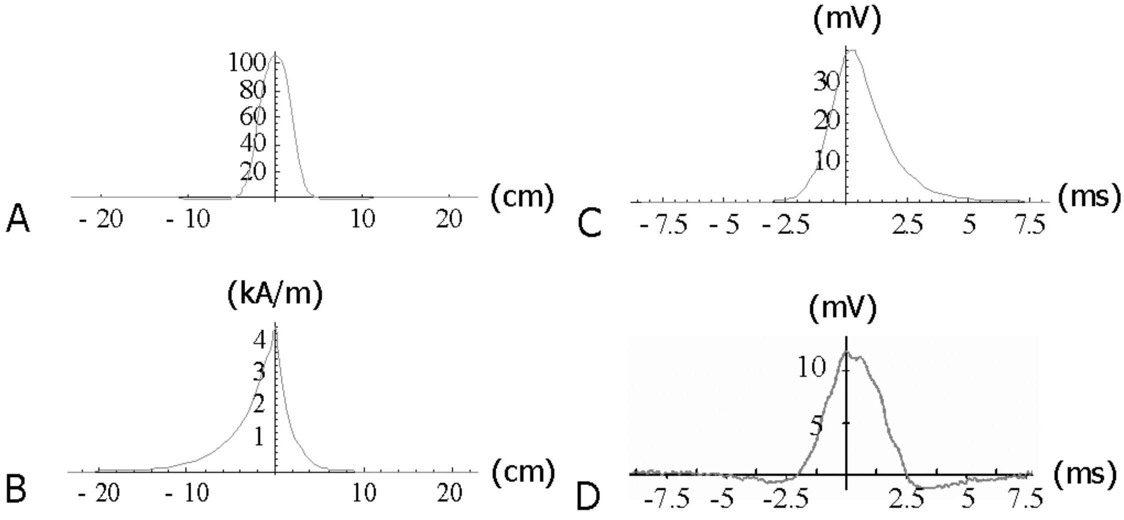

Figure 5.12: A. The geometric transfer function H_{AC} for cable 1. The assumptions for these graphs were that the quench occurred for a beam-pipe such as the left beam-pipe, on the internal side of the top loops of cables, with the quench front travelling in the same direction as the current. Note that H_{AC} is unit-less. B. dI/dz, the derivative of the current redistribution for wire 1. C. The resulting quench signal V_{AC}, the convolution of the graphs in the previous two figures. D. This is an actual quench signal measured by the LQA, that is, two coils of the LQA. The magnitude of the simulated signal is off by a factor of approximately 3; this is due to the twisted structure of the cable which ha not been take into account.

5.6.2 Sensitivity to Left-Right Position of the Quench

The (5.3) has been numerically evaluated using the segment like approximation (5.7) for the transfer function of the pick-up coil and the results are summarized in Table. 5.1. The ratio of the maximum value of both compensation (AC and BD) has been evaluated for all the cable in a quarter cross section of the LHC dipole magnet. [2]

The main conclusion is that the compensation which has the highest signal is the one which has one pick-up coil in the quadrant where the quench starts[3]. The second prediction is the opposite polarity of the two compensation which have always verify form the measurements results.

If the current redistribution zone is shorter than the pick-up coil length then (5.3) gets simpler

$$v(t) = -v_q \Delta I_0 h(-v_q \cdot t) \tag{5.8}$$

and the ratio between the maximum values of the two compensation can be evaluated. This simple calculation is in fair agreement with the more accurate results presented before.

---

[2] Given that the values for the parameters R_1, R_2, and G depend upon the magnitudes of the magnetic field, B_1 and B_2, at the positions of the two wires, the current redistribution $i(z-v_q t)$ is different for each cable. The value for L_{eq}, on the other hand, is a matter of geometry and is calculated to be on the order of 10^{-7} H. For one of the likely quenching cables, cable 1, the values for R_1 and R_2 are respectively taken to be 65.2 $\mu\Omega$/m and 60.5 $\mu\Omega$/m, and the conductivity G is taken to be 2.25×10^7 S/m. Thus, assuming $v_q =$ 30 m/s and $I_{tot} = 11.85$ kA.

[3] There is only cable 21 which does not obey to this general rule and during this first investigation there have been no quench observed in that area.

Cable	$V_{AC,peak}/V_{BD,peak}$	Cable	$V_{AC,peak}/V_{BD,peak}$
1	-2.66	21	-0.72
2	-3.30	22	-3.95
3	-4.41	23	-2.78
4	-4.84	24	-2.52
5	-5.14	25	-2.38
6	-12.62	26	-2.26
7	-6.87	27	-2.17
8	-5.40	28	-2.08
9	-4.46	29	-1.99
10	-3.68	30	-1.91
11	-3.03	31	-1.82
12	-2.36	32	-1.73
13	-1.85	33	-1.63
14	-1.46	34	-1.53
15	-1.15	35	-1.44
16	-2.00	36	-1.35
17	-2.00	37	-1.26
18	-1.97	38	-1.18
19	-1.89	39	-1.11
20	-1.66	40	-1.04

Table 5.1: Voltage-Peak Ratios for a Given Side

5.6.3 The Inverse Problem

One useful result of this model and the success of its simulations is the realization that a simple convolution can relate the quench signal to the changing current distribution via a transfer function. So long as the pattern of the current distribution (or the “redistribution”) travels as a waveform with a constant velocity, and so long as the quench front is propagating along the straight section of the quenching cable, a convolution will describe the interaction of the quench with the LQA. This idea works even for more complicated models of the quenching cable that have more than two wires.

Once the convolving relationship is established, it is not long before the idea of deconvolving a measured quench signal arises. With a good knowledge of the transfer function, a signal can be translated by deconvolution into the actual current distribution, according to the particular model that is used in deriving the transfer function. The good thing is that, once a model is chosen, the transfer function is well known because the LQA is well known and controllable. So a result of this model has been to find a second way of analyzing the raw data of the quench signals.

5.7 The Summary of the First Test Campaign

During the first test campaign the measurements performed with the LQA help in understanding the origin of low quench performance in a few problematic magnets. The training

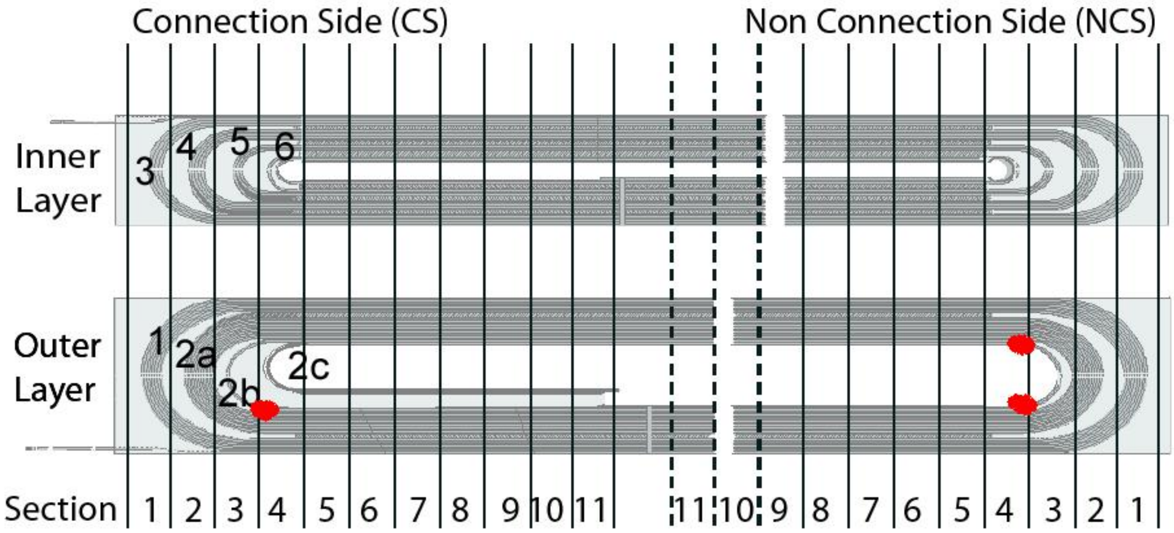

Figure 5.13: The illustrative example of the quench localization in the LHC dipole 2036 by meas of the LQA.

quenches detected in the magnet extremities started in the sixth and in the second block[4]. The quenches located in the 2^{nd} block started only in the sub-parts b and c. The longitudinal position of those quenches was located in a region of few centimeters close to the magnet extremities, in some cases in the bending part where the cable begin to turn and in other cases about 4 cm before. Three pick-up coils are usually activated at the same time in the very beginning of the resistive transition which suggests that the starting quench has a dimension of maximum 12 cm, comparable to the transposition pitch length. This last experimental evidence supports the hypothesis that the quench nucleation is generated by mechanical instabilities in between the two layers of strands in the Rutherford cable.

An illustrative example of the quench origin map as obtained for one of the measured magnets is presented in Fig. 5.13. The summary of the quench localization results analyzed within the first test campaign are show in Table. 5.2. These results have pointed out the particular systematic weak region in the magnet coil structure and served as a basis for the corrective action in industry.

---

[4] During the whole campaign only one quench was detected in a different block, (5^{th})

Magnet	**Quench**	**Aperture**	**Pole**	**Layer**	**Block**	**Region**	**Position**
2036	1	1	low	outer	2b	CS	0
"	2	1	up	outer	2b	NCS	0
"	3	1	low	outer	2b	NCS	0
2069	1	2	low	outer	2b	CS	0
"	2	2	low	outer	2c	CS	0
"	3	2	low	outer	2c	CS	0
"	4	2	low	outer	2c	CS	0
"	5	2	low	outer	2c	CS	0
"	6	2	low	outer	2c	CS	0
2523	1	2	low	outer	2c	CS	0
"	2					SP	
"	3	2	low	inner	6	CS	4
"	4	1	up	inner	5	CS	0
3061	4	2	up	inner	6	NCS	4
3063	1					SP	
"	2	1	low	outer	2c	CS	0
"	3	1	low	outer	2c	CS	0
"	4					SP	
3122	2	2	up	inner	6	NCS	4
"	3	2	up	inner	6	NCS	4
"	4	1	low	inner	6	NCS	40
"	5	1	up	inner	6	NCS	4
"	6	2	up	inner	6	NCS	4
"	8	1	low	inner	6	NCS	4
1123	1	2	low	inner	6	CS	20
"	2	1	low	outer	2c	NCS	0
"	3	2	low	inner	6	CS	4
"	4					SP	
"	5					SP	
"	6	1	low	outer	2b	NCS	4
"	7	2	up	inner	6	CS	0
"	8					SP	
"	10					SP	
"	12					SP	

Table 5.2: The Summary of the First Test Campaign. The CS, NCS and SP stand for connection side, non-connection side and straigth part of the magnet, respectively. The position is defined as the distance in centimeter from the bending part of the magnet extremity (between section 3 and 4) and the actual quench origin (positive distance indicates the direction going inside the magnet.)

Chapter 6

Cable Motion and Quench Origin

The quench location provides the most direct information about the weak points of a magnet. However the causes of a resistive phase transition should also be searched in the instants which precede it. The evidence of fast kink-like signals, later on simply called *spikes*, appearing before the quench suggested their relevance to the quench origin. The most sensible instrument to detect the spikes is the QA (or for a detail study of the magnet extremities the LQA) and it was extensively used during the LHC magnet tests with the aim to provide the data for a detailed analysis of possible correlation of spikes with the quench performance.

In this chapter the characterization methods and the statistical treatment of the spike signals is presented. A criterion to distinguish between the undergoing electrical noise and the spikes, both presents in the QA, is explained. The combined use of transversal and longitudinal compensations scheme is explained.

6.1 Cable motions versus spikes

The spikes present in the QA signal during the powering of the magnet exhibit many properties which suggest their mechanical origin. Investigation of mechanical disturbances in superconducting magnets were studied by recording and characterizing the signals induced in piezo-electric ceramic sensors and accelerometers by spontaneous acoustic emission during magnet excitation [14]. The localization of acoustic emission sources as recorded by the piezos-electric sensors corresponds to the localization obtained by signals recorded on the Quench Antenna which proved the mechanical origin of spikes.

A typical spike signal is shown in Fig. 6.1. After a certain time of inactivity in which the QA signal is almost flat and only small perturbation of electrical origin are present, a sudden sharp (at least in the scale of tens of μs) increasing voltage appearers. After reaching its maximum value the signal gets back and a clear oscillation regime starts which after a certain time disappears and the system is again in its normal quiescent state. This is a common dynamic behavior of any type of elastic media which experience a perturbation from their equilibrium.

The main evidence of the mechanical origin is the propagation of their signal along the magnets, Fig. 6.2. The typical spikes propagation velocity measured ranges between 1 and 2 km/s. This is in fair agreement with the velocity of sound wave predicted by the Youngh

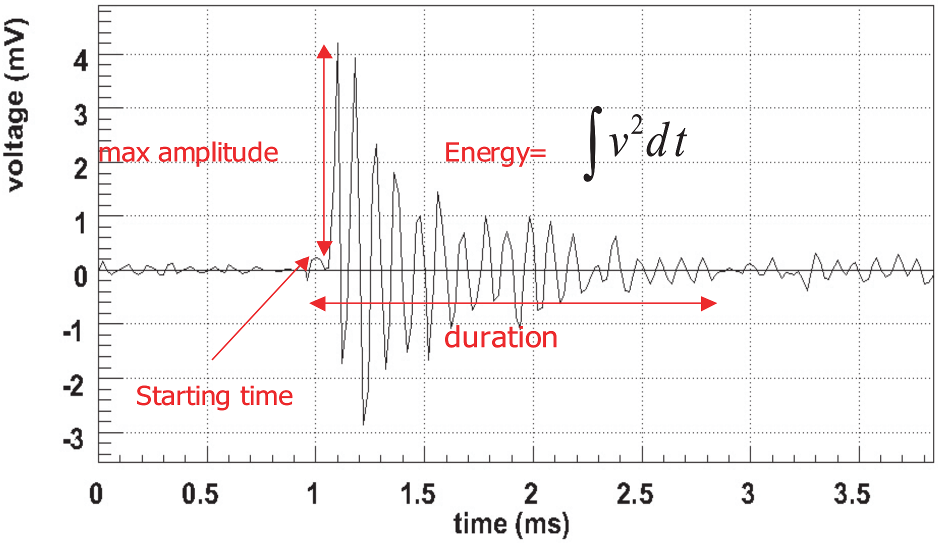

Figure 6.1: An example of a spike signal recorded with the QA. The main parameters used for the spike characterization of the spikes are evidenced.

modulus of the coil. Moreover the propagating spike has a different shape with respect to the original one, the beginning of the propagating signal is no more as sharp as it is the original but it develops more gently and propagates like a wave package.

The major difference between the energization of a short cable sample and a magnet coils is the presence, in the second one, of huge Lorentz forces which acts on it, pushing it towards the collar in the straight part of the magnet and stretching it longitudinally in the magnet extremities, as already discussed in detail in section 2.3.3. This is a very likely source of cable motion which can give rise to the sudden movements followed by relatively long period of inactivity. Moreover this dynamic is very likely seen in system in which friction forces are involved. This phenomenon is usually called stick-slip motion and it is the subject of the next chapter.

The cable motions are a very luckily sources of possible instabilities within the magnet coil. By purpose magnets are designed that the friction keep the cable in a stable position and prevent possible movements. If friction does not keep the cable in a stable position it is the dominant source of heat production while the cable moves and eventually it can provoke a quench if the energy dissipated is above the minimum quench energy (see section 4.5.1).

6.2 Raw data treatment

As already introduced in section 3.4 the signals coming from the pair of pick-up coils are merged in order to compensate the variation of main dipole field. If this last procedure is efficient the result signal is at zero average and not distinguishable from white noise for the

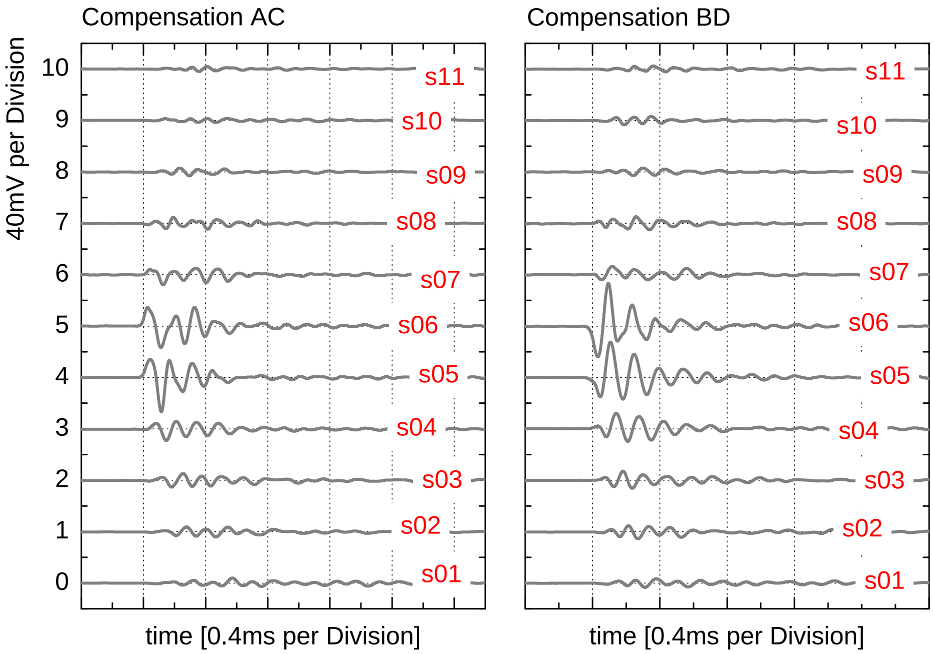

Figure 6.2: An example of a spike signal recorded with the LQA. The spike is originated in the region cover by the pick-up coils in sections 5 and 6 and afterwards the propagating signals is visible on the other. sensors.

most of the time. The whole signal can be described with this mathematical expression

$$s(t) = n(t) + \sum_i \psi_i(t - t_i), \tag{6.1}$$

in which overlapped with noise n there are several functions ψ_i, which brings the information related to cable motions. The knowledge of the standard deviation of the noise, called later simply sigma noise, gives a straightforward criterion to distinguish the information contained in s. As an obvious consequences the cables movements related to signals smaller than the typical noise spread are lost. The sigma noise gives an estimation of the sensitivity of the instrumentation. To get information about smaller and smaller mechanical instabilities much effort should be paid to improved the noise compensation scheme.

6.2.1 Noise and Spikes

The value of the sigma-noise is not a trivial information to achieve because the signal itself has a sigma which may vary. The representation of s in the amplitude space is the starting point adopted to begin the analysis. It is already possible to qualitatively distinguish the presence of tree peaks, the central and biggest one which contains the noise n and the two lateral ones, one at the right and one at the left which are related to the mechanical instability, ψ. To give a rigorous estimation of the threshold, s_{th}, to quantitative separate the noise from the information the following interactive procedure has been adopted. The

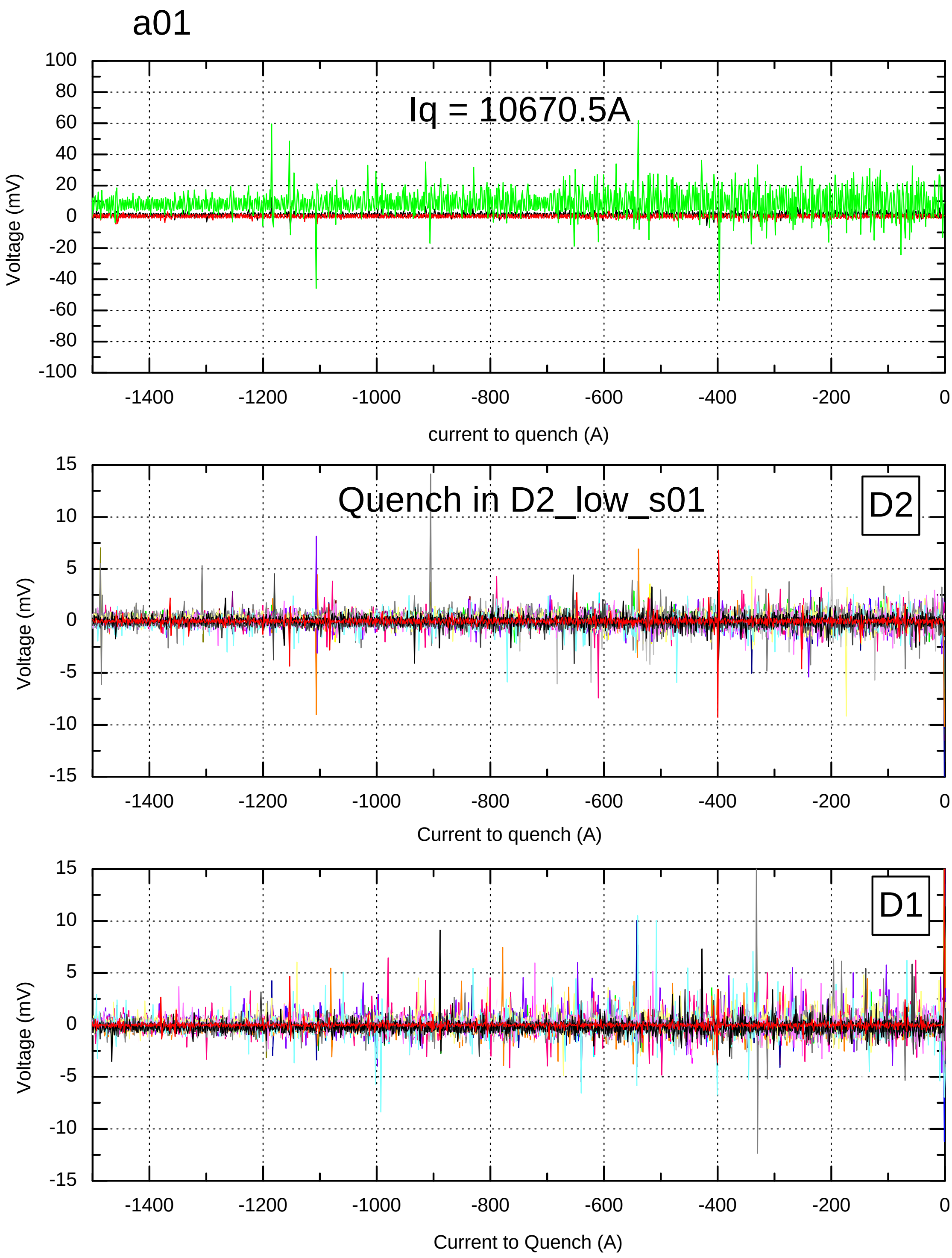

Figure 6.3: The mechanical activity recorded during 150 s before the quench (at 10 A/s). In the first graph the data of the voltage tap signals are presented. In the second and third there are the signals of the QA, for the first and of the second aperture of the magnet, respectively. These data are recorded during the virgin ramp of the magnet where the mechanical activity is present during all the time recorded. The quench appeared at 10670.5 A

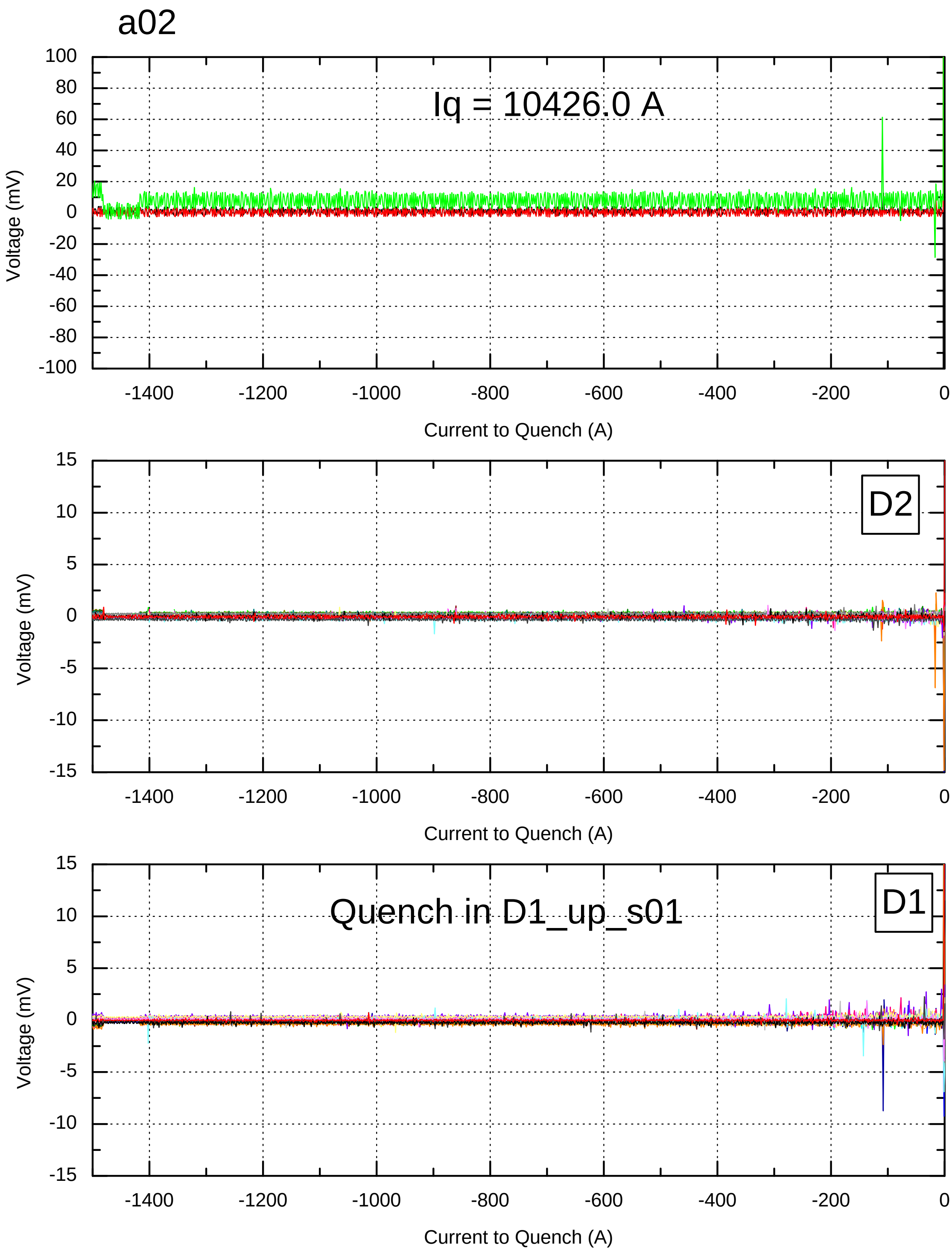

Figure 6.4: The mechanical activity 150 s (at 10 A/s) before the quench. In the first graph the data of the voltage tap signals are presented. In the second and third there are the signals of the QA, respectively the first and of the second aperture of the magnet. This data are recorded during the second ramp of the magnet. The quench appeared at 10426.0 A, about 250 A before the first one. The mechanical activity is not visible as it was during the first ramp but it starts just before the quench.

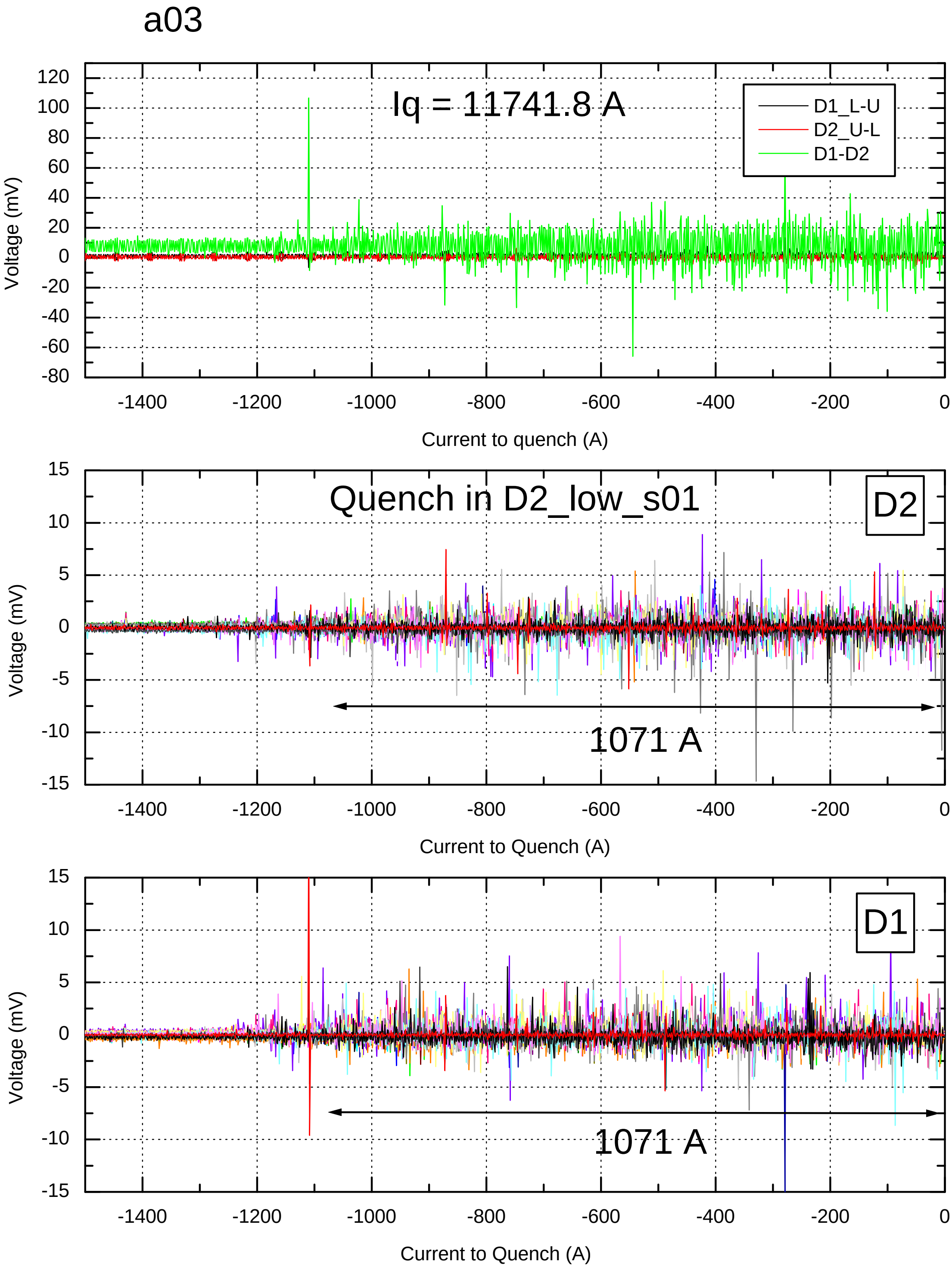

Figure 6.5: The mechanical activity 150 s (at 10 A/s) before the quench. In the first graph the data of the voltage tap signals are presented. In the second and third there are the signals of the QA, respectively the first and of the second aperture of the magnet. This data are recorded during the third ramp of the magnet. The quench appeared at 11741.8 A, about 1071 A after the first one. The mechanical activity starts to be visible about 200 A before the last highest current injected in the coil.

sigma of the whole signal is evaluated

$$\sigma_1^2 = \sum_{i=1}^{N} s_i^2/N, \tag{6.2}$$

and it is called σ_1. A first threshold is defined as $s_{th1} = 5\sigma_1$. A preliminary distinction between signal and noise may be done and this suggests an interactive procedure to approach the expected value. The next evaluation of the sigma is done only on the values which are inside the interval $(-s_{th1}, s_{th1})$. Defining the ensemble of points inside the interval as $\Omega_<$ and the one above as $\Omega_>$ and the respective cardinality $N_< + N_> = N$ the generalization is straightforward

$$\sigma_j^2 = \sum_{s_i \epsilon \Omega_<} s_i^2. \tag{6.3}$$

After few interactions the value of the (6.3) gets stable and equal to the expected σ and the threshold is defined finally as

$$s_{th} = 5\sigma. \tag{6.4}$$

At this point of the analysis a *raw-spike* can be defined as a continuous interval in which the signal is above s_{th}. Several scalar properties are associated to a raw-spike, like the starting time t_{start}, the duration T, the maximum amplitude A and the energy E.

The raw-spikes are the first ensemble of ψ candidates to be mechanical movement. The procedure to validate the goodness of such potential candidates is the so called *globalization* which is divided in two main steps: the reduction of the redundancy and the grouping of the propagating signals along the longitudinal axis.

6.2.2 Globalization procedure

There are several read out signals from the QA shaft which give information coming from the same magnet region: the information is not equivalent because the pick-up coils have a different position inside the magnets bore but at this stage it is important to group them together. All raw-spikes which belong to channels in the same longitudinal position are compared and if several of them are overlapping in function of time then they are grouped together. The one with highest amplitude of the class is considered as the *super-spike* and is chosen as the representant of the group. This procedure is performed separately for the both compensation scheme, the TC and the LC (see section 3.4).

The mechanical origin of such signals imply the possibility of propagation. A super-spike is the signature of a local instability but it may propagate to neighboring sections. It is important to group together super-spikes which has a time overlapping. This procedure brings directly to the definition of a *global spike* as the one with lowest starting time in this ensemble. The statistical differences between super-spikes and global-spikes may be significative and it is considered nevertheless important to be consistent with the physics behind. This procedure is not applied to the LC because the information is delocalized between two different region of the magnet and the reconstruction of a possible propagation left some ambiguities and the efficiency can not be demonstrated.

6.2.3 The Global Spikes

After the globalization procedure a table with all the spikes detected is produced. Each spike is define with a vector of n_s dimensions. The vector components are:

- the starting time, t_s
- the duration of a spikes, T
- the maximum amplitude, A_{max}, defined as the maximum absolute value of the spike signal.
- the energy, defined as the integral of the square of the amplitude
- the waiting time, δt, defined as the time between the spike and the previous one which happened at the same location.

Two table are produced, one for the global spikes detected with the TC signals and a second one for the super-spikes detected with the LC signals. Before analyzing the data, the global spikes detected by mean of the TC are compared with the one detected with the LC compensation and the intersection of these two ensembles is taken. As the representative of this new ensemble of spikes, the information associated with the TC are used. This final procedure helps the rejection of possible impulsive noise (generated mainly by the power supply) which usually affects only the TC signals.

6.2.4 Graphical User Interface

A graphical user interface using ROOT [67] objects was developed to visualize the various statistical parameters relevant to the analysis of the mechanical activities of magnets prior to their quenches. The program is structured as two dynamic lists (Fig. 6.8). The first list is in the form of a tree (magnet builder, magnet name and measurement name) and is linked to the database in which all information about measurements are available. In the second list the analysis of the selected measurements are stored and it is linked to a canvas where all histograms are available for visual inspection and selection of a particular analysis. This general approach gives the opportunity to compare different analysis for different magnets and to upgrade easily the data treatment at any time.

6.3 The Kaiser Effect versus Training

Some special experiments have been performed to study the effects of current cycles on the mechanical activity inside the magnet coil. Already from a visual inspection at the oscilloscope it is possible to notice that during the virgin ramp the mechanical activity is more pronounced than in the following ones. To better quantify this effects special cycles have been performed and the associated signals on the QA have been recorded. The analysis of one of those experiments is presented in Fig. 6.6. When a magnet is powered for the first time its mechanical activity is visible from low current level (about 4 kA) as it can be

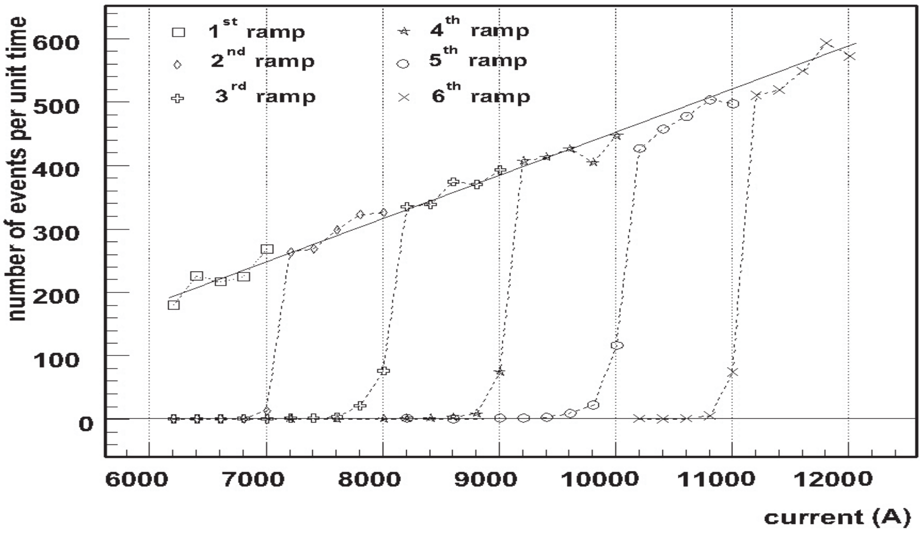

Figure 6.6: The number of spikes per unit time is plotted as a function of the current. The indicated first ramp is also the virgin ramp which means the first time the magnet experiences a current and the associated Lorentz force. During the first ramp the maximal current injected in the coil is 6 kA. After this current is reached the magnet is gradually discharged. During the second ramp the current is increased up to 7 kA, 1 kA more than in the previous ramp. This exercised is repeated several time up to 12 kA

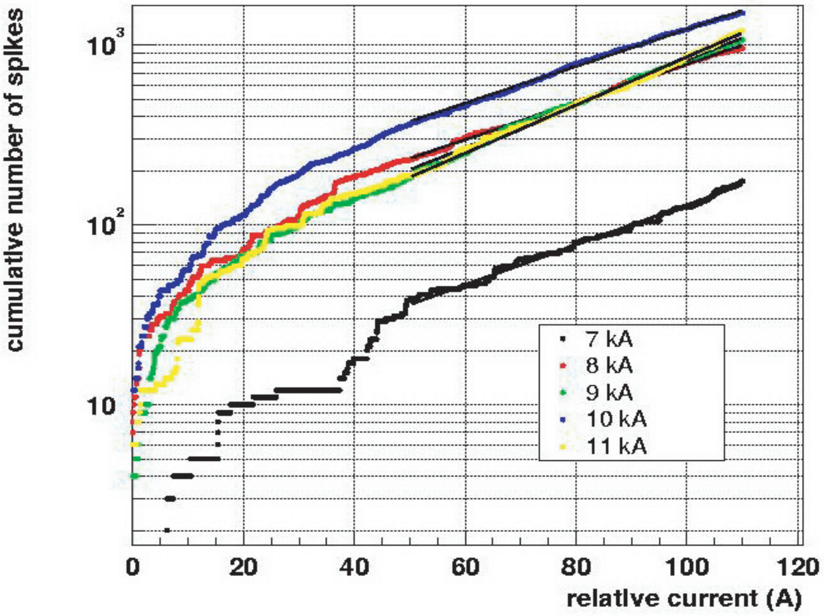

Figure 6.7: The cumulative number of spikes versus relative current while the current is approaching the last previous highest level. The experiment has been carried out at different current level

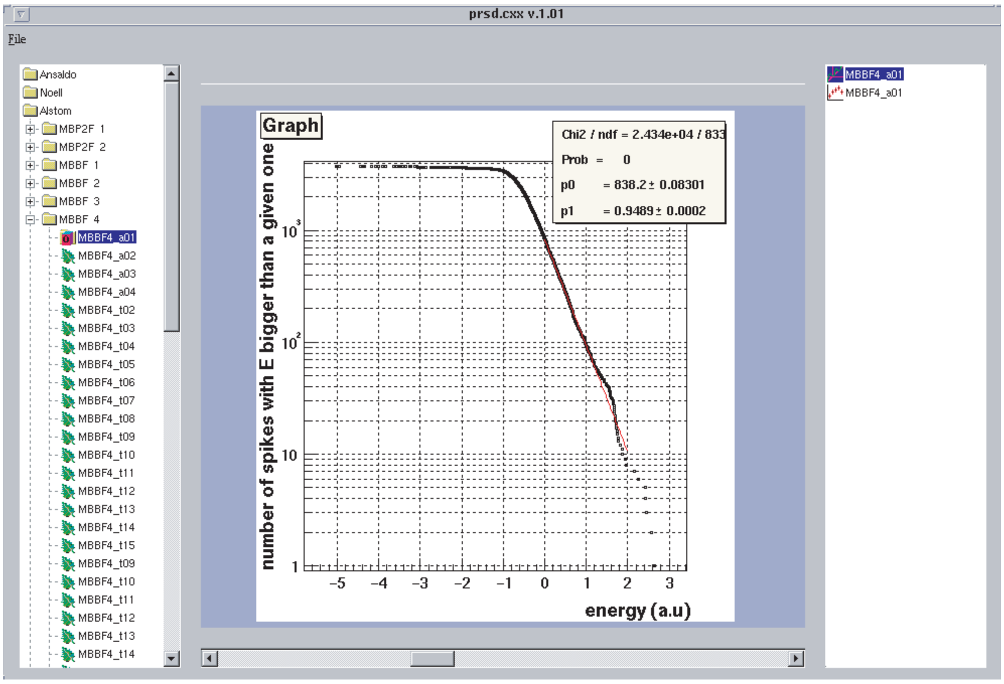

Figure 6.8: The graphical user interface dedicated to the statistical treatment of the extracted from raw measurements spikes.

extracted from the data. If energized magnet is reaching a level I_{max} without quenching and afterwards the current is ramped down, the mechanical activity is no longer visible in the next ramp till the level I_{max} is approached. This simple experiment shows that the magnets have a memory of the previous current cycles. This phenomenon, called the *Kaiser effect*, is at the base of the macroscopic behavior of the quench training. It is the Lorentz force which generates the mechanical activity and it is also the Lorentz force which compacts the coils inside the force retaining structure (collars) and put it in a more stable state. The described above experiment is a possible microscopic measure of the training efficiency of a magnet.

Another remarkable phenomena, illustrated in Fig. 6.7, is the exponential-like increasing of the number of events while the system is approaching the last highest current.

6.4 Statistical treatment

Within the standard measurement program for the LHC dipoles each magnet is energized at the nominal current ramp rate (10 A/s) and all signals are recorded 9 s before the quench. To analyze these data it is important to know the magnet powering history. The memory and consequently the non reproducibility of the experiments makes the statistical treatment of the data more critical because it is not possible to repeat the experiments. As a consequence the statistical objects that are described in the following are to be considered as a static picture of an irreversible and dynamic phenomenon, like for instance in the statistics of earthquakes [51].

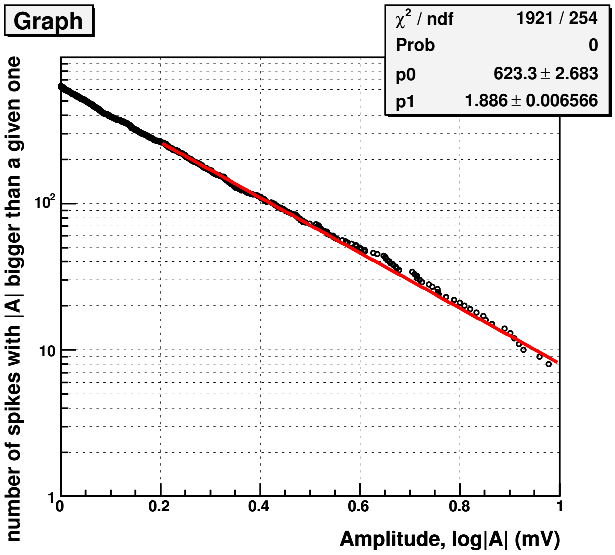

Figure 6.9: Example of cumulative distribution for the maximum amplitude of spikes, normalized with A_0=1 mV. The data are fitted with a power law.

6.4.1 Cumulative distribution

The main parameters chosen to describe the mechanical activity in a magnet are the maximal amplitude and the energy of a spike. The cumulative distributions of these parameters are evaluated in order to avoid the problem of choosing a bin size. This distribution has not been normalized to one but to the number of spikes per unit time:

$$P_{>} = \frac{\Delta N}{\Delta t} \int_{x}^{+\infty} p(\xi) d\xi, \tag{6.5}$$

where ΔN is the total number of global spikes detected during the observation time Δt (9 s) and x is the normalized parameter (for example $x = A/A_0$). The (6.5) gives the number of spikes per unit time which has a parameter bigger than a given value. This approach has been used to save the information related to the time dependent phenomena. To reduce the information a power law is used to fit the (6.5) the cumulative distribution (beween 1 and x_s) like in the example of Fig. 6.9:

$$f(x) = n \cdot x^{-b}, \tag{6.6}$$

where n is the number of spikes per unit time with x bigger than one and b is a positive number which characterizes the probability decay of x: the bigger is b the lower is the probability to observe an event characterized by x. If b is less than one the mean value is not defined and if b is less than two the sigma is not defined. The power law distribution is also endowed with a remarkable property, known as *self-similarity* or *scale invariance*: the ratio of the the probability of two values is only a function of the ratio of these variations,

$$\frac{f(x_a)}{f(x_b)} = \left(\frac{x_a}{x_b}\right)^{-b}. \tag{6.7}$$

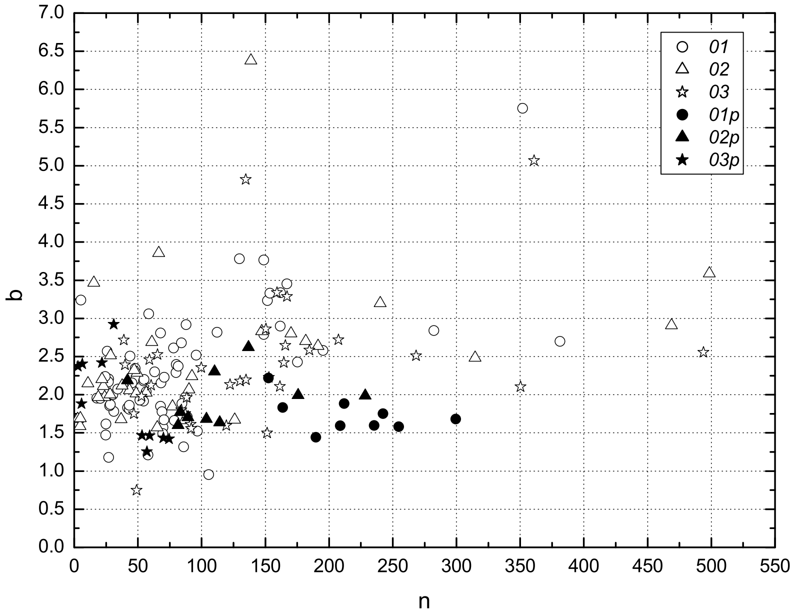

Figure 6.10: The results of the power law parametric analysis of the spikes maximum amplitude, obtained for the reference amplitude A_0=1 mV and observed in pre-series (01,02,03) and prototype (01p,02p,03p) LHC dipole magnets families.

This simple approach describes the mechanical activity of a magnet with a point in a two-dimensional parameter space. On the contrary it is not always the best fit for some measurements. Several parametric distributions have been taken into consideration as possible candidates but even if they were suitable in several cases the power law was found to be the most general with lowest number of parameters.

Builder	$< n >$	σ_n	$< b >$	σ_b	Number of quenches
01	84.6	71.12	2.3	0.75	67
02	100.5	119.8	2.43	0.9	35
03	143.5	100.5	2.38	0.84	33
01p	255.7	128.27	1.77	0.25	10
02p	116.5	53	1.95	0.34	10
03p	38.2	27.9	1.9	0.58	10

Table 6.1: Example of Analysis for Preseries and Prototypes LHC Superconducting Magnet families

6.5 Training Quench Analysis

The spikes dynamics recorded during the quench training is followed in the n versus b space. In Fig. 6.10 and Table 6.1 the results of the parametrization for the prototype and pre-series of

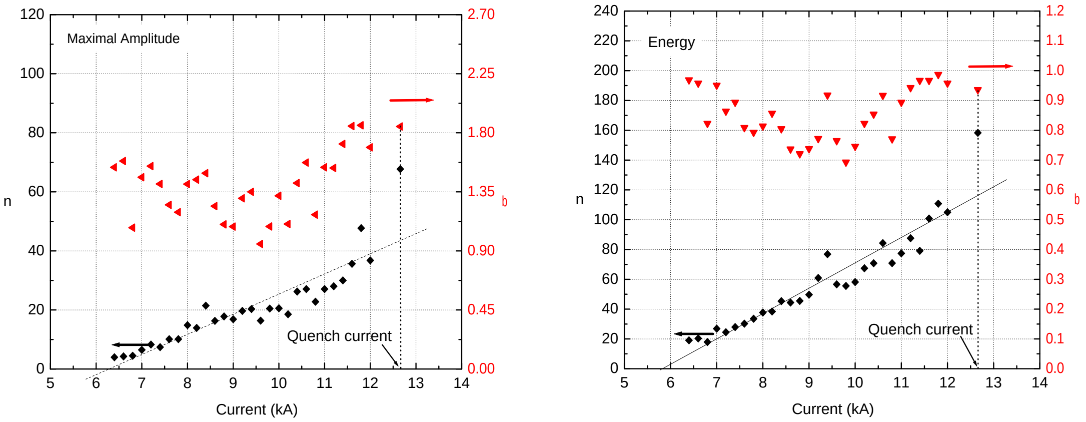

Figure 6.11: Parametric study of the maximal amplitude and of the energy during the whole ramp to predict its quench performance

dipole magnets, grouped in terms of production lines in six families of magnet, are presented. The mean and the standard deviation for n and b have been evaluated and are shown in Table. I. Via those parameters it is possible to define an ensemble of points which is grouped around the mean values with a spread of σ which represent the general trend. All the magnets which have been found out of this region have shown a low quench performance. Conversely some problematic magnets have been found inside. For the pre-series dipole magnets exhibiting a good quench performance it is no longer possible to clearly identify a particular magnet builder, as was the case for prototypes. This suggests that the procedures applied to wind the coils and assembly of the cold mass are, as desired, getting homogeneous among the firms, at least with respect to this particular analysis.

6.6 Towards Quench Level Prediction

To improve the statistical predictability of the quench performance special tests have been performed. The global mechanical activity has been investigated for several current levels before the quench and both n and b have been plotted as a function of the current, Fig 6.11. The parameter n increases linearly with the current until the quench level is approached. The value of n which corresponds to the 9 s before the quench is clearly out of the linear trend. A new mechanical regime seems to be correlated with the origin of the quench and this was observed for several magnets. Recording spikes during powering brings useful information about the quench performance and can be used as the standard test to check mechanical stability of the magnet production.

6.7 Mechanical activity of coil ends measured with the LQA

The magnets extremities do behave differently with respect to the magnet straight part. There is the evidence, already mention, that it is the most likely place in which the resistive transition is triggered by spike events. A detailed studied of the mechanical activities in the coil ends indicate also a different behavior which can be the origin of their weakness.

In Fig. 6.12-6.13-6.14 three examples of the mechanical activity recorded with the LQA making use of the very new long pre-trigger acquisition system. The preliminary analysis of the raw data indicates that the Kaiser effect in the magnet ends is not as pronounced as in the rest of the magnet. This lack of memory is at the origin of long training behavior in certain magnets. In several problematic magnets which needed a very long quench training to reach the target performance the magnet ends show very little memory. This indicates that the spike distribution measurement can serve as a possible quantification of the goodness of the magnet winding, directly from the microscopic properties of the coils. This is moreover a predictive tool which gives information about the coil stability without the need of quenching the magnet.

Another remarkable result is the pronounced differences between the mechanical activity in the connection side (also called MRB) and in the non connection side (also called CFB). These two extremities of the magnets have a different mechanical structure. The connection side is more complex because there are more components used to retain the forces acting on the cables and this can be at the origin of the higher activity and lower memory observed in that area.

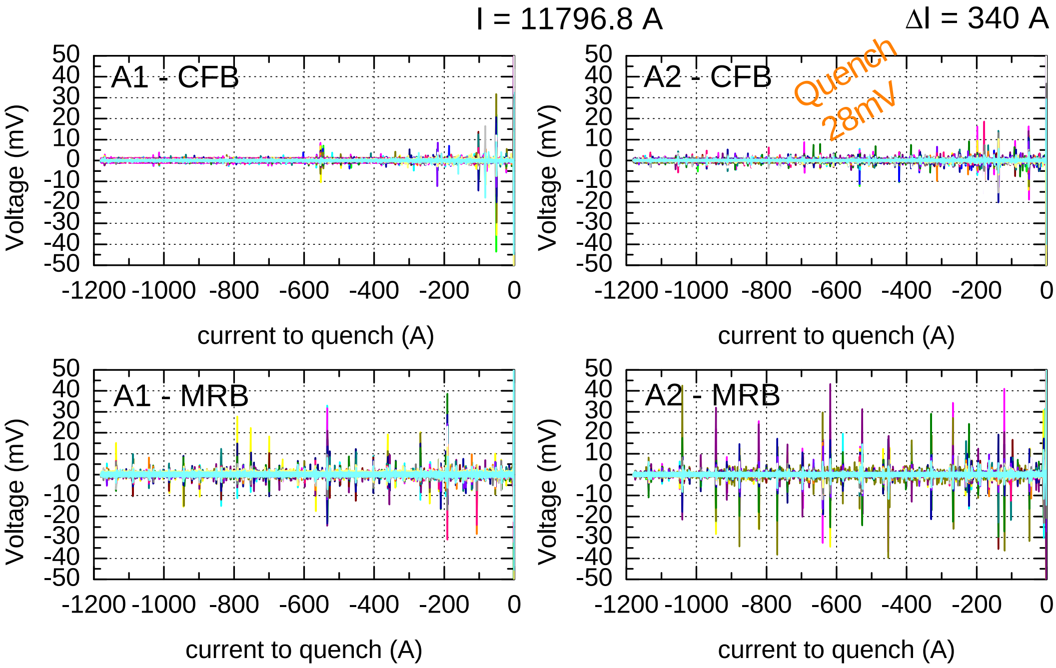

Figure 6.12: The mechanical activity recorded with the LQA on the four extremities of the LHC dipole magnet during 120 s before the quench. The quench current level is 11796.8 A, while the previous one was 340 A lower.

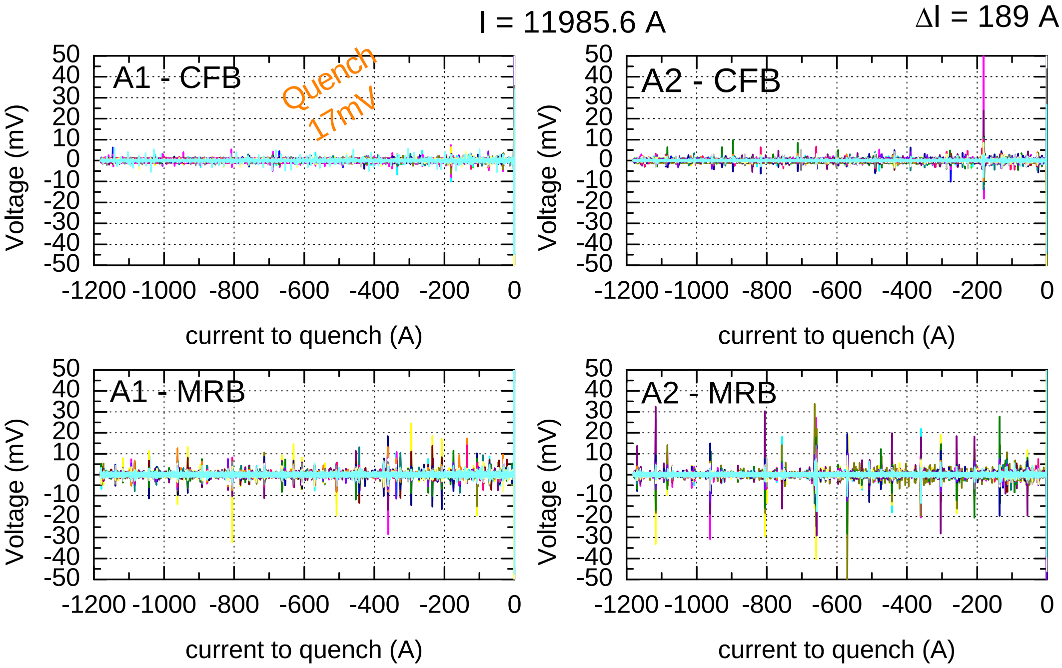

Figure 6.13: The mechanical activity recorded with the LQA on the four extremities of the LHC dipole magnet during 120 s before the quench. The quench current level is 11985.6 A, while the previous one was 189 A lower.

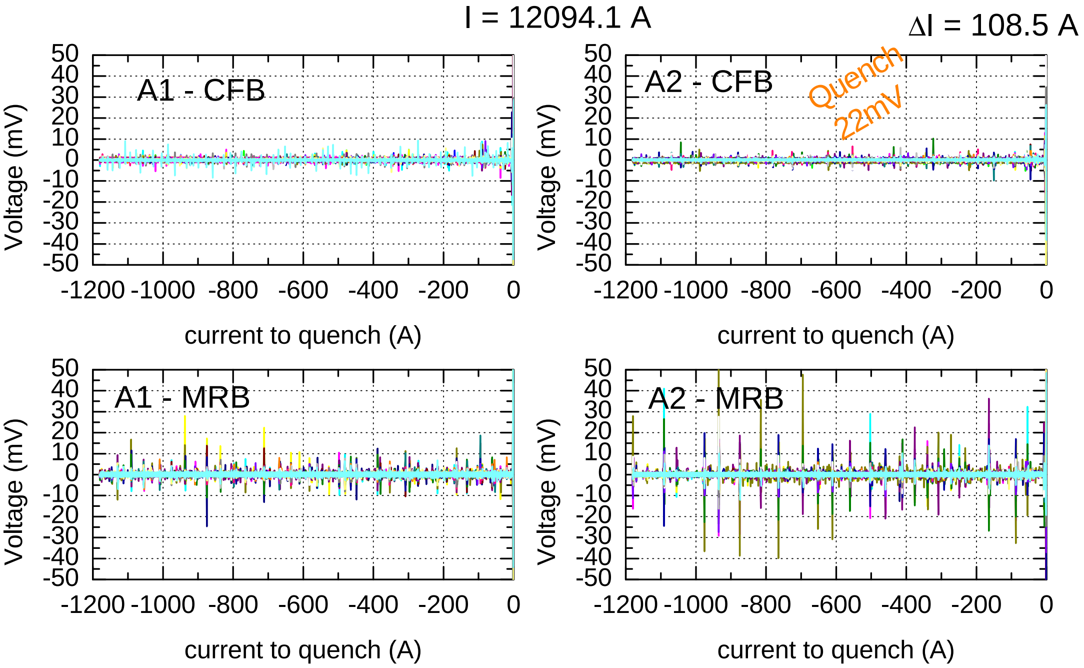

Figure 6.14: The mechanical activity recorded with the LQA on the four extremities of the LHC dipole magnet during 120 s before the quench. The quench current level is 12094.1 A, while the previous one was 108.5 A lower.

Chapter 7

Modelling Instabilities

In this chapter a possible interpretation of the phenomenology of the mechanical disturbances measured by means of pick-up coils are discussed. Starting with a short resume of main experimental evidences a simple spring block model in presence of solid friction is introduced. This approach aims to analyzes the origin of the stick-slip dynamics and the mechanical hysteresis. Afterwards a system of coupled spring block model is defined and the parallel with similar toy-models used in theoretical earthquake physics is discussed. The sensitivity of such system with respect to the starting conditions is analyzed and the role played by solid friction model is clarified. The dynamics and the statistical properties of such system are computed using a cellular automaton equivalence both in one and in two dimension and the qualitative agrement with the phenomenology is evidenced.

7.1 The Phenomenology

Before discussing the details of the models proposed, it is convenient to schematically resume the emergence phenomenology knowledge gained during the experimental investigation which defined the common properties observed among several hundred magnets tested.

1. **Stick-slip dynamics** - The system evolves intermittently with period of tranquillity interrupted by bursts of activity, rather than following a smooth gradual path. This is a common behavior among several natural systems like for instance earthquakes, volcanic eruptions, solar flanges, gamma-ray burst and biological evolution.

2. **Positive activity** - The system is active only when the force applied is increased. There is no activity while the force is kept constant or while it is decreased.

3. **Propagation** - The events, even if well localized in a narrow region, do propagate to neighboring parts.

4. **Kaiser effect** - One of the most remarkable properties of such system is the capability to memorize the last highest force which was applied during its history.

5. **Meta-stability** - While the system is approaching the last highest force applied the mechanical activity reactivate with an exponential-like increase of events per unit time.

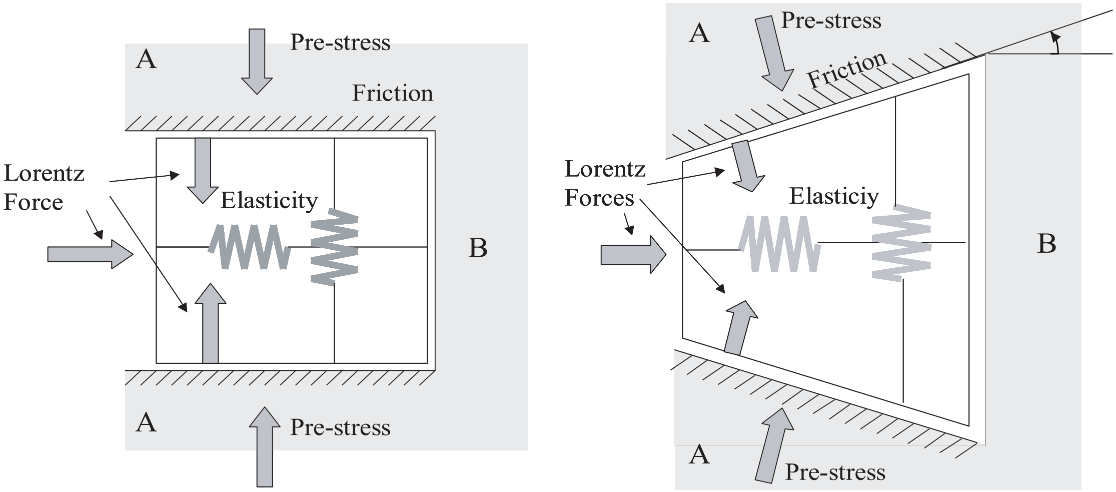

Figure 7.1: The schematic representation of the LHC dipole cross section. The coil is considered as an elastic media compressed inside the collar and pushed by the Lorentz forces in a regime of solid friction. On the left side the symmetric model and on the right side the asymmetric one

6. **Power law correlation** - The *energy* of the events has a very wide spectrum of values and its cumulative distribution function turn out to be best fitted with a power law correlation function.

7.2 The Spring Block Model with Solid Friction

The first and the simplest model introduced to interpret the phenomenology of measured mechanical disturbances is the spring-block system as it is sketched in Fig. 7.1. The half-cross section of the magnet coil is represented as an elastic media (later on called simply the *block*) imprisoned inside of a collar. The region of the collar denominated A compresses the block in the y direction and the region region B inhibits the possible movements of the block against the acting Lorentz force in the x direction. Between the block and the collar there are friction forces. The equation which govern the system dynamics can be formulated as the following:

$$m\ddot{x} = -kx - f(\dot{x}) + F_{ex}(t), \tag{7.1}$$

where m is the mass of the block and k its elasticity, F_{ex} is the external applied force (the Lorentz force). The frictional law f is described in Fig. 7.2 (solid line). It ranges between $\pm f_{th}$ at zero velocity and decreases monotonically to zero while the absolute value of the velocity increases.

Neglecting at a first analysis all the dynamic effects ($\ddot{x} = 0$ and $\dot{x} = 0$) the (7.1) reduces to

$$F_{ex} = kx + f(0), \tag{7.2}$$

where the external applied forces are equal the elasticity of the block plus the solid friction.

In Fig. 7.3 the equation (7.2) is represented in the plane F versus x/k. The center of the diagram represent the virgin state of the block. When the external force is applied the block do not experience any movement until the threshold of the static friction f_{th} is reached. When the force exceeds f_{th} the system starts moving and the elasticity of the system starts overtaking the external applied force. This dynamics is irreversible and even if the force is suddenly released the block remains at the position and does not get back to the original position. The irreversible regime finishes when the applied force exceed twice the static threshold. Above this second characteristic value the system starts to follow a reversible path where the block position follows the applied force: when the force increases of δF the block moves on the right and when the force δF is released the system gets back to the previous position. The geometry as the one described in the left side of Fig. 7.1, are responsible for an asymmetrical behavior along the x axis. The interpretation previously introduced is still valid if two equivalent threshold values for the friction forces are introduce, which gives rise to an asymmetrical hysteresis diagram like the one presented in the right side of Fig. 7.3.

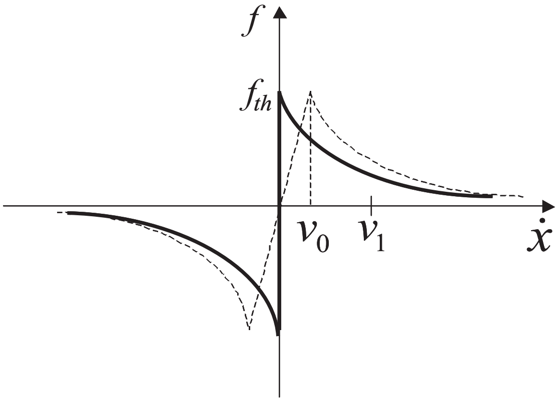

Figure 7.2: Two possible models for solid friction.

Already the static description allows to understand the mechanism responsible for the memory effect. Considering the dynamic properties of the system it is possible to predict that the system very unlikely experiences a uniform motion under the external applied forces. This is related to the properties of the solid friction and to the inertia of the system [34]. This last parameter is not easy to be characterized, but it is nevertheless accepted that the dynamic friction forces are lower than the static which implies that the forces needed to keep a body at constat velocity are lower than needed to start its motion.

7.2.1 Model results

The first remark is that this simple system is capable to reproduce the stick-slip dynamics and the memory of the system. The number of events per unit time is zero for a constant applied force, constant for a linearly increasing force and linear for a quadratically increasing forces, as experimentally observed for the magnets. On the contrary, the size of a slipping event predicted by the model has a constant magnitude. This is not in agrement with the experimental observation during which a great variety of events have been measured.

7.3 The One-dimensional Coil Model

The detected motion inside the coils are localized in different places along the magnet and nevertheless they can generate perturbation in their neighborhood which is well proved by

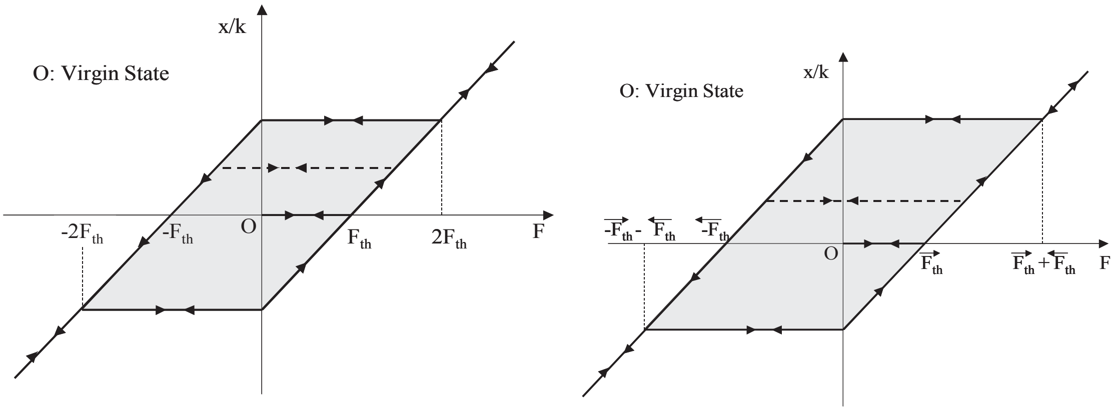

Figure 7.3: The schematic model of the hysteresis for a spring block system in presence of solid friction.

the propagation signal which is always associated to the original one. The natural extension of the previous model is given by the introduction of the longitudinal dimension of the magnet coil. The system can be considered as a collection of spring-block system as the one previously introduced. In first approximation a linear relation is used to model the nearest neighbor coupling. A schematic representation of such system is given in Fig.7.4. The equation of the system reads like:

$$m\ddot{x}_i = k_c(x_{i+1} + x_{i-1} - 2x_i) - k_p x_i - f(\dot{x}_i) + F_{ex}(t), \tag{7.3}$$

where k_c represents the elasticity of the cable to transversal deformation, F_{ex} is the Lorenz force, f is the friction force which depends only on the velocity of the block:

$$f(\dot{x}) = f_0 \phi(\dot{x}/v_1), \tag{7.4}$$

where ϕ vanishes at large values of its argument and is normalized so that $\phi(0) = -\phi'(0) = 1$, and v_1 is the speed that characterizes the velocity dependence of f.

The last term is the k_p which estimate the forces trying to stabilized the block position after a movement. Before discussing the general solution it is interesting to evaluate some possible analytical solutions and their stability.

7.3.1 Dimensionless formulation

It is convenient to begin the analysis of (7.3) by rewriting it in a scaled form that helps in understanding the roles played by the various length and time scale that occur in this system. The most natural choice for the time variable may be expressed as:

$$\tau = \omega_p t, \quad \omega_p^2 = k_p/m. \tag{7.5}$$

The quantity $2\pi/\omega_p$ is the period of oscillation of a single block attached to a compressed spring (k_p) in absence of solid friction. The displacement corresponding to a force f_0 is $D_0 = f_0/k_p$ and this is chosen as the natural unit to measure x:

$$x_i = D_0 U_i = (f_0/k_p) U_i. \tag{7.6}$$

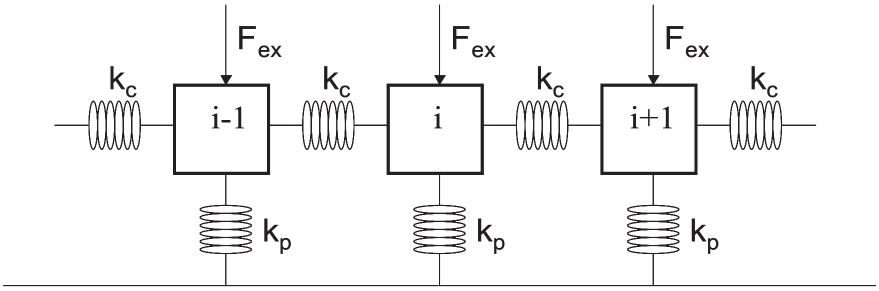

Figure 7.4: Block and spring system for the *one-dimensional coil model*. In this analysis the system is considered homogenous, composed of equal masses m, each connected to its nearest neighbors by springs of strength k_c, and to a stationary surface with springs of strength k_p. Each mass is subject to an external applied force which compress the system towards the retaining surface. The plane (xz) acts as a friction force $f(\dot{x})$, which depends only on the velocity of the block. The equilibrium spacing is a which does not enter directly into the equation of motion.

In this new units of time the (7.3) becomes

$$\ddot{U}_i = l^2(U_{i+1} + U_{i-1} - 2U_i) - U_i - \phi(\dot{U}_i) + \gamma(\tau), \tag{7.7}$$

where

$$l^2 = k_c/k_p. \tag{7.8}$$

7.3.2 Continuum Limit

There is no natural length scale for measuring position along the coil; the equilibrium spacing between blocks, denoted by a, so far appears nowhere in these equations. It is nevertheless convenient to consider the continuum limit. Introducing

$$z = ia, \quad \xi = la = a\sqrt{k_c/k_p}, \tag{7.9}$$

$$\ddot{U} = \xi^2 \frac{\partial^2 U}{\partial z^2} - U - \phi(\dot{U}) + \gamma(\tau), \tag{7.10}$$

it is clear that ξ in the continuum limit remain finite because m, k_p and f_0 scales like a and k_c like a^{-1}.

Change of Variables

Before the analysis of certain special solutions, it is convenient to perform a change of variables. The dynamics of this system can be split in two major contribution: the motion of the center of mass as the reaction to the external applied force and the deviation from it. Defining

$$U(z,\tau) = \langle U \rangle(\tau) + u(z,\tau), \tag{7.11}$$

where $\langle U \rangle$ is the coordinate of the center of mass given by

$$\langle U \rangle = \frac{1}{\|Z\|} \int_Z U(z)dz, \tag{7.12}$$

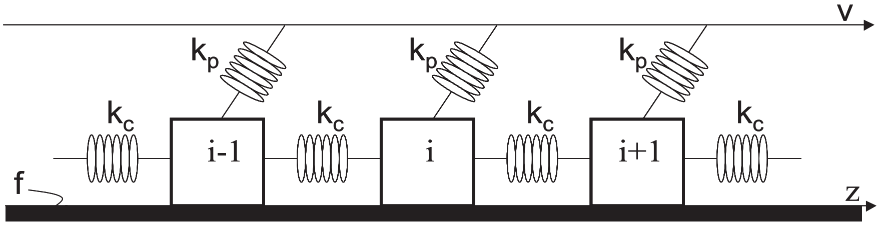

Figure 7.5: Block and spring system for the *Burridge-Knopoff model.* In this analysis the system is considered homogeneous, composed of equal masses m, each connected to its nearest neighbors by springs of strength k_c, and to a stationary surface with springs of strength k_p. Each mass is subject to the friction force $f(\dot{x})$, which depends only on the velocity of the block. The equilibrium spacing is a which does not enter directly into the equation of motion

and u are the fluctuation. Substituting the (7.11) into the (7.10), the equation of motion becomes:

$$\langle \ddot{U} \rangle + \ddot{u} = \xi \frac{\partial^2 u}{dz^2} - \langle U \rangle - u - \phi(\langle \dot{U} \rangle + \dot{u}) + \gamma(\tau). \tag{7.13}$$

The equation (7.13) can be split in two

$$\langle \ddot{U} \rangle = -\langle U \rangle - \phi(\langle \dot{U} \rangle) + \gamma(\tau), \tag{7.14}$$

$$\ddot{u} = \xi \frac{\partial^2 u}{dz^2} - u - \phi(\langle \dot{U} \rangle + \dot{u}) + \phi(\langle \dot{U} \rangle). \tag{7.15}$$

Since this particular research is intended mainly to characterize the fluctuations (u) of the system more than to understand the motion of center on mass, a simple monotonic solution of the (7.14) is supposed and the velocity

$$v(\tau) = \langle \dot{U} \rangle(\tau), \tag{7.16}$$

is defined as a known input parameter. This approach simplifies the study to the (7.15) which becomes

$$\ddot{u} = \xi \frac{\partial^2 u}{dz^2} - u - \phi(v + \dot{u}) + \phi(v). \tag{7.17}$$

The Eq. (7.17) is the same equation of motion which characterized the *Burridge-Knopoff model* [40, 45] shown in Fig. 7.5.

7.3.3 Some Special Solutions

The Constant Solution

A trivial solution of (7.15)

$$u(\tau) = 0, \tag{7.18}$$

which states that the system is undergoing a uniform motion under the pushing velocity v and there are no fluctuations superimposed. This solution is most unlikely seen in the real system. Due to the chosen form of the frictional law this solution is unstable against small perturbation of all wave length. Substituting the following expression

$$u(z, \tau) = u_0 \exp(iqz + \alpha\tau), \tag{7.19}$$

into the Eq.(7.17) results in:

$$\alpha^2 u = -\xi^2 q^2 u - u - \phi(v + \alpha u) - \phi(v). \tag{7.20}$$

Linearization of Eq.(7.21) with respect to u_0, leads to the equation which relates the wave length to the amplification rate α:

$$\alpha^2 = -\xi^2 q^2 - 1 - \alpha\phi'(v). \tag{7.21}$$

Solutions of this equation are

$$2\alpha = -\phi'(v) \pm \sqrt{\phi'(v)^2 - 4(\xi^2 q^2 + 1)}. \tag{7.22}$$

The real part of the amplification (α) remains positive for all q. For the reason that it remains finite for all q , the instability is not the cause of divergences at finite time; deformation of arbitrary wave length do not grow arbitrarily rapidly. On the other hand, any small irregularity in the positions of the blocks, no matter how long or short its wavelength, is amplified while the system is slipping in this manner.

The Periodic Solution

Another partially uniform solution of the (7.17) is when the whole system undergoes a periodic motion satisfying this equation

$$\ddot{u} = -u - \phi(v + \dot{u}). \tag{7.23}$$

The system alternatively sticks until the threshold value of the solid friction is reached and then slip until the compressed spring has not absorbed enough force to stop the motion.

This uniform stick-slip motion is also unstable. A linear stability analysis (similar to the one discussed above) indicates that, as the system passes through the region of slipping speed for which ϕ' is negative, irregularities in the positions of the blocks are amplified essentially by the mechanism that was described for the constant solution.

The Propagating Kinks

The Eq. (7.17) also admits periodic solution in the form of propagating kinks. This dynamics can be described using the following form:

$$u(z, \tau) = u(\tau \pm z/\beta). \tag{7.24}$$

In this case u satisfies

$$(1 - \xi^2/\beta^2)\ddot{u} = -u - \phi(v + \dot{u}), \tag{7.25}$$

which is almost the same as the (7.23) except for a reduced "mass". These kinks must propagate at speed β which is higher than the sound speed ξ in order that the mass remains non-negative. This solution, even if unstable like the previous ones discussed, coexists with the general chaotic dynamic and it is observed during large events like pointed out in [45].

7.4 The one dimensional cellular automata equivalence

The model consists of a one-dimensional chain of blocks and springs being pushed uniformly at a certain velocity v_p, trough the pushing springs and undergoing stick-slip motion. Supposed f_i is a total force with acts on the i-th block through sprigs attached to it. The forces f_i are related to the displacements of the blocks from their natural positions x_i by

$$f_i = -k_p(x_i - v_p t) + k_c(x_{i+1} + x_{i-1} + 2x_i), \tag{7.26}$$

where k_c and k_p are the spring constants for the connecting and the pushing springs respectively, v_p is the equivalent pushing velocity which assuming a constat increasing forces $(F_{ex} = \eta t)$ is simply $v_p = \eta / k_p$.

The dynamics of the model is essentially identical to the one already presented in [47, 48]. It is defined as follows: if all the f_i's are smaller than a threshold value f_{th}, then all the blocks are stuck and x_i's are constant in time. In this time slot the f_i's increase continuously by a uniform rate $k_p v_p$ per unit time. As soon as one of the forces reaches the threshold f_{th}, that block is assumed to slip by a certain distance to relax a certain amount of force δf. During the elementary process, all the other blocks are assumed to be stuck. Then part of the relaxed force δf is distributed equally to the neighboring blocks, namely if the j-th block is slipping, this process is given by the change of forces from f_i's to f_i''s as:

$$f_j = f_{th} \rightarrow f_j' = f_{th} - \delta f, \tag{7.27}$$

$$f_{j\pm1} \rightarrow f_{j\pm1}' = f_{j\pm1} + 0.5\Delta\delta f, \tag{7.28}$$

and all the other f_i $(i \pm j, j \pm 1)$ are unchanged. In Eq. (7.28), Δ is a ratio of the distributed force to the relaxed force and in accordance with E. (7.26) is given by

$$\Delta = \frac{2k_c}{k_p + 2k_c}. \tag{7.29}$$

If the neighboring forces $f_{\pm1}$ before this process are small enough to make $f_{j\pm1}'$ smaller than f_{th}, no more slipping ensues and all the forces start increasing uniformly again until a next event occurs. On the other hand if the neighboring forces are close enough to f_{th} and $f_{j\pm1}' > f_{th}$, then these blocks also start slipping and the forces will be relaxed according to the amount of excess forces over f_{th}. The part of the relaxed force will be redistributed to neighboring blocks again. The elementary processes are defined in the following way. Suppose f_j exceed f_{th}, then

$$f_j \rightarrow f_j' = \phi(f_j - f_{th}), \tag{7.30}$$

$$f_{j\pm1} \rightarrow f_{j\pm1}' = f_{j\pm1} + 0.5\Delta(f_j - f_j'). \tag{7.31}$$

This process will be repeated until all the forces become smaller than f_{th}. The relaxation function ϕ defines how much forces will be relaxed when the f_i's exceed f_{th} and should satisfy the conditions

$$\phi(+0) = f_{th} - \delta f, \tag{7.32}$$

$$|\phi(x)| < f_{th} \quad, x \geq 0 \tag{7.33}$$

The parameter δf defines the smallest event where only a single block is involved. Defining ϕ as a decreasing function, at least for small x, in order to allow even a small event to be amplified, what leads to a larger one, which is supposed to imitate an effect caused by the velocity-weaken friction. The parameter α defined as

$$\frac{d}{dx}\phi(x)\mid_{x=+0}=\alpha, \tag{7.34}$$

characterizes the way the forces are relaxed in the small events. The uniform increase of forces starts only alter these precesses are settled, which means that the duration time of the processes is assumed to be zero.

Each event consists of the sequence of processes of this kind and is embedded in the uniform increase of forces. The moment of event is defined in the following way. Suppose that the values of the force and displacement just before and after the event are $\{f_i, x_i\}$ and $\{f_i', x_i'\}$ respectively. Then the moment of the event E is defined as

$$E \equiv \sum_i (x_i' - x_i) = k_p^{-1} \sum_i (f_i - f_i'), \tag{7.35}$$

and the magnitude of the event as

$$\mu \equiv log_{10}E. \tag{7.36}$$

The distribution function $R(\mu)$ of the magnitude of events μ per block per unit time is introduced. It satisfies the sum rule

$$\int_0^\infty 10^\mu R(\mu) d\mu = v_p, \tag{7.37}$$

which simply reflects the fact that each block is moving at the velocity v_p on the average.

There are three basic parameters for this system, namely: Δ, δf and α. The parameter Δ defined by the (7.29) is related to k_c/k_p and characterizes the system "stiffness". If Δ is small, a large part of the forces is relaxed through pushing springs during events. As a consequence events tend to localize. On the other hand if Δ is close to unity, most of the relaxed force will be taken over the neighboring blocks and events tend to extend over a large spatial region.

In the one-layer coil model the parameter δf that defines the smallest events may be related to the pushing velocity v_p because the moment of the smallest event is proportional to the v_p there. It is important however, to note that v_p itself in the present plays no role.

In the following numerical simulations $v_p = k_p = f_t h = 1$. As for the relaxation function ϕ the following formula has been used

$$\phi(x) = \frac{(2-\delta f)^2/\alpha}{x + (2-\delta f)/\alpha} - 1, \tag{7.38}$$

which is a simplest decreasing function of x satisfying the (7.32)(7.33)(7.34). Free boundary conditions have been employed where the f_i's are set to be zero outside the system.

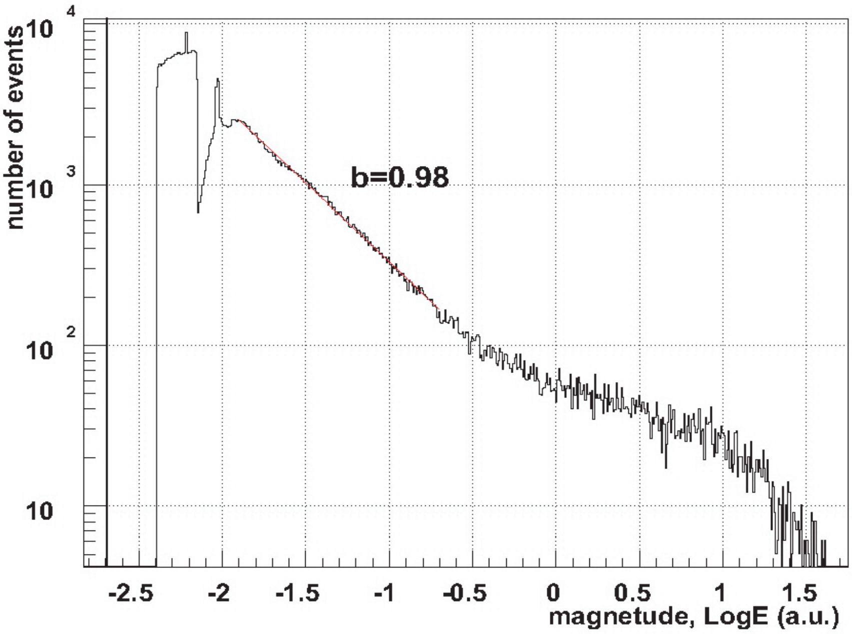

Figure 7.6: The histogram of the magnitude for the one dimensional cellular automaton. The simulation as been performed for a system of 1000 blocks and $v_p = k_p = f_{th} = 1$, $\delta f = 0.01$, Δ =0.8 and α=3.

7.4.1 Summary of the model predictions

This model has all properties already mention for the spring block system: the stick-slip dynamic, the positive dynamic and the Kaiser effect. Moreover it predicts a great variety of event sizes which are in certain range power law correlated, as it is shown in Fig. 7.6. The exponent of the power law varies around one depending on the parameters. While Δ is approaching one and the elements of the system are getting stronger correlated, a clear pick in the large events is appearing in the probability density function of the magnitude. It is quite intuitive that higher is the correlation between nearest neighbors, higher it is the probability to observe events which involve the whole system. However this is not a general conclusion as it will be clarified in the next example of self-organized critical system.

7.5 The two dimensional cellular automaton equivalence

The inhomogeneity of the forces acting in the magnet coil cross section due to the specific field map and to the differences in initial conditions can generate motion of a sub-part of the coil cross section. To take this degree of freedom into account the dimensionality of the system must be increased. In the following the extension of the previous model to two dimensions is discussed neglecting the details of the geometry and difference in the forces acting on the components. The total force exerted on a given block (i,j) is expressed by

$$f_{i,j} = -k_p(x_{i,j} - v_p t) + k_{c1}(x_{i+1,j} + x_{i-1,j} + 2x_{i,j}) + k_{c2}(x_{i,j+1} + x_{i,j-1} + 2x_{i,j}), \tag{7.39}$$

where k_{c1} k_{c2} are the elasticity constat which describe the linear interaction with the neighboring components and k_p is the elasticity of the block subject to compression. As in the previous model the system undergos a uniform compression until a block exceed the solid friction threshold f_{th}. At that moment the unstable block slips and releases the accumulated strength to the neighboring site and gets more compressed. The redistribution of strain after a local slip is given by the relation:

$$f_{i\pm1,j} \rightarrow f_{i\pm1,j} + \delta f_{i\pm1,j}, \tag{7.40}$$

$$f_{i,j\pm1} \rightarrow f_{i,j\pm1} + \delta f_{i,j\pm1}, \tag{7.41}$$

$$f_{i,j} \rightarrow 0, \tag{7.42}$$

and the neighboring forces increases like:

$$\delta f_{i\pm1,j} = \frac{k_{c1}}{2k_{c1} + 2k_{c2} + k_p} f_{i,j}, \tag{7.43}$$

$$\delta f_{i\pm1,j} = \frac{k_{c2}}{2k_{c1} + 2k_{c2} + k_p} f_{i,j}. \tag{7.44}$$

This model has a critical state more robust than the one-dimensional introduced previously and there is no need to introduce the amplification mechanism which imitated the velocity dependent friction law. The estimation of the energy released during the events can be simply estimated as the total number of sites which become unstable. Free boundary conditions are used

7.5.1 Model predictions and remarks

This last model, as the previous one, is suitable to reproduce the stick-slip dynamic, the positive dynamic and the Kaiser effect. Moreover this model predicts a very stable critical state and the power law exponent vary as a function of the conservation of the system as shown in Fig. 7.7. Higher is the level of conservation of the system, higher is the probability to observe a large event. The large event cutoff observed in the magnitude distribution scales with a power function of the dimension of the system.

7.6 Final remarks

The models discussed belongs to the family of the so called Self-Organized Critical Systems [38, 37]. The dynamics of these systems is simple, but already too much complex to hope to solve it analytically. One of the simplest and also the first appeared in the literature which triggered the still open debate about self-organized critical system is the sand pile model. In their original paper [35, 36], Bak, Tang and Wiesenfeld proposed a simple cellular automaton model of sandpile growth. The model is defined on a lattice, which can be taken for simplicity to be the two dimensional square lattice. There is a positive integer variable at each site of the lattice, called the height of the sandpile at that site. The system evolves in discrete time. The rules of evolution are quite simple: At each time step a site is picked

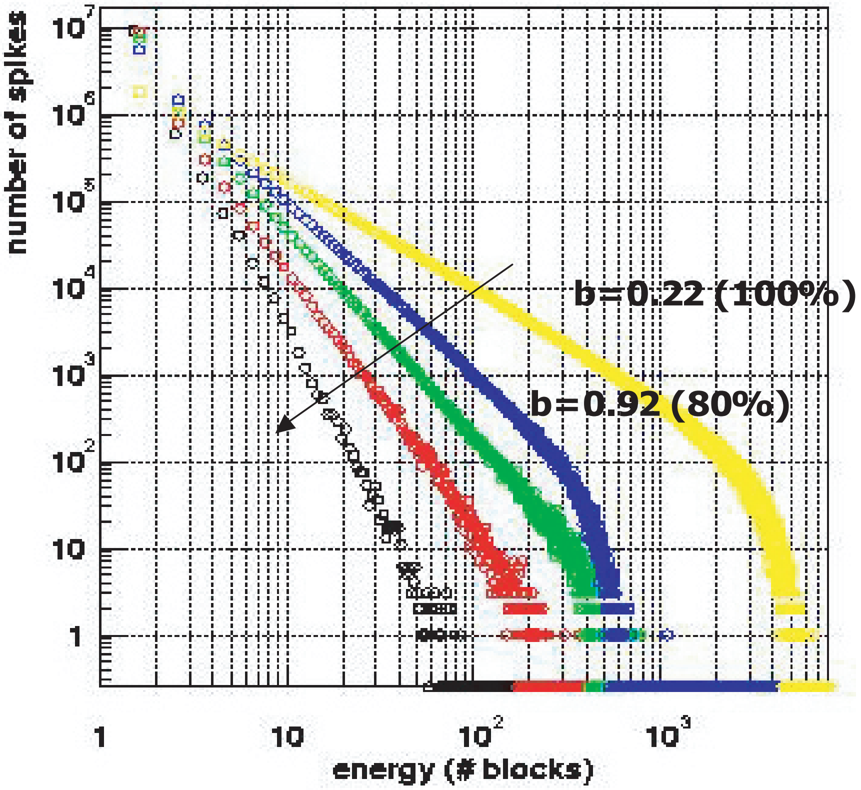

Figure 7.7: The histogram of the magnitude of the events for the two dimensional cellular automaton. Different simulations correspond to different conservative levels. For a conservative system the exponents is about 0.22 and it increases while the systems is getting less conservative.

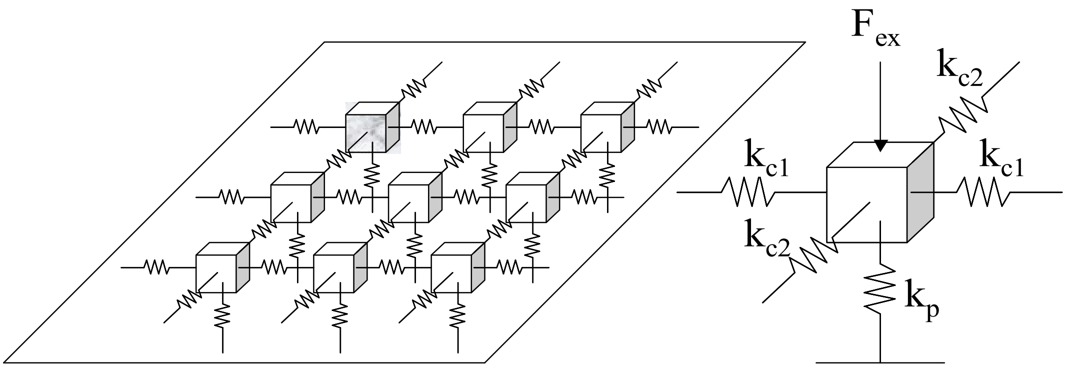

Figure 7.8: The two-dimensional coil model. In this analysis the system is considered homogeneous, composed of equal masses m, each connected to its nearest neighbors by springs of strength k_{c1} and k_{c2}, and to a stationary surface with springs of strength k_p. Each mass is subject to an external applied force which compress the system towards the retaining surface. The blocks (xz) experience a friction force in between their interfaces $f(\dot{x})$, which depends only on the velocity of the block. The equilibrium spacing is a which does not enter directly into the equation of motion

randomly, and its height z_i is increased by unity. If its height is then larger than a critical height z_c, this site is said to be unstable. It relaxes by toppling whereby four sand grains leave the site, and each of the four neighboring sites gets one grain. If there is any unstable site remaining, it too is toppled. In case of toppling at a site at the boundary of the lattice, grains falling *outside* the lattice are removed from the system. This process continues until all sites are stable. Then another site is picked randomly, its height increased, and so on. To make the rules unambiguous, the toppling of sites which were rendered unstable during the same time step is defined to be carried out in parallel. It is easy to show that this process must converge to a stable configuration in a finite number of time steps on any finite lattice using the diffusive nature of each relaxation step. Even this very simple model is still to complex to be solved analytically.

Conclusions and Outlook

General Conclusions

The main issue of this thesis has been the impact of the mechanical perturbations on the quench performance of the LHC magnets

A new instrumentation has been developed (LQA) for 15 m long superconducting LHC dipole cryo-magnet in order to obtain accurate and representative experimental data. It gives for the first time the information needed to identify the block of cables undergoing an irreversible resistive transition and to localize it with centimeter precision in the longitudinal position of the magnet. Already the first test campaign pointed out the systematic weak regions of the magnet extremities, thus giving a feedback for corrective actions in the magnet production and also strong arguments to reject problematic magnets.

A new release of the SPQR program has been developed which takes into account the current distribution between both high and the low magnetic field regions of a cable induced by the magnetoresistance. This program helps to interpret the data provided by the LQA. A graphical interface has been also provided which helps different users to perform numerical simulations.

The improved understanding of the electrical and thermal properties leads to correct simplified equations and provides analytical tools both for an interpretation of the experimental data in existing cables and magnets and for future developments in the field of applied superconductivity.

An intense experimental investigation with the QA and the LQA has been carried out to clarify the phenomenology of spike-signals, the precursors of the irreversible resistive transition in the LHC dipole magnet. The general behavior has been classified. The data reduction strategy adopted here gives indication about the accuracy of the magnet coil manufacture and helps identifying the low quality ones. The stability of the energy distribution indicates a good reproducibility of the final magnet coil winding and collaring procedure inside each manufacturer and among them. There is no clear correlation between global magnet mechanical activity and quench performance which, at least during the experience with the series LHC superconducting dipole magnets, is mainly related to local defects while the rest of the magnet behaves normally.

Several models were introduced to interpret the main properties of the stick-slip events. The cellular automaton approach has been used to simulate the statistical behavior of the events, while the magnet coil turns out to be well described by a two-dimensional array of coupled spring-block system in presence of solid friction. Finally, resemblances with systems introduce in other branches of physics were briefly discussed. A new example of natural system which exhibits long range correlations has been pointed out and can be introduced in the open debate of Self Organized Critical Systems.

Outlook

The LQA is the currently used tool for the investigation of low performance LHC superconducting dipole magnets for the decision of their rejection.

The SPQR program is used for the design optimization of the new generation Nb_3Sn superconducting Rutherford cables with copper added as a separate component for future high energy physic application. The first test campaign will be carried out in Spring 2005 to validate the model.

SPQR is one of the candidate computer applications to start the systematic study of quench margins in the LHC accelerator with respect to beam loss. The study will provide the quench levels as a function of the number of protons lost during the operation, thus setting the threshold dose of the beam loss protection system.

The understanding of the role of the mechanical perturbations gained during this work and the ideas developed for their modelling can already be integrated in the design phase of future accelerator magnets. It is believed, however, that the progress in data collection, expected in due course of the testing of the remaining LHC magnets should result in more quantitative predictions, linked to the measured, physical parameters of the real magnets.

Acknowledgment

I would like to acknowledge Prof.R.Flukiger for his constant support during this project and his belief in me and in the project I wanted to carry out.

I would like to thank A.Siemko, my supervisor, for his help, his great knowledge of magnet technology and for providing me the adequate resources to carry out my research. I would like also to thank him for his extra time he gave me for the reduction of this thesis.

I would like to acknowledge my colleges P.Pugnat, L.Bottura, M.Coccoli, E.Floch, A.Masi, K.Naoui, Prof.L.Rossi, S.Sanfilippo and F.Sonnemann for the endless and useful discussion about applied superconductivity.

Special thanks also to R.Schmidt, B.Denning, V.Kain and G.Guaglio for the interesting discussion about machine protection and beam loss related issues.

I would like to thank the students I had the pleasure to co-supervise, J.M.Pellegrin, L.Thevenod, S.Kouzue and A.Forester.

I am grateful to F.Thierry and M.Genet for their precious help during the design phase of the LQA and the MTM-TF team for their assistance during the experiments.

Bibliography

[1] LHC Design Report Vol. 1, "The LHC Main Ring", *CERN-2004-003*, June 2004.

[2] The LHC study group, "The Large Hadron Collider - Conceptual Design". *CERN/AC/95-05* (LHC), October 1995.

[3] O. Brüning, "Optics Solutions in IR1 and IR5 for Ring-1 and Ring2 of the LHC Version 6.0", *LHC Project Note* 187, April 1999.

[4] H. K. Onnes, Akad. van Wetenschappen (Amsterdam) 14, 113, 818 (1911).

[5] W. Meissner and R. Ochsenfeld, *Naturwiss.* 21, 787 (1933).

[6] F. London and H. London, *Z. Phys.* 96, 359 (1935).

[7] J. Bardeen, L. N. Cooper and J. R. Schrieffer, *Phys. Rev.* 108, 1175 (1957).

[8] O. Dunkel, P. Legrand and P. Sievers, "A Warm Bore Anticryostat for Series Magnetic Measurements of LHC Ssuperconducting Dipole and Short Straight Section Magnets" , presented at *CEC/ICMC* 2003 22-26 September 2003, Anchorage, Alaska.

[9] J. Billan and , al. "Twin Rotating Coils for cold magnetic measurements of 15 m long LHC dipoles", *IEEE trans Appl Sup*, Vol.10, No 1, pp.1422-1426, March 2000.

[10] D. Leroy, J. Krzywinski, V. Remondino, L. Walckiers, R. Wolf, "Quench Observation in the LHC Superconducting One Meter Long Models by Field Perturbation Measurements", Proceeding of the Applied Superconducting Conference, Chicago, 23-28 August 1992.

[11] T. Ogitsu, A. Devred, K. Kim, J. Krzywinski, P. Radusewicz and P. Schermer, "Quench Antenna for Particle accelerator Magnets", SSCL-Preprint-518 Rev.A, May, 1994.

[12] A. Siemko, J. Billan, G. Gerin, D. Leroy, L. Walckiers and R. Wolf, "Quench Localization in the superconducting model magnets for the LHC by means of pick-up coils", *IEEE Trans. Appl. Sup.*,Vol.5, pp.1028-1031, June 1995.

[13] S. Jongeleen, D. Leroy, A. Siemko and R. Wolf, "Quench Localization and Current Redistribution after Quench in Superconducting Dipole Magnets wound with Ruttherford-Type Cables". *LHC Project Report* 59, CERN, Geneva, 1996.

[14] B. Dezillie, K. Artoos, A. Siemko, R. Mompo, D. Tommasini, "Study Of Mechanical Disturbances in Superconducting Magnets Using Piezoelectric Sensors and Quench Antenna", *LHC Project Report* 498, CERN, Geneva, 2001.

[15] privite comunication, K. Naoui.

[16] A. F. Greene, "Recent status of superconductors for accelerator magnets." *Proceedings of the Workshop on AC-Superconductivity*, KEK, Japan, 1992.

[17] K. H. Mess, P. Schmüser, S. Wolff, "Superconducting Accelerator Magnets". *Wold Scientific Publications*, 1996.

[18] M. N. Wilson. "Superconducting magnets". *Oxford Science Publications*, 1983.

[19] R. Perin. "Field, Forces and Mechanics of Superconducting Magnets". *CERN CAS School on Superconductivity*, 1995.

[20] P. Pugnat, B. Khomenko, A. Rijlart, S. Sanfilippo and A. Siemko, "Statistical diagnosis method of conductor motions in superconducting magnets to predict their quench performance", *LHC Project Report* 455, CERN, Gevena, 2000.

[21] M. Calvi, N. Ponomarev, P. Pugnat and A. Siemko, "Statistical analysis of conductor motion in LHC superconducting dipole magnets", *IEEE Trans. Appl. Sup.* Vol.14, N.2, June 2003.

[22] M. Calvi, E. Floch, S. Koukue and A. Siemko, "Precise Quench Localization and Quench Propagation Velocity Measurements in the LHC Superconducting Dipole Magnets", presented to the ASC2004, Jacksonville, 2004.

[23] M. Calvi, A. Forrester and A. Siemko "Modelling Quench signals in The LHC superconducting Dipoles". To be submitted to *IEEE Trans. Appl. Sup.*, Geneva (CERN), 2004.

[24] M. Calvi "Quench Propagation in the LHC Superconducting Busbars". Diploma Thesis, Polytechnic of Turin, Italy, 2000.

[25] F. Sonnemann, M. Calvi, "Quench Simulation Studies: Program documentation of SPQR", LHC project note 265, 2001.

[26] R. Herzog, M. Calvi, F. Sonnemann "Quench Propagation 600A busbars", Advances in Cryogenic Engineering, Procedings of the Engeneering Cryogenic Conference - CEC, Madison, Wisconsin (USA), July 2001.

[27] R. Herzog, M. Calvi, F. Sonnemann and J. M. Pelegrin "Quench Propagation and Heating in the flexible 6 kA busbars", Advances in Cryogenic Engineering, Procedings of the Engeneering Cryogenic Conference - CEC, Madison, Wisconsin (USA), July 2001.

[28] F.Sonnemann, "Resistive Transition and Protection of the LHC Superconduting Cables and Magnets", CERN-THESIS-2001-004.

[29] L. Rossi, "Superconducting Magnets for the LHC main Lattice", *LHC Project Report 718*. Presented at the 18^{th} International Conference on Magnet Technology (MT-18) 20-24, October 2003, Morioka, Japan.

[30] L. Rossi, "State of the Art Superconducting Acellerator Magnets", *LHC Project Report 541*. Invited paper at the 17^{th} International Conference on Magnet Technology (MT17) 24-28 September 2001, Geneva, Switzerland.

[31] L. Rossi, "Superconducting Cable and Magnets for the Large Hadron Collider", *LHC Project Report 694*, Presented at the 6th European Conference on Applied Superconductivity (EUCAS 2003) 14-18 September 2003, Sorrento Napoli - Italy.

[32] A. Devred, T. Ogitsu, K. Tsuchiya, ŞInvestigation of wire motion in superconducting magnetsŤ, *IEEE Trans. Magn.*, vol. 27, pp. 2132-2135, 1991.

[33] B. Gutenberg and C. F. Richter, "Earthquake magnitude, intensity, energy and acceleration", *Bull. Seism. Soc. Am.*, Vol. 46, pp. 105-143, 1956.

[34] Franz-Josef Elmer, "Non linear dynamics of dry friction", *J.Phys.A*, Math. Gen. 30, 1997.

[35] P. Bak, C. Tang and K. Wiesenfield, "Self-organised Criticality" *Phys. Rev. Lett.* Vol.59, pp.381, 1987.

[36] P. Bak, C. Tang and K. Wiesenfield, "Self-organised Criticality", *Phys.Rev.A*, Vol.38, No 1, pp. 364-374, 1988.

[37] P.Bak, "How nature works : the science of self-organized criticality" Oxford Univ. Press, Oxford, 1997.

[38] Jeldtoft Jensen, "Self-organized criticality: emergent complex behaviour in physical and biological systems" Cambridge Univ. Press, Cambridge, 1998.

[39] S.Lise and H.J.Jensen, "Transition in Nonconserving Models of Self-Organized Criticality", *Phys. Rev. Lett.* Vol.76, N.13, 1996.

[40] R. Burridge and L. Knopoff. *Bull. Seismol. Soc. Am.* 57, 341 (1967).

[41] A. Gabrielov, "Abelian avalanges and Tutte polynomials", *Physica A*, 195, pp.253-274, (1993).

[42] D. Dhar and R. Ramaswamy, "Exactly Solved Model of Self-Organized Critical Phenomena", *Phys. Rev. Lett.*, Vol.63, N.16 (1989).

[43] D. Dhar, "Self-Organized Critical State of Sandpile Automaton Models", *Phys. Rev. Lett.*, Vol.64, N.14 (1990).

[44] D. Dhar, S. S. Manna, "Inverce avalanges in the Abelian sanpile model", *Phys. Rev. E*, Vol.49, N.4 (1994).

[45] M. Carlson and J. S. Langer, "Properties of Earthquakes Generated by Fault Dynamics", *Phys. Rev. Lett.* 62, 2632 (1989).

[46] J. M. Carlson and J. S. Langer, "Mechanical model of an earthquake fault", *Physical Review A*, 21 July 1989.

[47] Hiizu Nakanishi, "Cellular-automaton model of earthquakes with deterministic dynamics", *Physical Review A*, Vol.41, N.12, 15 June 1990.

[48] Hiizu Nakanishi, "Statistical properties of cellura-automaton model for earthquakes", *Physical Review A*, Vol.43, N.12, 15 June 1991.

[49] Z. Olami, H. J. Feder and K. Christensen, "Self-Organized Criticality in Cotinuos, Nonconservative Cellular Automaton Modelling Earthquakes", *Physical Review Letters*, Vol.68, N.8, 24 February 1992.

[50] K. Leung, J. Muller and J. V. Andersen, "The Two-dimensional Nonlinear Birrigen-Knopoff Model of Earthquakes", arXiv:cond-mat/9510020 v2, 5 October 1995.

[51] D. Sornette, "Critical phenomena in natural science", Springer Series in Synergetics, SPRINGER, Heidelberg, 2000.

[52] L. Bottura, M. Breschi, C. Rosso, "Analysis of Electrical Coupling Parameters in Superconducting Cables", *Cryogenics* Vol.43, May, 2003.

[53] L. Bottura, M. Breschi, M. G. Fabbri, "Analytical solution for Current Distribution in Multistrends Superconducting Cables", *J.Appl.Phys.*, Vol.92, pp.7571.7580.

[54] L. Dresner, "Propagation of normal zones in thermal insulated superconductors". *Advance in Cryogenics Engeneering*, N.26, pp.647-653, 1980.

[55] A. Devred, "Investigation of the normal zone along a superstabilizedsuperconductor solenoid", *J.Appl.Physic.* Vol.66(6) 15 September 1989.

[56] A. Devred, "General Formulas for the adiabatic velocity of the normal zone", *IEEE Transaction on Magnetics*, Vol.25, N.2, March 1989.

[57] A. Devred, "Investigation of current redistribution in superconducting winding when switching to the normal resistive state", *J. Appl. Phys.* Vol.65, N.10, 15 May 1989.

[58] A. Devred, C. Meuris, "Analitical Solution for the propagation velocity of normal zones in large matrix-stabilized superconductor".

[59] L. Dresner , "Stability of supercondutors", ISBN: 0-306-45030-5, *Lenum Press*, 1995.

[60] P. Bauer, "Stability of superconducting strands for accelerator magnets", PhD Thesis, Technische Universität Wien, 1998.

[61] Z. Stekly et al. Stability of superconductors. IEEE Trans. 12, 1965.

[62] B.J. Maddock et al. Stability of superconductors. Cryogenics 9, 1969.

[63] F.R.Fickett, "Magnetoresistivity of Copper and Allunimum at cryogenic temperatures". Preceeding of the 4^{th} International Conference of Magnet Technology, pp.539-541, Upton USA, 1972.

[64] R.W.Arenz, C.F.Clark, W.N.Lawless, "Thermal conductivity and electrical resistivity of copper in intense magnetic field at low temperature", *Phys.Rev.B*, Vol26, N.6, pp.2727-2732, September 1982.

[65] Privite comunication Eric Floch.

[66] Privite comunication Andrzej Siemko.

[67] R. Brun, F. Rademakers, "ROOT - An Object Oriented Data Analysis Framework", Proceeding AIHENP96 Workshop Lausanne, 1996, *Nucl. Inst. and Meth. in Phys. Rev. A* 389, 1997, pp. 81-86.

[68] F. Sonnemann and R. Schmidt. "Quench simulations of LHC accelerator magnets and busbars", *Cryogenics* 40, CHATS 2000 Proceedings, 2000.

[69] F. Sonnemann et al., "The protection system for the superconducting elements of the LHC at CERN", *Proceedings* of PAC 99, New York, USA, 1999.

[70] R. Schmidt et al., "Machine Protection System for the LHC: Architecture of the Beam and Powering Interlock Systems." *CERN LHC Project Report* 521, December 2001.

[71] A. Ballarino, "Application of high temperature superconductors to accelerators", *Proceedings* of EPAC 2000, Vienna, Austria, 2000.

[72] Ph. Lebrun, "Superfluid helium as a technical coolant", *Proceedings* of the 15^{th} UIT, 1997.

[73] M.Coccoli, R.Scanlan, M.Calvi et al. "Fabrication and performance of Nb_3Sn Rutherford-type cable with Cu added as a separate component" Presented at the 18th International Conference on Magnet Technology (MT-18) 20-24 October 2003, Morioka, Japan.

[74] R. Schmidt, M.Calvi, V.Kain, A.Siemko, "Operating the lhc initially at a lower energy?", presented at the LHC Project Workshop - Chamonix XIII, 2003.

Appendix A

Transfer function of pick-up coils

It is assumed that the coils in the LQA are essentially two-dimensional, i.e., that they are $l \times w$ rectangular loops with no thickness, where $l = 4$ cm and $w = 1$ cm. The coils of wire are looped N_t times, where $N_t = 400$. It is also assumed that their 1-cm widths are small enough that the magnetic field can be taken as constant along that dimension. The values for the magnetic field vector throughout a given coil are thus taken along a line down the center of the coil.

Mathematically, the quench signal $V(t)$ for a single coil due to the changing current distribution in wire 1 alone is expressed below:

$$V(t) = -\dot{\Phi}_B(t), \tag{A.1}$$

the negative time derivative of the magnetic flux Φ_B in the coil

$$= -\partial_t \left[N_t \int_S \mathbf{B}(z', t) \cdot d\mathbf{A} \right], \tag{A.2}$$

where the magnetic field B is a function of z' taken along the center of the coil and is integrated over the surface S of the coil, with $d\mathbf{A}$ pointing in the assigned normal direction $\hat{\mathbf{n}}$ of the coil

$$= -\partial_t \left[N_t \int_{-l/2}^{l/2} \mathbf{B}(z', t) \cdot \hat{\mathbf{n}}\, w\, dz' \right], \tag{A.3}$$

because the surface integral simplifies to a line integral

$$= -\partial_t \left[N_t \int_{-l/2}^{l/2} \left(\int_{-\infty}^{\infty} \frac{\mu_0}{4\pi} \frac{I_1(z - v_q t)\, d\mathbf{z} \times \mathbf{r}}{r^3} \right) \cdot \hat{\mathbf{n}}\, w\, dz' \right], \tag{A.4}$$

where the magnetic field B is calculated using Biot-Savart's Law, with z taken as a position along wire 1 and with $\mathbf{r}$, a function of z and z', taken as the vector extending from the position along the wire at z to the position along the center of the coil at z'

$$= -\frac{\mu_0}{4\pi} \partial_t \left[N_t\, w\, (\hat{\mathbf{z}} \times \mathbf{r}) \cdot \hat{\mathbf{n}} \int_{-l/2}^{l/2} \left(\int_{-\infty}^{\infty} I_1(z - v_q t) \frac{1}{r^3} dz \right) dz' \right], \tag{A.5}$$

after pulling out the constants from the integrals (and since $\mathbf{r}$ *per se* should not be taken out of the integral, let $\mathbf{r} = \mathbf{d}$, where $\mathbf{d}$ is the distance vector, perpendicular to the coil's axis and wire 1, that gives the distance d between them)

$$= -\frac{\mu_0}{4\pi}\partial_t\left[N_t\, w\,(\hat{\mathbf{z}}\times\mathbf{d})\cdot\hat{\mathbf{n}}\int_{-\infty}^{\infty}\left(\int_{-l/2}^{l/2} I_1(z-v_q t)\frac{1}{r^3}dz'\right)dz\right], \tag{A.6}$$

after switching the order of integration

$$= -\frac{\mu_0}{4\pi}\partial_t\left[N_t\, w\,(\hat{\mathbf{z}}\times\mathbf{d})\cdot\hat{\mathbf{n}}\int_{-\infty}^{\infty} I_1(z-v_q t)\left(\int_{-l/2}^{l/2}\frac{1}{r^3}dz'\right)dz\right], \tag{A.7}$$

after pulling out I_1, which is constant with respect to z'

$$= -\frac{\mu_0}{4\pi}\partial_t\left[\int_{-\infty}^{\infty} I_1(z-v_q t)\left(\int_{-l/2}^{l/2}\frac{N_t\, w\,(\hat{\mathbf{z}}\times\mathbf{d})\cdot\hat{\mathbf{n}}}{r^3}dz'\right)dz\right], \tag{A.8}$$

where all the geometry-dependent[1] constants are grouped with the geometry-dependent integral

$$= -\frac{\mu_0}{4\pi}\partial_t\left[\int_{-\infty}^{\infty} I_1(z-v_q t)\, h(z)\, dz\right], \tag{A.9}$$

calling the geometry-dependent integral h and the "geometric coupling function," or just the "coupling function"

$$= -\frac{\mu_0}{4\pi}\partial_t(I_1 * h)\,(-v_q t), \tag{A.10}$$

the convolution of I_1 and h, by definition

$$= -\frac{\mu_0}{4\pi}\left(\dot{I}_1 * h\right)(-v_q t), \tag{A.11}$$

since only I_1 is a function of time

$$= -\frac{\mu_0}{4\pi}\left(\dot{i} * h\right)(-v_q t), \tag{A.12}$$

then

$$= \frac{\mu_0}{4\pi}v_q\,(i' * h)\,(-v_q t). \tag{A.13}$$

So the quench signal is simply a convolution of the derivative of the current redistribution in the quenching cable with the pertinent geometric coupling function. The geometric coupling function h is explicitly calculated below (letting $N_t\, w\,(\hat{\mathbf{z}}\times\mathbf{d})\cdot\hat{\mathbf{n}} = g$):

$$h(z) = \int_{-l/2}^{l/2}\frac{g}{r^3}dz' \tag{A.14}$$

$$= \int_{-l/2}^{l/2}\frac{g\, dz'}{\left(d^2 + (z-z')\right)^{3/2}} \tag{A.15}$$

---

[1] "Geometry-dependent" means dependent upon the postion (of the wires) of the cable of interest with respect to the coil(s) of interest.

$$= g\left(\frac{l/2 - z}{d^2\sqrt{(l/2 - z)^2 + d^2}} + \frac{l/2 + z}{d^2\sqrt{(l/2 + z)^2 + d^2}}\right). \tag{A.16}$$

Since pairs of coils are connected together in series, the resulting signal is a sum of the signals from each coil due to each wire. For example, coils A and C are in series, so the resulting signal V_{AC} is

$$V_{AC}(t) = V_{A1}(t) + V_{A2}(t) + V_{C1}(t) + V_{C2}(t) \tag{A.17}$$

$$= \frac{\mu_0}{4\pi} v_q\left[(i' * h_{A1})(-v_q t) + (i' * h_{A2})(-v_q t) + (i' * h_{C1})(-v_q t) + (i' * h_{C2})(-v_q t)\right] \tag{A.18}$$

$$= \frac{\mu_0}{4\pi} v_q\left(i' * [h_{A1} + h_{A2} + h_{C1} + h_{C2}]\right)(-v_q t) \tag{A.19}$$

$$= \frac{\mu_0}{4\pi} v_q\left(i' * H_{AC}\right)(-v_q t), \tag{A.20}$$

where H_{AC} is the total geometric coupling function for coils A and C with respect to a particular cable. The quench signal V_{BD} and its coupling function H_{BD} come about in the same manner.

Appendix B

Numerical study

Eq.4.6 is a non linear parabolical equation of this form:

$$C(T)\cdot\frac{dT}{dt}=\frac{d}{dx}\left(k(T)\frac{dT}{dx}\right)+f\left(T,\frac{dT}{dt}\right)\tag{B.1}$$

with boudery conditions:

$$T(x,0)=T^0(x),\quad \left.\frac{dT}{dt}\right|_{(x,0)}=0,\quad 0\le x\le L;\tag{B.2}$$

$$\left.\frac{dT}{dx}\right|_{(0,t)}=0,\quad \left.\frac{dT}{dx}\right|_{(L,t)}=0,\quad L>0.\tag{B.3}$$

Approximation of the order of $O(\tau+h^2)$ for the above problem can be obtained with the use of the following sheme:

$$C(T_i^n)\frac{T_i^{n+1}-T_i^n}{\tau}=\frac{1}{h}\left[s(T_{i+1}^n)\frac{T_{i+1}^{n+1}-T_i^{n+1}}{h}-s(T_i^n)\frac{T_i^{n+1}-T_{i-1}^{n+1}}{h}\right]+f\left(T_i^n,\frac{T_i^n-T_i^{n-1}}{\tau}\right)\tag{B.4}$$

where the function $s(T_i)$ can take one of the following forms:

$$s(v_i)=\frac{1}{2}\left[k(v_{i-1})+k(v_i)\right],\tag{B.5}$$

$$s(v_i)=k\left(\frac{v_{i-1}+v_i}{2}\right),\tag{B.6}$$

$$s(v_i)=\frac{2k(v_{i-1})k(v_i)}{k(v_{i-1})+k(v_i)};\tag{B.7}$$

for $v_i{=}T_i^n$ or $v_i{=}T_i^{n+1}$. This sheme is unconditionally stable. It is a system of linear equation with tridiagonal matrix.

$$\begin{bmatrix} b_1 & c_1 & 0 & ... & 0 & 0 & 0\\ a_2 & b_2 & c_2 & ... & 0 & 0 & 0\\ ... & ... & ... & ... & ... & ... & ...\\ 0 & 0 & 0 & ... & a_{N-1} & b_{N-1} & c_{N-1}\\ 0 & 0 & 0 & ... & 0 & a_N & b_N \end{bmatrix}\cdot\begin{bmatrix} u_1\\ u_2\\ ...\\ u_{N-1}\\ u_N\end{bmatrix}=\begin{bmatrix} r_1\\ r_2\\ ...\\ r_{N-1}\\ r_N\end{bmatrix}\tag{B.8}$$

The coefficient of the known vector for i=1 to i=N are:

$$r_i = T_i^n + f\left(T_i^n, \frac{T_i^n - T_i^{n-1}}{\tau}\right)\frac{\tau}{C(T_i^n)}. \tag{B.9}$$

The coefficients of the matrix for i=2 to i=N-1 are:

$$a_i = -s(T_i^n)\frac{\tau}{C(T_i^n)h^2}, \tag{B.10}$$

$$b_i = 1 + \left(s(T_{i+1}^n) + s(T_i^n)\right)\frac{\tau}{C(T_i^n)h^2}, \tag{B.11}$$

$$c_i = -s(T_{i+1}^n)\frac{\tau}{C(T_i^n)h^2}. \tag{B.12}$$

Using the boundary conditions (B.3) the value for i=1 and i=N of the matrix are:

$$b_1 = 1 + 2s(T_2^n)\frac{\tau}{C(T_1^n)h^2}, \tag{B.13}$$

$$c_1 = -2s(T_2^n)\frac{\tau}{C(T_1^n)h^2}, \tag{B.14}$$

$$a_N = -2s(T_N^n)\frac{\tau}{C(T_N^n)h^2}, \tag{B.15}$$

$$b_N = 1 + 2s(T_N^n)\frac{\tau}{C(T_N^n)h^2}. \tag{B.16}$$

List of Tables

List of Figures